LOUGHBOROUGH UNIVERSITY

# Modelling of dynamical effects related to the wettability and capillarity of simple and complex liquids

by

Desislava V. Todorova

A thesis submitted in partial fulfillment for the degree of Doctor of Philosophy

in the

Faculty of Science

Department of Mathematical Sciences

29 November 2013

# *Acknowledgements*

I would like to express my deep gratitude to Prof. Uwe Thiele for being an exceptional supervisor. By exceptional, besides many other great things, I mean approachable, patient, encouraging, forgiving and always passionate and contagiously excited about our projects.

My thanks goes to all members of our research group at the Department of Mathematics and my office mates for their friendship, help and support. A special "thank you" goes to Mariano Galvagno, for being not only a great friend, but also an invaluable help in the cases when I needed technical support and a discussion compañero. To Hender López and Nikita Tretyakov, whom I was very fortunate to collaborate with.

To my parents, Galina and Valentin, for the love, constant support and encouragement in everything I do. To my caring sister Kristina, for being also my best friend.

To my love, Nikola, for his rational approach to life that perfectly balances mine. For always being beside me and for keeping me sane.

# *Abstract*

This Thesis explores physical phenomena characteristic for thin liquid films and small droplets of simple and complex liquids on solid substrates for which wettability and capillarity control their statical and dynamical properties.

We start by discussing the general concepts of wettability and capillarity and introduce the common mathematical framework of the lubrication approximation for studies of thin liquid films and small contact angle drops. We demonstrate the derivation of the generic equation describing the evolution of a film of simple liquid from the Navier–Stokes equations. We show how this model can be further extended to incorporate various effects relevant to the case of complex liquids.

The results described in the Thesis comprise three projects with the common main theme of the influence of wettability and capillarity on the statics and dynamics of the studied systems, namely

(i) Evaporating sessile droplets fed through the solid substrate - a geometry that allows us to discuss steady states of the system and their role in the time evolution of freely evaporating droplets without influx in an isothermal case;

(ii) The influence of a solute–dependent wettability on the stability, static and dynamical properties of thin films and drops of non-volatile mixtures, suspensions and solutions;

(iii) A parameter-passing scheme between particle–based Molecular Dynamics simulations and the continuum lubrication model which allows us to discuss equilibrium properties of small polymeric droplets.

We present the physical questions arising in the three systems and discuss approaches and results as well as possible extensions.

Chapters 3 and 5 of this thesis are based on the publications:

**Steady evaporating droplets fed by an influx – the isothermal limit.**
*Desislava Todorova, Uwe Thiele and Len M. Pismen*
J. Engg. Math. 73, 17-30 (2012). DOI: 10.1007/s10665-011-9485-1;

**Parameter passing between Molecular Dynamics and continuum models for droplets on solid substrates: The static case.**
*Nikita Tretyakov, Marcus Müller, Desislava Todorova and Uwe Thiele*
J. Chem. Phys. 138, 064905 (2013). DOI: 10.1063/1.4790581;

Parts of the major results and discussion presented in Chapter 4 are included in the publication:

**Gradient dynamics description for films of mixtures and suspensions: Dewetting triggered by coupled film height and concentration fluctuations**
*Uwe Thiele, Desislava Todorova and Hender Lopez*
Phys. Rev. Lett. 111, 117801 (2013). DOI: 10.1103/PhysRevLett.111.117801.

# Contents

# Chapter 1

# Introduction

Thin films are ubiquitous. They are found both in nature and in various technological applications. Being a subject of interest in a wide range of fields, they are practically invaluable. For example, they appear in biophysics as membranes or tear film in the eye [155], acting as a lubricant to protect the cornea. They can be found in geology, when considering lava flows [11, 72]. Moreover, they have countless applications in engineering and technology, e.g. in heat and mass transfer processes to limit fluxes and protect surfaces [12]; in coating technology to modulate the optical response of a surface, typically as an antireflective coating [77, 85, 90, 134, 190]; as memory devices in the case when thin magnetic films are employed for data storage; in immersion lithography in the process of manufacturing micro- and nanodevices [57, 66]; many other processes involving liquids on solid and soft substrates. Thin liquid films are typically composed of common liquids such as water or oil, but also multicomponent mixtures of two or more phases, referred to as *complex liquids*, such as polymer solutions or melts, nanoparticle suspensions, etc. [40, 55, 118, 188, 191].

In fluid mechanics, *capillarity* and *wettability* are collective labels for effects resulting from the intermolecular interactions occurring at the interface formed when two substances come into contact and at the three–phase contact region if three

substances are involved, respectively. They play a crucial role in practically all industrial and engineering processes where liquid-solid interfaces are involved. However, the mechanisms governing the wetting behaviour are still not completely understood. This Thesis is formed of three projects, presented in Chapters 3, 4 and 5, with the main theme of the influence of wettability and capillarity effects on the statics and dynamics of thin films and small droplets. In Chapter 2 we introduce the basic concepts related to the wetting behaviour as well as the general model we use throughout the Thesis.

A liquid layer on a substrate is called a *thin film* if its thickness is much smaller than the typical length scales parallel to the substrate. Therefore, "thin" does not refer to an absolute film thickness and should be defined for each physical problem studied. The dynamical and statical properties of thin films with a liquid–gas interface (also referred to as a "free surface") can be analysed with the full Navier–Stokes [84, 140] or Stokes [22] equations but the most natural theoretical approach to them is based on the so called *lubrication approximation*, also known as long-wave theory [114]. It is based on the procedure of asymptotic reduction of the full set of governing equations and boundary conditions, characterising the system, to a simplified, yet highly nonlinear, evolution equation for the local thickness of the liquid film, which we refer to as the *thin film equation*. Although lacking the full mathematical complexity of the original free-boundary problem, the model preserves many of the important features of its physics. We demonstrate the derivation of the general thin film equation in Chapter 2.

Many practical processes require the spreading of a liquid on a solid surface [21, 97]. When a liquid makes contact with a solid, a three-phase contact line is formed. This contact line may move along the surface of the solid, driven by both the external fluid flow and the thermodynamically-determined contact angle that the liquid-gas interface makes with the solid surface. Evaporation of thin liquid films and sessile droplets has attracted much attention recently as a way to study the dynamics of the contact line [88, 141], as well as a route to create deposition patterns through sedimentation of solutes and suspensions on a solid surface [40, 41, 169]. For small sessile droplets in well controlled experiments

on smooth substrates the main influences are the liquid - substrate interactions (wettability and capillarity). In Chapter 3 we present an isothermal version of the thin film equation describing the influence of capillarity and wettability on evaporation in the case of complete wetting. We discuss the possible role which the steady states of a "fed" system play in the time evolution of freely evaporating droplets.

An increasing number of experiments is now performed not only with simple but also with complex liquids [40, 55, 118, 159, 188, 191]. Popular examples include spreading and dewetting of films and droplets of polymer solutions or nanoparticle suspensions [40, 191], as well as decomposition and dewetting of films of polymer mixtures [55]. Films of complex liquids have various presently employed and many further potential applications, but their properties are still not completely understood. An important aspect of the problems associated with thin films of mixtures, emulsions and suspensions is their stability. In many technological and everyday processes where a uniform film is involved, e.g. wall paint or various coatings, it is important that the film does not rupture and break up. On the contrary, for butterflies and birds, it is important that water does not form a continuous wetting film on their wings and bodies, but instead breaks up into droplets which can easily fall off.

Although in these systems the wettability and capillarity still control their statical and dynamical properties, they may interact with other phenomena such as the diffusive transport of the solute, phase transitions such as phase separation, evaporation of the solvent and others. Therefore, the understanding of the underlying thermodynamic behaviour is crucial for constructing a successful model for the coupling between the processes. For the case of two-component mixtures, nanoparticle suspensions and solutions, at least two dynamic equations are needed - one for height and one for composition. In Chapter 2 we introduce a gradient dynamics formulation for a films of complex liquids and show that it is equivalent to thin film equations in the literature. Later, in Chapter 4 we employ the derived dynamical model to study the linear stability of flat homogeneous films. In particular, we investigate how the stability thresholds are influenced by the

incorporation of an additional degree of freedom related to the concentration field. We also analyse nonlinear thickness and concentration profiles for steady droplets and relate them to the binodal curves obtained for the case of two coupled fields. Finally, we look at the time evolution of flat homogeneous films with solute and further discuss the dynamical effects of the coupled height and composition fluctuations.

The physical phenomena that determine the shape of a sessile drop on a given surface, hence the equilibrium three–phase contact angle, have been a subject of interest for a long time now. Both particle–based and continuum models have been applied in the last decades to study the behaviour of small quantities of liquids on solid [13, 21, 162] and soft [109, 151] substrates both in equilibrium and in the presence of driving [149, 173]. In Chapter 5 we compare the equilibrium properties of small droplets by transferring information from a particle based simulation technique (Molecular Dynamics) towards the continuum description provided by the thin film theory in a region where both descriptions can be presumed valid. We explore how the two models can be "coupled", in particular applied to find out what information one can pass from the particle–based model into the continuum description and how and in what form it needs to be extracted. Then we use both approaches to determine the equilibrium contact angle for droplets of various sizes and strengths of interaction between the liquid and the substrate. Moreover, we describe several ways the contact angle can be defined. By comparing the results of the two descriptions we also explore the limits of applicability of the thin film theory.

Finally, Chapter 6 summarises the results and gives concluding remarks.

# Chapter 2

# Basic concepts and background theory

## 2.1 Wettability: interaction of a liquid film with the substrate.

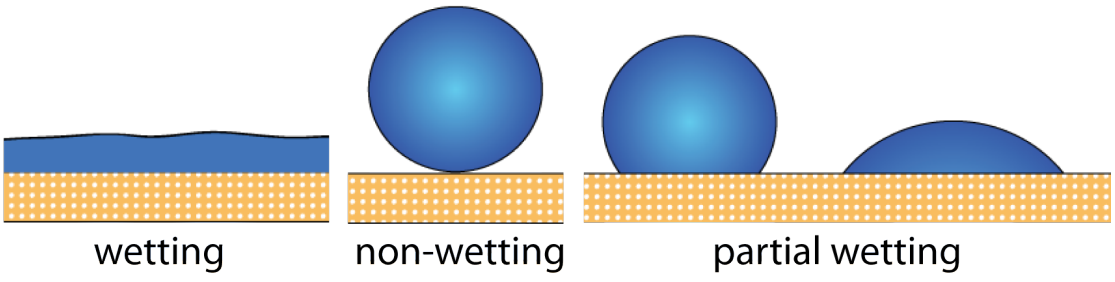


FIGURE 2.1: A sketch of three different types of wetting behaviour of a liquid on a solid substrate: (i) complete wetting (left), (ii) non-wetting (middle) and (iii) two cases of partial wetting (right).

The interactions arising between solid substrates with a smooth rigid surface and free surfaces need to be taken into account when characterising the macroscopic properties of a liquid in contact with a solid. One needs to take into account the local properties of the system (e.g. surface or interfacial tension) along with long-range forces (e.g. van der Waals interactions). Generally speaking, the van der Waals forces act between all molecules, due to dipolar interactions. They are

called after the Dutch physicist *Johannes Diderik van der Waals* (Nobel Laureate in Physics, 1910), because of his contribution in the development of the equation of state for liquids and gases. The van der Waals forces are of a universal importance - they arise between all combinations of surfaces and molecules. The term "van der Waals forces" involves a range of interactions - Coulomb interaction, monopole–dipole and dipole–dipole interactions, Debye interaction, Keesom interaction and London dispersion interactions. They are all important in understanding the structure and phase behaviour of any type of systems where surfaces and interfaces are involved [28, 74, 139]. The interactions in simple and multicomponent systems with surfaces/interfaces are usually related to the interactions between molecules in a particular medium. This is of a major importance for self–assembling systems involving polymers or/and surfactants, as the interactions and the equilibrium structures strongly depend on the choice of solvent.

Generally, when a liquid comes into contact with a flat solid substrate, there are three possible outcomes: (i) complete wetting – the liquid forms a flat film on the substrate, corresponding to a zero equilibrium contact angle $\theta_E$; (ii) non-wetting – the formed droplet does not wet the substrate and forms an ideal sphere that touches the substrate in a single point only, $\theta_E = \pi$ or (iii) partial wetting – the liquid forms a droplet with a finite contact angle $0 < \theta_E < \pi$ on the substrate. The three possible situations are sketched on Fig. 2.1. In situation (iii) the border of the region, where the liquid wets the substrate, is the so called *contact line*. For droplets on a flat homogeneous surface with no lateral driving the contact line is a circle.

One can approximate the contact line region by a macroscopic wedge, as shown in Fig. 2.2, and assign a certain energy per unit area (or length in the 1-dimensional case) to every interface – $\gamma_{SG}$ for the gas–solid interfacial energy, $\gamma$ for the gas–liquid interface and $\gamma_{SL}$ for the liquid–solid interface. For the finite contact angle $\theta_E$ characterising the three-phase region, the Young–Laplace law is satisfied [39]

$$\gamma_{SL} + \gamma \cos\theta_E - \gamma_{SG} = 0. \tag{2.1}$$

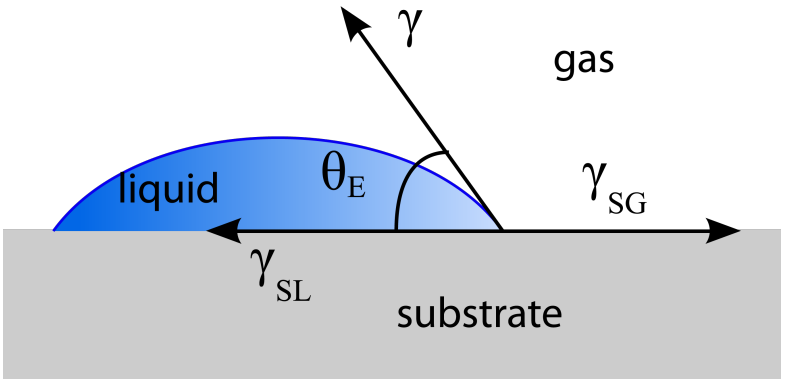


FIGURE 2.2: A sketch of a liquid drop sitting on a solid substrate. The three-phase contact line region is approximated by a wedge and the corresponding solid-gas $\gamma_{SG}$, liquid–gas $\gamma$ and solid–liquid $\gamma_{SL}$ interfacial energies and the equilibrium contact angle $\theta_E$ are indicated.

Equation 2.1 can also be interpreted as a mechanical force balance at the three–phase contact line. It is best derived when considering a reversible change in the position of the contact line, with the help of global energetic arguments [21, 39]. In that way the nature of the contact line region and thus the action of the intermolecular forces is not considered. Accordingly, $\theta_E$ is understood to be measured macroscopically, meaning it is done on a scale above the one of long–range intermolecular forces.

Here, one defines the three interfacial tensions for the case when the three participating media (liquid, solid and gas) are in a mechanical equilibrium with each other. Additionally, one may consider a chemical equilibrium, that is matching between the chemical potentials for each of the components of the system, and a thermal equilibrium, which is a temperature balance between the liquid and the gas phase, guaranteeing the gas is the saturated vapour of the liquid. The mechanical, chemical and thermal equilibrium altogether constitute a thermodynamic equilibrium [21].

If, for a given combination of materials the interfacial tensions are known, then one can directly predict the wetting regime of the fluid. The contact angle is zero when $\gamma_{SG} = \gamma_{SL} + \gamma$. If $\gamma_{SG} < \gamma_{SL} + \gamma$, one observes a droplet with a finite

contact angle, corresponding to the case of partial wetting. Partial wetting corresponds to droplets, coexisting with a microscopically thin film absorbed at the solid substrate, known as a *precursor film*. In a state of thermodynamic equilibrium, molecules adsorbed onto the substrate are always present - the surface surrounding the droplet is never completely dry. The case of complete wetting corresponds to a macroscopically thick layer. For sufficiently thick films the interfacial energies can be calculated using the assumption that the materials are in bulk state. An interesting question is what exactly happens when the film becomes so thin that one can not assign to it bulk properties anymore.

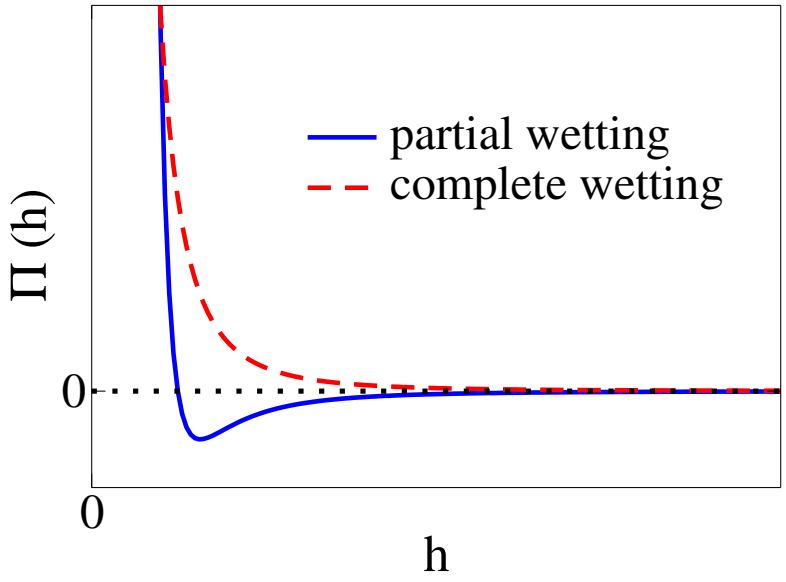


FIGURE 2.3: Schematic plots for two examples of disjoining pressure, modelling partial wetting (blue line) and complete wetting (red line).

In 1960 Derjaguin and coworkers suggested that for the case of ultra-thin films with thickness below 100 nm, an additional energy term $f(h)$ needs to be taken into account [74]. This dependence of the corresponding force on the film thickness leads to an additional repulsion or attraction between the interacting interfaces. It is usually included as an additional pressure term $\Pi = -\frac{\mathrm{d}f(h)}{\mathrm{d}h}$ – the Derjaguin (disjoining) pressure and can be introduced in the normal force boundary condition

as an addition to the curvature pressure, or as an additional body force in the Navier Stokes equation [39, 114][1].

It can be calculated for specific intermolecular interactions. Various expressions for the disjoining pressure exist in the literature [39, 74, 76, 114, 121]. Fig. 2.3 shows a sketch of two commonly used forms of Derjaguin's pressure modeling the cases of partial and complete wetting. For example, if a long-range apolar van der Waals interaction is considered [74, 93, 138, 153, 161, 162], the disjoining pressure has the form

$$\Pi(h) = -\frac{A}{6\pi h^3}, \tag{2.2}$$

where $A$ is the Hamaker constant giving the strength of the interaction. It can be calculated from the optical indices of the involved materials [74]. Note that other sign conventions are also common (cf. e.g. [21, 39, 157]). Other forms of Derjaguin's pressure are found in the literature. Some of them, aimed to model partially wetting liquids, combine destabilising short-range polar interactions and stabilising long-range van der Waals interactions. For example, the combinations of a term $\sim \frac{1}{h^3}$ with a term proportional either to $e^{-h}$ or to $\frac{1}{h^6}$ are commonly used [161, 173].

The conventional Hamaker constant $A$ is defined as a material property that represents the strength of van der Waals interacions between macroscopic bodies. It is measured in [Nm] and typical values of $A$ lie in the range of $10^{-19}$ to $10^{-21}$ Nm for interactions across vacuum. Historically, the Hamaker constant was derived assuming purely additive interactions between the atoms of the involved materials, completely ignoring polarisation effects (Derjaguin, 1934; Hamaker, 1937). A

[1] The original concept of disjoining pressure was first presented in Derjaguin's work from 1936 [32], based on experiments with thin aqueous interlayers formed between two flat mica surfaces. The action of the disjoining pressure is also the reason why liquid helium is known for spreading on almost any surface. If poured in a deep vessel, it climbs the walls of the vessel to eventually leave it. The reason for this behaviour is that the dielectric constant $\epsilon = 1.057$ of liquid helium is lower as compared to the dielectric constant of any other material, different than vapour. The latter implies that there is a repulsive van der Waals force acting across the absorbed liquid helium film which will try to make the film thicker, thus lowering its energy. However, when the helium climbs up the wall this means the gravitational energy will start compensating for the gained van der Waals energy - the film thickness will decrease as the height increases [74].

solution to the problem, completely avoiding the issue of additivity, was later proposed by Lifshitz. He developed a continuum theory which does not consider the atomic structure of the substance [74, 127]. The Lifshitz theory will be discussed in more detail in Section 4.2.1.

Generally, the Hamaker constant can be either positive or negative, resulting in either repulsive or attractive van der Waals interaction. Typical positive values are $A \sim 10^{-21}$ Nm for oil films on glass, quartz or mica [157]. If one considers a liquid film of thickness $\sim$ 1 nm, then the Derjaguin pressure component will be $\Pi \sim 10^6$ kg/ms$^2$. If one, for comparison, considers a sessile spherical oil drop of radius 100 $\mu$m on a solid substrate, the capillary pressure inside the spherical part of the droplet will be 60 kg/ms$^2$. In the three-phase contact line region the Derjaguin pressure is much larger than the capillary pressure and this is the reason for the deviation of the drop shape from the ideal spherical shape in this region.

## 2.2 Derivation of the film thickness evolution equation

The derivation of the film thickness evolution equation in long wave approximation passes through the following steps: At first, the transport equation for the momentum density (Navier-Stokes) and continuity equations are written down together with appropriate boundary conditions. Next, scaling is applied in order to obtain dimensionless equations. A non-dimensional parameter $\epsilon = l/L$ is introduced for long wave scaling, where $l$ and $L$ are the vertical and horizontal length scales. All fields are expanded in series in $\epsilon$ which allows us to solve the transport and continuity equations order by order. Finally, continuity is used to get the film thickness evolution equation.

### 2.2.1 Transport equation for the momentum density

As a starting point for the derivation of the thin film equation we write down the transport equation for the momentum density (Navier-Stokes equation):

$$\rho \frac{\mathrm{d}\mathbf{v}}{\mathrm{d}t} = \nabla \cdot \hat{\tau} + \mathbf{f}, \tag{2.3}$$

where $\mathbf{v} = \begin{pmatrix} u \\ w \end{pmatrix}$ is the velocity field, $\mathbf{f} = \begin{pmatrix} f_1 \\ f_2 \end{pmatrix}$ is the body force field and $\nabla = \begin{pmatrix} \partial_x \\ \partial_z \end{pmatrix}$ in the two–dimensional case, to which we restrict our attention.

The stress tensor has the form:

$$\hat{\tau} = -p\hat{I} + \eta(\nabla\mathbf{v} + (\nabla\mathbf{v})^T), \tag{2.4}$$

where $p(x, z)$ denotes the pressure field and $\hat{I}$ is the identity tensor. The parameters $\rho$ and $\eta$ are the density and the dynamic viscosity of the fluid.

Boundary conditions are set at the solid substrate and at the free surface. The appropriate boundary conditions for the continuous film considered here are as follows [161].

At $z = 0$ (substrate) we choose the no-slip and no-penetration condition:

$$\mathbf{v} = 0. \tag{2.5}$$

This condition implies that at the solid boundary the fluid will have zero velocity relative to the boundary and the solid substrate is impermeable to the fluid - it "sticks" to the surface.

At $z = h(t, x)$ (free surface) we have the kinematic boundary condition:

$$w = \partial_h + u\partial_x h \tag{2.6}$$

and the condition for force equilibrium:

$$\hat{\tau} \cdot \mathbf{n} = \mathbf{n} K\gamma + \mathbf{t}\partial_s \gamma, \tag{2.7}$$

where $\partial_s = \mathbf{t} \cdot \hat{\tau}$, $p_L = -K\gamma$ is the Laplace or curvature pressure and $\partial_s \gamma$ is the variation of the surface tension along the surface. The normal and tangent vector of the surface are

$$\begin{aligned} \mathbf{n} &= \frac{1}{\sqrt{1+(\partial_x h)^2}}(-\partial_x h, 1), \\ \mathbf{t} &= \frac{1}{\sqrt{1+(\partial_x h)^2}}(1, \partial_x h). \end{aligned}$$

The curvature of the surface is

$$K = \frac{\partial_{xx} h}{(1+(\partial_x h)^{3/2}}.$$

Now we can write the vectorial boundary condition (2.7) as two scalar conditions, by simply projecting it onto $\mathbf{n}$ and $\mathbf{t}$, corresponding to normal and tangential force conditions, respectively:

$$\mathbf{n} : p + \frac{2\eta}{1+h_x^2}[-u_x h_x^2 - w_z + h_x(u_z + w_x)] = -\frac{\gamma h_{xx}}{(1+h_x^2)^{3/2}}; \tag{2.8}$$

$$\mathbf{t} : \eta[(u_z + w_x)(1-h_x^2) + 2(w_z - u_x)h_x] = \partial_s \gamma (1+h_x^2). \tag{2.9}$$

### 2.2.2 Dimensionless groups and numbers

In the following table a general set of scaling parameters is introduced [161]:

| | | | | | |
|---|---|---|---|---|---|
| *Dimensionless* | $t'$ | $x'$ | $z'$ | $p'$ | $\mathbf{v}$ |
| *Scale* | $t_0 = \frac{l}{U_0}$ | $l$ | $l$ | $P_0 = \rho U_0^2$ | $U_0$ |
| *Dimensional* | $t = t_0 t'$ | $x = lx'$ | $z = lz'$ | $p = P_0 p$' | $\mathbf{v} = U_0 \mathbf{v}'$ |

Next we now go back to the momentum transport equations (2.3) and introduce the scaled variables to obtain the following expression for its $x$ component:

$$\rho \frac{U_0^2}{l}(u'_t + u'u'_x + w'u'_{z'}) = -\frac{\rho U_0^2}{l} p'_{x'} + \eta \frac{U_0}{l^2}(u'_{x'x'} + u'_{z'z'}) + \rho g \sin\alpha, \tag{2.10}$$

where $\mathbf{f} = \rho\mathbf{g} = \rho g(\sin\alpha, \cos\alpha)$ is assumed for a film or drop on an inclined surface with inclination angle $\alpha$.

Further simplification can be achieved by introducing the dimensionless numbers of Reynolds and Froude:

$$Re = \frac{U_0 l \rho}{\eta}, \qquad Fr = \frac{U_0^2}{lg}. \tag{2.11}$$

Using these non-dimensional numbers, the two components of equation (2.3) become:

$$\begin{aligned} u_t + uu_x + wu_z &= -p_x + \frac{1}{Re}(u_{xx} + u_{zz}) + \frac{\sin\alpha}{Fr}; \\ w_t + ww_x + ww_z &= -p_z + \frac{1}{Re}(w_{xx} + w_{zz}) - \frac{\cos\alpha}{Fr}, \end{aligned} \tag{2.12}$$

where we have dropped the dashes for simplicity.

If one examines these dimensionless numbers, one notices that in this case the Reynolds numbers stands for the ratio of the selected velocity scale and the viscous one, and the Froude number corresponds to the squared ratio of the selected velocity scale and the gravitational one.

This scaling is general unless the used scales $l$ and $U_0$ are specified. All scales introduced above are based on the same length $l$ and velocity $U_0$. However, this is not compulsory. For example, a number of appropriate scales for the case of thin film flowing on an inclined substrate exist, any of which leads to different expressions for the dimensionless numbers. We will use the so called "viscous" scaling based on the viscous velocity scale:

$$U_0 = \frac{\eta}{\rho l}. \tag{2.13}$$

It implies

$$\frac{1}{Re} \to 1, \qquad G := \frac{1}{Fr} \to \frac{gl^3\rho^2}{\eta^2}, \tag{2.14}$$

where $G$ is the Galilei (gravitational) number.

The introduced scaling brings us to the following form of the non-dimensional momentum equations:

$$u_t + uu_x + wu_z = -p_x + u_{xx} + u_{zz} + G\sin\alpha,$$

$$w_t + uw_x + ww_z = -p_z + w_{xx} + w_{zz} - G\cos\alpha. \tag{2.15}$$

The non-dimensional tangential and normal boundary conditions (2.9) and (2.8) become:

$$(u_z + w_x)(1 - h_x^2) + 2(w_z - u_x)h_x = 0; \tag{2.16}$$

$$p + \frac{2}{1+h_x^2}[-u_x h_x^2 - w_z + h_x(u_z + w_x)] = -\frac{1}{Ca}\frac{h_{xx}}{(1+h_x^2)^{3/2}} + \Pi, \tag{2.17}$$

where $Ca = \frac{\eta^2}{\gamma_0 l\rho}$ is the capillary number. Here $\gamma_0$ is defined as $\gamma_0 = \gamma(T_0)$ if a linear dependence of surface tension on temperature is assumed. However, the possibility for dependence of $\gamma$ on the temperature will not be discussed further in the Thesis as no thermal effects will be considered.

$\Pi$ is the Derjaguin's (disjoining/conjoining) pressure introduced in Section 2.1 and it is scaled using the standard pressure scale.

### 2.2.3 Long-wave scaling

Consideration of the geometry of the thin film and particularly the disparity of the length scales leads us to further simplification of the Navier - Stokes equations. The procedure is based on an asymptotic reduction of the full set of governing equations and boundary conditions. The model obtained may not have the mathematical complexity of the original free-boundary problem, but it still preserves many of the important physical features of the described system [161]. In the case of thin film geometry all length scales parallel to the substrate $L$ (e.g. periods of surface waves or drop length), are large if compared to the film thickness $l$. This observation prompts us to introduce the smallness parameter $\epsilon$, defined as follows:

$$\epsilon = \frac{l}{L}, \qquad l \ll L.$$

Next, two separate scales are introduced for the two coordinates $x$ and $z$:

$$x = Lx' = \frac{l}{\epsilon}x', \qquad z = lz'. \tag{2.18}$$

Because of continuity, the velocity components also scale differently:

$$u = U_0 u', \qquad w = \epsilon U_0 w'. \tag{2.19}$$

The time is scaled as

$$t = \frac{L}{U_0} = \frac{l}{\epsilon U_0}t'. \tag{2.20}$$

The rescaled non-dimensional momentum equations have the form

$$\begin{gathered}\epsilon(u_t + uu_t + wu_z) = -\epsilon p_x + \epsilon^2 u_{xx} + u_{zz} + G\sin\alpha; \\ \epsilon^2(w_t + uw_x + ww_z) = -p_z + \epsilon^3 w_{xx} + \epsilon w_{zz} - G\cos\alpha; \\ u_x + w_z = 0.\end{gathered} \tag{2.21}$$

The boundary conditions become

$$(u_z + \epsilon^2 w_x)(1 - \epsilon^2 h_x^2) + 2\epsilon^2 (w_z - u_x) h_x = 0;$$

$$p + \frac{2}{1+\epsilon^2 h_x^2}[-\epsilon^3 u_x h_x^2 - \epsilon w_z + \epsilon h_x (u_z + \epsilon^2 w_x)] = -\frac{1}{Ca}\frac{\epsilon^2 h_{xx}}{(1+\epsilon^2 h_x^2)^{3/2}}; \qquad (2.22)$$

$$w = h_t + u h_x.$$

### 2.2.4 Small inclination or horizontal substrate

The standard procedure for solving the rescaled momentum equations involves expansion of all fields as series in $\epsilon$ so the equations can be solved order by order. The resulting non-linear partial differential equation [15] explicitly contains $\epsilon$ so it consists of terms of different order. The approach used here for studying the situation of a thin liquid film on a slightly inclined or horizontal solid substrate suggests that all physically interesting effects enter the lowest order equations. To achieve this, the dependent variables and dimensionless numbers are rescaled. A new $O(1)$ variable is introduced, considering the inclination of the substrate to be small ($\alpha \ll 1$):

$$\alpha' = \frac{\alpha}{\epsilon} \approx \frac{\sin\alpha}{\epsilon} \quad \Longrightarrow \quad \sin\alpha \to \epsilon\alpha', \quad \cos\alpha \to 1 - O(\epsilon^2)$$

One further chooses

$$Ca' = \frac{Ca}{\epsilon^2}; \qquad \mathbf{v} = \frac{\mathbf{v}'}{\epsilon},$$

where the fact that for small $\alpha$ all velocities are small is taken into account. Now we can drop the dashes and write the transport equations to the lowest order in $\epsilon$:

$$u_{zz} = p_x - G\alpha, \qquad (2.23)$$

$$p_z = -G. \qquad (2.24)$$

The continuity equation writes

$$u_x + w_z = 0. \tag{2.25}$$

The boundary condition at $z = 0$ is

$$u = w = 0. \tag{2.26}$$

The boundary conditions at the surface $z = h(x)$ are written as

$$w = \partial_t h + u\partial_x h, \tag{2.27}$$

$$u_z = 0, \tag{2.28}$$

$$p = -\frac{h_{xx}}{Ca} + \Pi. \tag{2.29}$$

After solving the system, the pressure and velocity fields are obtained:

$$p(x,z) = -Gz + Gh - \Pi(h) - \frac{h_{xx}}{Ca}, \tag{2.30}$$

$$u(x,z) = \left(\frac{z^2}{2} - zh\right)(p_x - G\alpha). \tag{2.31}$$

Finally, from the kinematic boundary condition and continuity equation we obtain

$$\partial_t h = -\partial_x \Gamma, \qquad \Gamma = \int_0^h u dz. \tag{2.32}$$

Here $\Gamma$ is the flow in the laboratory frame. Substituting (2.30) and (2.31) into (2.32), we obtain the general hydrodynamic form of the thickness evolution equation for a film on a slightly inclined substrate:

$$\partial_t h = -\partial_x \left\{ \frac{h^3}{3} \left[ \partial_x \left( \frac{h_{xx}}{Ca} - Gh - \Pi(h) \right) + G\alpha \right] \right\}. \tag{2.33}$$

## 2.3 Hydrodynamic formulation of the thin film equations for simple and complex liquids.

### 2.3.1 Simple liquids on horizontal substrates

Without lateral driving, for dewetting and spreading of simple liquids on a smooth horizontal substrate under the sole influence of capillarity and wettability ($G = 0$), Eq. (2.33) takes the form

$$\partial_t h = -\nabla \cdot \left[ \frac{h^3}{3\eta} \nabla(\gamma \Delta h + \Pi(h)) \right], \tag{2.34}$$

where we have reintroduced the dimensions in order to allow for easier identification of the physical meaning of the individual terms. Here $\eta$ is the dynamic viscosity of the liquid and the pressure term in the brackets on the right hand side consists of the curvature pressure $\gamma \Delta h$ and the disjoining (Derjaguin) pressure $\Pi(h) = -\partial_h f(h)$, modelling wettability.

This equation can be formulated as a gradient dynamics for the film thickness field, which is conserved

$$\partial_t h \; = \; \nabla \cdot \left[ Q(h) \nabla \frac{\delta F}{\delta h} \right], \tag{2.35}$$

where $F[h]$ is the energy functional

$$F[h] \; = \; \int \left[ \frac{\gamma}{2} (\nabla h)^2 + f(h) \right] dV, \tag{2.36}$$

$\frac{\delta}{\delta h}$ is a functional variational derivative with respect to $h$ and $Q(h) = h^3/3\eta$ is the mobility for the case of Poiseuille flow in the film and no-slip boundary conditions at the substrate. Equations of the form of (2.35) exist in various areas and examples include the Cahn-Hilliard equation for the demixing of a binary mixture [30], evolution equations for the density in the framework of Dynamical Density Functional Theory [10, 96], as well as phase field crystals [51, 98, 181].

The gradient form (2.35) of the thin film evolution equation is very versatile - it allows for incorporation of various effects. For example, one can include in (2.36) additional terms accounting for substrate heterogeneties [78, 145, 165], hydrostatic effects [114], temperature differences [18, 115, 167], electrical fields [91, 166], etc.

Recently, experiments involving complex liquids are becoming very popular, due to their numerous potential applications such as ink-jet printing, emulsion stability, in nanofluidics, etc. [57, 66, 135, 136, 183]. Examples of the involved phenomena include dewetting of films and droplets of volatile or non-volatile solutions of polymers or nanoparticle suspensions [42, 191], dewetting of polymer mixtures [55], spreading of drops covered by soluble or insoluble surfactants [159], the spreading of nanoparticle suspensions [188] and nematic liquid crystals [126], etc. In these systems the interfacial effects may couple with diffusive transport of solutes or surfactants, as well as phase separation and evaporation/condensation of the solvent. The theoretical models for systems in which effects like these are involved are still not complete, as suggested in Section 1.

Next, we are going to present a thin film description for a class of complex liquids, e.g. solutions and suspensions in the limit of small concentration, on homogenous horizontal substrates. We are going to discuss how it can be reformulated based on an underlying free energy functional which in consequence will allow us to incorporate additional physical effects.

### 2.3.2 Complex liquids on horizontal substrates

By definition, in the long-wavelength (or long-wave) approximation, all variations along the film are much more gradual than those normal to it, and the variations are slow in time [114]. For the case of a thin film of a non-volatile mixture that partially wets a flat solid substrate, this would imply that all surface slopes and lateral gradients of the film thickness and solute concentration are small. Using the long-wave approximation we arrive at two coupled evolution equations for the thickness of the mixture film $h$ and the local amount of solute $\psi = h\phi$, where $\phi$ is

the vertically averaged solute concentration [53, 187]. They read

$$\partial_t h = \nabla \cdot [Q(h,\phi)\nabla p(h)]\,; \tag{2.37}$$

$$\partial_t(\phi h) = \nabla \cdot [\phi Q(h,\phi)\nabla p(h)] + \nabla \cdot [D(\phi)h\nabla\phi]\,, \tag{2.38}$$

where the mobility is $Q(h,\phi) = h^3/3\eta(\phi)$. The dynamic viscosity may be a constant $\eta(\phi) = \eta_0$ or a possibly strongly non-linear function of the local solute concentration as, e.g., given by the Krieger-Dougherty law [87, 131].

The term on the right hand side of Eq. (2.37) represents the convective flow of the liquid which is driven by the pressure gradient. The pressure term $p(h)$ consists of Laplace and Derjaguin contributions as the one discussed in Section 2.3.1.

The two terms on the right hand side of Eq. (2.38) model convective and diffusive transport of the solute, respectively. $D(\phi)$ is the diffusion coefficient for which the Einstein-Stokes relation is used, i.e. $D(\phi) = k_B T/6\pi r_0 \eta(\phi)$, where $k_B$ is the Boltzmann constant, $T$ the temperature, and $r_0$ – the particle radius.

One may write Eqs. (2.37) and (2.38) in the alternative form

$$\partial_t h = -\nabla \cdot \mathbf{j}_{\text{conv}}, \tag{2.39}$$

$$\partial_t \psi = -\nabla \cdot \left(\frac{\psi}{h}\mathbf{j}_{\text{conv}} + \mathbf{j}_{\text{diff}}\right) \tag{2.40}$$

where

$$\mathbf{j}_{\text{conv}} = -Q(h,\psi)\nabla p(h,\psi), \tag{2.41}$$

$$\mathbf{j}_{\text{diff}} = -D\left(\frac{\psi}{h}\right) h\nabla\left(\frac{\psi}{h}\right). \tag{2.42}$$

For a relaxational system (i.e., a system approaching thermodynamical equilibrium due to energy redistribution in response to external perturbation), the convective $\mathbf{j}_{\text{conv}}$ and the diffusive $\mathbf{j}_{\text{diff}}$ fluxes can be reformulated as a gradient dynamics based

on an underlying free energy functional [163]. In consequence one finds

$$\mathbf{j}_{\text{conv}} = -Q_{hh}\nabla\frac{\delta F}{\delta h} - Q_{h\psi}\nabla\frac{\delta F}{\delta \psi}, \tag{2.43}$$

$$\mathbf{j}_{\text{diff}} = -\check{Q}_{\psi\psi}\nabla\frac{\delta F}{\delta \psi}, \tag{2.44}$$

where the mobility functions are

$$Q_{hh} = \frac{1}{3\eta}h^3, \tag{2.45}$$

$$Q_{h\psi} = \frac{1}{3\eta}h^2\psi, \tag{2.46}$$

$$\check{Q}_{\psi\psi} = \frac{1}{\eta}\widetilde{D}\psi \tag{2.47}$$

and $\eta$ is the dynamical viscosity of the mixture. The $Q_{ij}$ form the symmetric and positive definite mobility matrix

$$\begin{pmatrix} Q_{hh} & Q_{h\psi} \\ Q_{\psi h} & Q_{\psi\psi} \end{pmatrix}, \tag{2.48}$$

where

$$Q_{\psi\psi} = \widehat{Q}_{\psi\psi} + \check{Q}_{\psi\psi} = \frac{h\psi^2}{3\eta} + \frac{\widetilde{D}\psi}{\eta}. \tag{2.49}$$

The viscosity may be constant or depend on the local solute concentration.
In order to obtain Eq. (2.44), the diffusion flux (2.42) is reformulated as a gradient dynamics based on the Helmholtz free energy for an ideal gas, or a medium consisting of non-interacting particles

$$F[\phi] = \int_V \frac{k_b T}{a^3}\phi\ln\phi ds. \tag{2.50}$$

The transport equation for a solute in a bulk situation can be brought into the form

$$\partial_t\phi = \nabla\cdot\left[Q(\phi)\nabla\frac{\delta F[\phi]}{\delta\phi}\right]. \tag{2.51}$$

To recover the diffusion equation, one needs to make an appropriate choice for the mobility function $Q(\phi)$. One chooses $Q(\phi) = -\tilde{D}\phi$, where $\tilde{D}$ is a molecular mobility. The diffusive part of Eq. (2.40) (in the bulk, or simply for imposed fixed $h$) writes $\partial_t \phi = -\nabla \cdot \mathbf{j}_{\text{diff}}$ with $\mathbf{j}_{\text{diff}} = -\tilde{D}\phi\nabla\mu_\phi = -\frac{\tilde{D}k_bT}{a^3} = -D\nabla\phi$, the latter being the classical diffusion equation. Here $\mu_\phi$ is the chemical potential $\mu_\phi = \frac{\delta F[\phi]}{\delta \phi} = \frac{k_bT}{a^3}\ln\phi$.

Thus, equations (2.39) and (2.40) can be reformulated in the form of a gradient dynamics for the two conserved fields $h$ and $\psi$

$$\partial_t h = \nabla \cdot \left[ Q_{hh}\nabla\frac{\delta F}{\delta h} + Q_{h\psi}\nabla\frac{\delta F}{\delta \psi} \right], \tag{2.52}$$

$$\partial_t \psi = \nabla \cdot \left[ Q_{h\psi}\nabla\frac{\delta F}{\delta h} + Q_{\psi\psi}\nabla\frac{\delta F}{\delta \psi} \right]. \tag{2.53}$$

There are other types of relaxational physical systems where the evolution of two coupled fields is described by a set of equations in the same form. A particularly good example is the evolution of a two-layer liquid films [124], and some general results for it can be used for the presently studied system of a film of a mixture, particularly the techniques for the linear stability analysis of homogeneous states.

The formulation, represented by equations (2.52) and (2.53) allows for an incorporation of various physical effects via the inclusion of various terms in the free energy functional. They may account, for instance, for solvent-solute interactions resulting possibly in phase decomposition, concentration-dependent dispersion forces (wettability), entropic terms accounting for mixing in the case of polymers and solutions, etc.

In the following Chapter 3 we are going to employ a variant of Eq.(2.34) that will allow us to study the evolution of evaporating droplets which are "fed" through the substrate and discuss the effects of wettability and capillarity on evaporation.

# Chapter 3

# The relation of steady evaporating drops fed by an influx and freely evaporating drops

In this Chapter we discuss a thin film evolution equation for a wetting evaporating liquid on a smooth solid substrate. The model is valid for slowly evaporating small sessile droplets when thermal effects are insignificant, while wettability and capillarity play a major role. The model is first employed to study steady evaporating drops that are fed locally through the substrate. An asymptotic analysis focuses on the precursor film and the transition region towards the bulk drop and a numerical continuation of steady drops determines their fully non-linear profiles.

Following this, we study the time evolution of freely evaporating drops without influx for several initial drop shapes. As a result we find that drops initially spread if their initial contact angle is larger than the apparent contact angle of large steady evaporating drops with influx. Otherwise they recede right from the beginning.

## 3.1 Introduction

Evaporation of thin liquid films and sessile droplets has attracted much attention both as the way to probe the dynamics of the contact line [88, 141] and as a route to create deposition patterns through sedimentation of solutes and suspensions [40, 41, 71, 169]. A number of studies concentrate on problems pertinent to any evaporation process, which include mass and heat transfer and thermocapillarity [4, 7]. For slowly evaporating small sessile droplets studied in contemporary well-controlled experiments on smooth surfaces [29, 141], thermal effects are, however, insignificant, while contact line dynamics and liquid-substrate interactions play a major role. It has been suggested that the relation between spreading and evaporation/condensation goes both ways, so that the latter may alleviate the notorious contact line singularity [123, 189]. For background on spreading see, e.g., [21, 158].

A remarkable phenomenon observed in evaporating completely wetting liquids is the formation of a dynamic meniscus with a finite contact angle [41]. The standard approach to computing the form of a spreading and evaporating drop and the resulting dynamic contact angle [7, 69, 125] is based on the lubrication approximation with the singularity at the contact line alleviated by slip. The mechanisms limiting the evaporation rate can be of different character. One possibility, realized in the presence of a temperature difference between the substrate and vapor phase [7], is the evaporation rate determined by the balance of latent heat and heat flux. The evaporation rate is then uniform in the limit of small Biot numbers, but diverges near the contact line in the opposite limit. The model, considered in [7] has been earlier applied for the description of isothermal spreading of droplets with unsteady and capillary effects [58]. For thin droplets the evaporation rate is uniform (as long as the layer thickness remains outside the range of intermolecular forces) when evaporation is controlled either by phase transition kinetics at the interface or by diffusion through a boundary layer of constant thickness in a stirred vessel. Another possibility is to consider the diffusion of the liquid vapour away from the droplet to be the evaporation-limiting mechanism. If evaporation is

diffusionally controlled with no stirring, the evaporation rate increases towards the contact line; an analytical solution based on interfacial equilibrium with no flux onto the unwetted substrate yields the flux diverging on the contact line [42, 125]. The approach taken in [48, 49, 148] accounts for the influence of the thermal conductivity of the substrate and the dependence of the vapor saturation concentration on temperature. It generalises the model suggested by [42] by including the effect of evaporative cooling on the vapour saturation concentration at the free surface of the drop, as well as the dependence of the diffusion coefficient of vapour on the atmospheric pressure.

The aim of the present Chapter is to present a simple isothermal thin film evolution equation with evaporation limited by phase transition kinetics (or boundary layer transfer, but not diffusion), that correctly describes the influence of effective molecular interactions on evaporation in the case of complete wetting. This is achieved by taking into account the dependence of the saturated vapor pressure on the disjoining pressure and curvature in the way it has been done in studies of the dynamics of evaporating films [93, 116, 122] but not in the cited studies of droplet spreading. This allows us to describe in a consistent way the transition from the bulk droplet to a precursor layer and eliminate singularities at the contact line. Note however, that our model may be obtained as the isothermal limit of the models in [4, 133], i.e., letting the difference of substrate and ambient temperature, and the latent heat go to zero. It also corresponds to the limit of infinite thermal conductivity of the liquid.

Following [7, 69], we consider a two-dimensional "fed" system that allows us to study steady states of evaporating droplets. These steady states are compared to droplet shapes resulting from a time evolution of an evaporating droplet (without influx). The comparison will be employed to discuss a possible special role the steady state profiles play in the time evolution. A related approach is taken in Ref. [5] where steady fronts of evaporating liquid on an incline are considered.

The Chapter is structured as follows. The following section 3.2 introduces our model and discusses the scaling, whereas section 3.3 discusses the asymptotics

in the precursor film. Section 3.4 discusses the properties of steady drops with influx as a function of the influx strength and of the single remaining dimensionless parameter. The time-evolution in the case without influx is analysed in section 3.5 where we also compare the steady drop profiles in the case with influx to the time-dependent profiles in the non-fed case. Section 3.6 gives our conclusions.

*Note that the model we present here was previously discussed by Pismen [122]. The extension of the model towards including an influx to study steady states was suggested by Thiele and Pismen. Todorova and Thiele calculated the steady states discussed in Section 3.4. Todorova performed the time-dependent simulations introduced in Section 3.5.*

## 3.2 Basic Model and Scaling

For simplicity, we restrict our attention to a two-dimensional system as sketched in Fig. 3.1. Conceptually, there exists no difference to the full three-dimensional system, we only expect the transport rates to change.

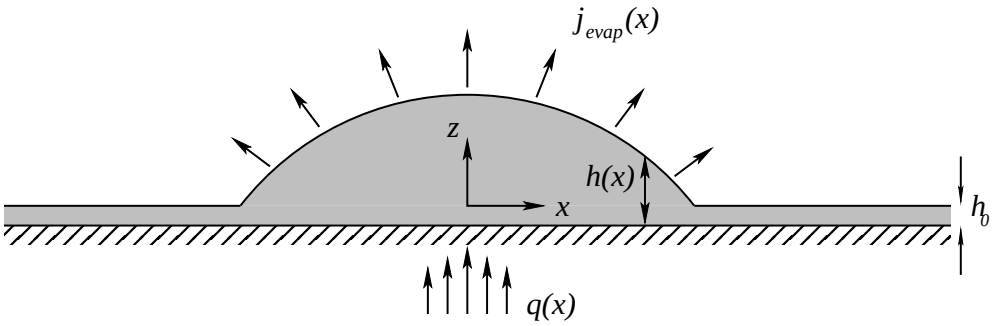


FIGURE 3.1: Sketch of the two-dimensional geometry employed for investigating an evaporating droplet with localised influx $q(x)$.

Using the lubrication approximation, the evaporation dynamics for an isothermal droplet of liquid on a porous substrate is captured by an evolution equation for

the film thickness profile $h$ [93, 114, 122, 162]

$$\begin{aligned} \partial_t h &= -\partial_x j_{\rm conv}(x) - j_{\rm evap}(x) + q(x), && (3.1)\\ j_{\rm conv}(x) &= -\frac{h^3}{3\eta}\,\partial_x p, \qquad j_{\rm evap}(x) = \beta\left(\frac{p}{\rho} - \mu_0\right), \\ p &= -\gamma\,\partial_{xx} h - \Pi(h). && (3.2) \end{aligned}$$

Eq. (3.1) was presented as Eq. (2.34) in Section 2.3.1 without the 2-nd and 3-rd terms on the right hand side. The first and second term on the r.h.s. of Eq. (3.1) are the divergence of the convective flux $j_{\rm conv}(x)$ and the evaporative flux $j_{\rm evap}(x)$, which correspond, respectively, to the conserved and non-conserved part of the dynamics. This form of the evaporative flux implies the evaporation is limited by phase transition kinetics (or boundary layer transfer, but not diffusion). The function $q(x)$ is the influx through the (locally) porous substrate. The evaporative flux is proportional to the difference between the chemical potential of the ambient vapour and the chemical potential in the liquid $\mu = p/\rho$; $p$ is pressure, $\beta$ is an effective evaporation rate constant; and $\gamma$, $\rho$ and $\eta$ are the surface tension, mass density and dynamic viscosity of the liquid, respectively. The pressure $p$ contains the curvature pressure $-\gamma\partial_{xx}h$ and the disjoining pressure $\Pi(h)$ modelling wettability, introduced in Section 2.1; the hydrostatic pressure is neglected as we focus on nano- and micro-droplets.

To model a droplet of completely wetting liquid, we employ a long-range stabilising van der Waals disjoining pressure $\Pi = -A/(6\pi h^3)$ with the Hamaker constant $A < 0$.

The model (3.1) is related to various models in the literature: it may be obtained from the one in [93] by adding an influx and replacing the disjoining pressure for a partially wetting liquid by one for a wetting liquid. The models in [4, 133] incorporate various thermal aspects that are here neglected by assuming that the latent heat is very small or/and the thermal conductivity is very large. The same applies to the steady state description in [105]. Note that our model also corresponds to the one in [133] in the limit of zero superheat.

A dimensionless form of Eqs. (3.1) and (3.2) can be obtained by choosing the characteristic energy density of molecular interactions between the fluid and substrate $\kappa = |A|/(6\pi h_0^3)$ as the pressure scale and the equilibrium film thickness $h_0 = |A/(6\pi\rho\mu_0)|^{1/3}$ corresponding to the ambient vapour potential $\mu_0$ as the scale of film thickness $h$ (note that $\mu_0 < 0$ when a thick flat film evaporates). The horizontal coordinate $x$ and time $t$ can be scaled in several ways [122]. A short horizontal length scale

$$l = \sqrt{\frac{\gamma h_0}{\kappa}} = h_0^2 \sqrt{\frac{6\pi\gamma}{|A|}} = \left(\frac{|A|}{6\pi}\right)^{1/6} \frac{\sqrt{\gamma}}{|\rho\mu_0|^{2/3}} \tag{3.3}$$

is fixed by the balance between disjoining pressure and surface tension at the thickness of the wetting layer, and determines the extent of a region adjacent to the contact line where the interface may be strongly curved due to interaction with the substrate. The lubrication approximation remains formally applicable as long as $l$ far exceeds $h_0$. Note, however, that lubrication approximation often still predicts the qualitative behavior for many systems with larger contact angles [76, 114]. When considering the results obtained with models like Eqs. (3.1), one has always to keep in mind that even very large contact angles obtained in lubrication approximation (measured as slopes at the inflection point of the drop profiles) correspond to rather small angles in physical sense.

Another horizontal scale, applicable in the precursor layer, is determined by the balance of flow driven by the disjoining pressure gradient and evaporation:

$$L = \sqrt{\frac{h_0^3\rho}{\beta\eta}} = \sqrt{\left|\frac{A}{6\pi\mu_0\beta\eta}\right|}. \tag{3.4}$$

This scale is large when evaporation is slow. It is appropriate to choose $L$ as the horizontal scale, assuming it to be of the same order of magnitude as the third available scale – the droplet size. The respective time scale is $T = (L/h_0)^2\eta/\kappa$, and the flux $j_{\mathrm{conv}}$ is scaled by $h_0 L/T$.

Retaining the same notation for the rescaled variables, we rewrite Eqs. (3.1) and (3.2) as

$$\partial_t h = -\partial_x j_{\rm conv}(x) + \left(\epsilon\,\partial_{xx}h + \frac{1}{h^3} - 1\right) + q(x), \tag{3.5}$$

$$j_{\rm conv}(x) = \frac{h^3}{3}\partial_x\left(\epsilon\,\partial_{xx}h + \frac{1}{h^3}\right), \tag{3.6}$$

where the parameter

$$\epsilon = \frac{(6\pi)^{2/3}\gamma\beta\eta}{|A|^{2/3}\rho^{4/3}|\mu_0|^{1/3}} \tag{3.7}$$

denotes the scale ratio $(l/L)^2$. It is proportional to the evaporation rate constant $\beta$, but contains as well a weak dependence on the chemical potential $\mu_0$ in the denominator. Note that the choice of the two length scales $l$ and $L$ does not imply for the parameter $\epsilon$ to be a small number.

In the following we will study steady state droplets that are obtained for an influx $q(x)$ localised at the centre of the drop (section 3.4). Below, the steady profiles are compared to time simulations without influx for different initial profiles (section 3.5). First, however, we discuss the asymptotics in the precursor film.

## 3.3 Asymptotics in the precursor film

In the outer precursor region, the film is almost flat and surface tension can be neglected, i.e., we set $\epsilon = 0$ in Eqs. (3.5) and (3.6) and assume $q(x) = 0$. In the linear regime the film thickness decays exponentially to its equilibrium value $h = 1$:

$$h - 1 \sim \exp(-\sqrt{3}x). \tag{3.8}$$

Note the difference from the non-physical asymptotics $h \sim x^{1/4}$ in [125] where the dependence of the evaporation equilibrium on the disjoining pressure was neglected. The latter profile corresponds to the well-known result of de Gennes [39] who failed to recognise it as an unstable solution.

To discuss the nonlinear behaviour we convert Eqs. (3.5) and (3.6) to the stationary equation

$$\frac{\mathrm{d}^2 \ln h}{\mathrm{d}x^2} = 1 - \frac{1}{h^3}. \tag{3.9}$$

This equation is solved by using $h$ as an independent variable, and $y(h) = (\mathrm{d}\ln h/\mathrm{d}x)^2$ as a dependent variable. The transformed equation is

$$y'(h) = \frac{2}{h}\left(1 - \frac{1}{h^3}\right). \tag{3.10}$$

It is integrated with the boundary condition $y(1) = 0$ to yield

$$y(h) = 2\left[\ln h - \frac{1}{3}\left(1 - \frac{1}{h^3}\right)\right]. \tag{3.11}$$

The precursor film profile is obtained in an implicit form

$$\sqrt{2}x = \int \left[H - \frac{1}{3}\left(1 - \mathrm{e}^{-3H}\right)\right]^{-1/2} \mathrm{d}H, \tag{3.12}$$

where $H = \ln h$. This solution, shown in Fig. 3.2, formally implies a very fast

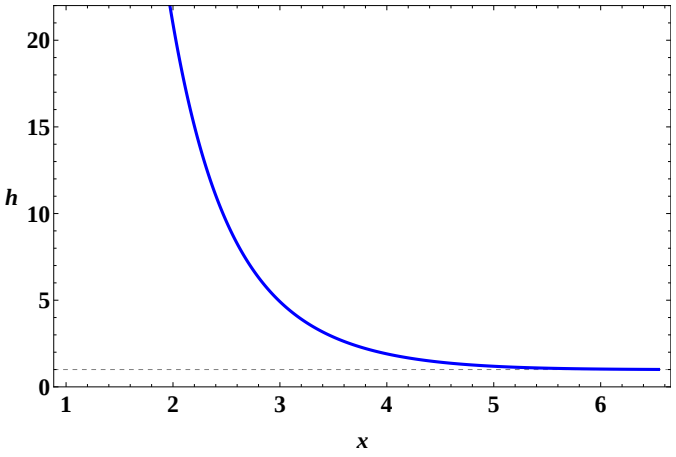


FIGURE 3.2: The solution for the film thickness profile given in an implicit form in Eq. (3.12).

growth $h \sim \exp[(x - x_0)^2]$ towards the bulk of the droplet. It becomes, however, inapplicable as $h$ grows, necessitating a modified scaling. One can see that the two terms in the r.h.s. of Eq. (3.6) become, up to logarithmic corrections, comparable at $h \sim \epsilon^{-1/4}$, which, though appreciably exceeding the thickness of the equilibrium

wetting layer $h = 1$, may be still far below the height of the bulk droplet. As follows from Eq. (3.11), the incline at this thickness level is, up to logarithmic corrections, $h_x = h\sqrt{y(h)} \sim \epsilon^{-1/4}$ in agreement with results by Morris [105, 106]. This sheds light on the origin of a finite contact angle in an evaporating droplet. As we will see below in section 3.4 the numerically obtained dependence agrees well with the asymptotic result.

The flux $J$ from the droplet bulk into the precursor at a "transitional" location $X$ corresponding to the thickness level $h = \epsilon^{-1/4}\zeta$ is determined by the total evaporation rate from the precursor, which can be obtained directly from Eq. (3.9):

$$J = \int_X^\infty \left(1 - \frac{1}{h(x)^3}\right) \mathrm{d}x = -\left(\frac{\mathrm{d}\ln h}{\mathrm{d}x}\right)_{x=X} \approx \sqrt{2\left(\ln\frac{\zeta}{\epsilon^{1/4}} - \frac{1}{3}\right)}. \tag{3.13}$$

The dependence both on $\epsilon$ and on a precise choice of the level $\zeta$ is very weak. The rest of evaporation goes at an almost constant rate from the bulk of a large droplet.

## 3.4 Steady state droplets with influx

For zero influx through the porous substrate ($q(x) = 0$) the only steady state solution is $h = h_0$. However, for $q(x) \neq 0$ steady droplets may exist with a volume determined by the dynamic equilibrium between the overall influx through the substrate and the overall evaporation flux.

Here we use continuation techniques [45–47] to numerically analyse the steady state solutions of Eqs. (3.5) and (3.6), i.e., we set $\partial_t h = 0$ and solve the resulting ordinary differential equation as a boundary value problem on a domain of size $D$ with the boundary conditions (for a symmetrical drop) $\partial_x h = \partial_{xxx} h = 0$ at $x = 0$ (drop centre). At $x = D$ we employ either $h = 1$ and $\partial_x h = 0$, or $\partial_x h = 0$ and $\partial_{xx} h = 0$. If the domain is sufficiently large the results depend neither on the particular choice of $D$ nor on the used version of boundary conditions at $x = D$. For details on the usage of continuation methods for thin film equations

see, e.g., Refs. [170], [75] and [168] where they have been employed to study sliding drops, chemically driven running drops and drops pinned by wettability defects, respectively.

For the influx $q(x)$ we use a normalised Gaussian

$$q(x) = q_0 \frac{2}{\sigma\sqrt{\pi}} \exp\left[-\frac{x^2}{\sigma^2}\right] \tag{3.14}$$

with $q_0 = \int_0^\infty q(x)\mathrm{d}x$ being the total influx through the substrate. If the droplet size is large as compared to the width $\sigma$, the results do not depend on the particular choice of $\sigma$.

In order to produce localized droplets, for a flat film of thickness $h_\mathrm{p} = 1$ (corresponding to the equilibrium film thickness) we continuously increase the parameter $q_0$ from 0 towards a finite value. Next, to investigate the influence of a chosen parameter, we choose one of the solutions produced for chosen value of $q_0$ and vary the parameter of interest.

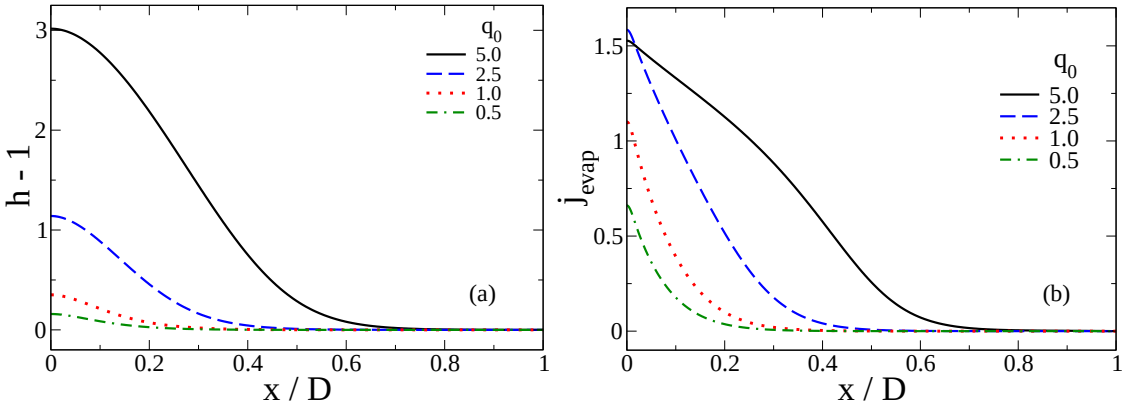


FIGURE 3.3: For the case of small droplets we give (a) droplet profiles and (b) evaporation flux in dependence of position for $\epsilon = 1.0$ and various total influxes $q_0$ as given in the legend. Domain size is $D = 10$, and $\sigma = 0.1$.

Figs. 3.3 and 3.4 show profiles of rather small (nano-)droplets (left panels) and the corresponding dependencies of the evaporative flux on position (right panels). The results are given for various moderate values of the influx $q_0$ (Fig. 3.3) and the length scale ratio $\epsilon$ (Fig. 3.4). In all shown cases these droplets are not much higher than the wetting layer. For such small drops the behaviour is dominated

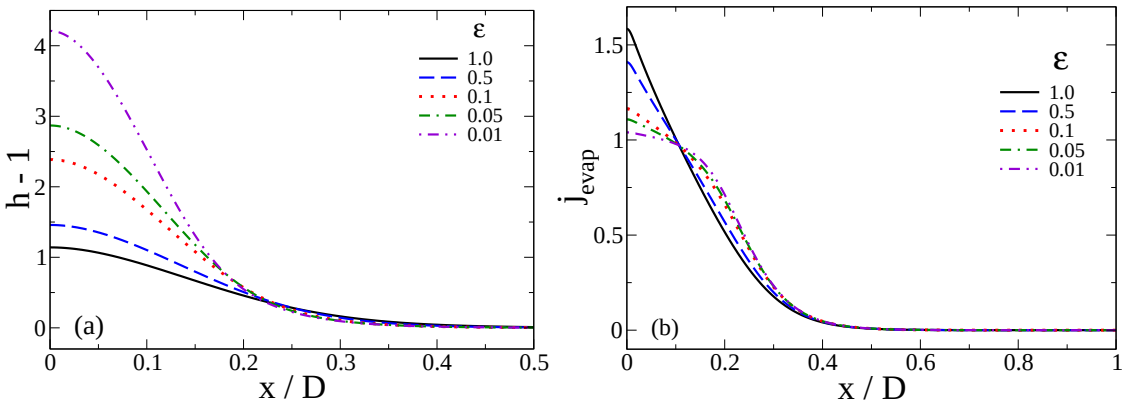


FIGURE 3.4: For the case of small droplets we show (a) droplet profiles and (b) evaporation flux in dependence of position for $q_0 = 2.5$ and various $\epsilon$ as given in the legend. Domain size is $D = 10$, and $\sigma = 0.1$.

by the influence of the disjoining pressure. In consequence, the evaporation decreases monotonically from the center of the drops towards the contact region. Interestingly, in all cases the droplet assumes a shape that does not allow for any condensation of liquid even in the contact line region where the Laplace pressure is negative. Note that there exists a one-to-one correspondence between the strength of the influx $q_0$ and droplet volume for fixed $\epsilon$. This implies that one may characterise the relative size of droplets either by volume or by influx $q_0$.

For extremely small drops (see, e.g., profile for $q_0 = 0.5$ in Fig. 3.3) the disjoining pressure influence is stronger than the capillary pressure even at the drop centre. As a result, the absolute value of the evaporation flux $j_{\text{evap}}$ is smaller than one even at the centre of the drop. For slightly larger drops (see, e.g., profile for $q_0 = 2.5$ in Fig. 3.3) the capillary pressure dominates the disjoining pressure at the drop centre and $j_{\text{evap}}$ is larger than one. With a further increase in drop size the influence of the capillary pressure diminishes and $j_{\text{evap}}$ eventually approaches unity everywhere with the exception of the contact line region (cf. Fig. 3.5). The latter means that with the exception of the contact line region, where the capillarity and wettability play role, the evaporation is controlled exclusively by the equilibrium vapour pressure.

Decreasing $\epsilon$ mainly influences the height of the droplets while the width remains roughly constant [Fig. 3.4(a)]. This implies that the curvature at the drop centre and the apparent contact angle $\theta_{\text{app}}$ (defined as the maximal slope of the drop

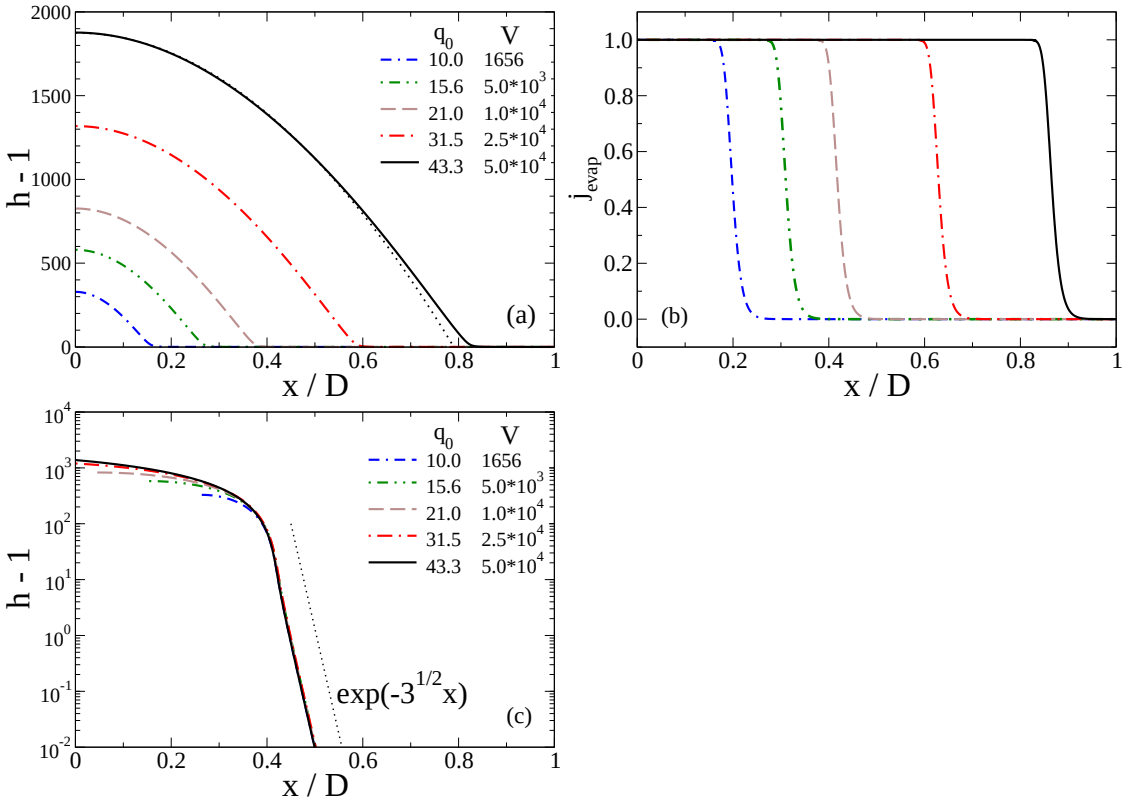


FIGURE 3.5: For the case of large drops we show for $\epsilon = 10^{-6}$ (a) drop profiles and (b) evaporation flux in dependence of position. Results are given for various total influxes $j_0$ and droplet volumes $V$ (see legend). The thin dotted line in (a) gives for the largest drop the corresponding parabolic drop profile of identical maximal height and curvature at centre (corresponding to a spherical cap in lubrication approximation). Panel (c) shows $\log h$ to indicate the universal behaviour near the contact line (drops shifted in $x$). The dotted line indicates the linear result $h - 1 \sim \exp(-\sqrt{3}x)$ [Eq. (3.8)]. Domain size is $D = 50$, and $\sigma = 0.1$.

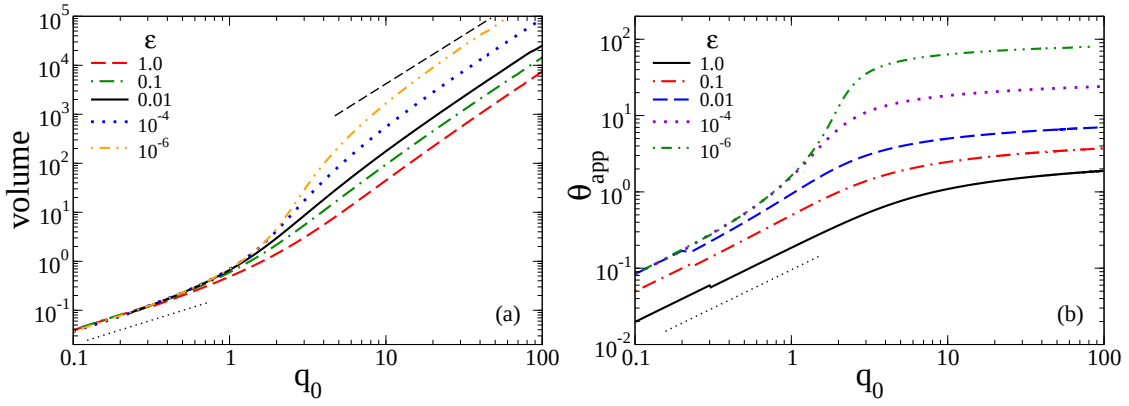


FIGURE 3.6: Shown are (a) drop volume and (b) the apparent contact angle $\theta_{\text{app}}$ (defined as the maximal slope of the drop profile), in dependence of total influx $q_0$ for various length scale ratios $\epsilon$ as given in the legend. The straight dotted [dashed] lines indicate linear [quadratic] dependencies, respectively.

profile), increase with decreasing $\epsilon$. However, although curvature increases we find that the influence of capillarity on the evaporation flux decreases [Fig. 3.4(b)]. For $\epsilon = 0.01$, one has at the drop centre $j_{\text{evap}}$ slightly above one. Furthermore, at the same $\epsilon$, $j_{\text{evap}}$ has already a small plateau at the drop centre, i.e., the flux is nearly constant at the value determined solely by the chemical potential.

The influence of the source width $\sigma$ is marginal as long as it is sufficiently smaller than the droplet width. For moderately large width it has still no influence on the contact line region but has some influence on the center of the drop. Increasing, for instance, $\sigma$ from 0.1 to 1.0 at constant $j_0 = 2.5$ and $\epsilon = 1$ the drop volume goes up by about 5%. Decreasing $\sigma$ down to 0.001 has no visible influence on the droplet shape.

The droplets discussed up to this point represent nano-droplets of heights normally below 500 nm. However, for much smaller $\epsilon$ or much larger $q_0$ one is able to study micro-droplets with heights in the 10-100 $\mu$m range. Fig. 3.5 shows profiles of such drops and the local evaporative flux for $\epsilon = 10^{-6}$. For such large drops the local evaporation is essentially constant for the 'bulk drop' and decreases monotonically in a confined contact region [Fig. 3.5(b)]. Panel (c) of Fig. 3.5 shows the logarithm of $h - 1$. By shifting the drops in the $x$-direction one can appreciate that the approach to $h = 1$ is universal and well described by the linear relation $h - 1 \sim \exp(-\sqrt{3}x)$ derived above (see Eq. (3.8) in section 3.3).

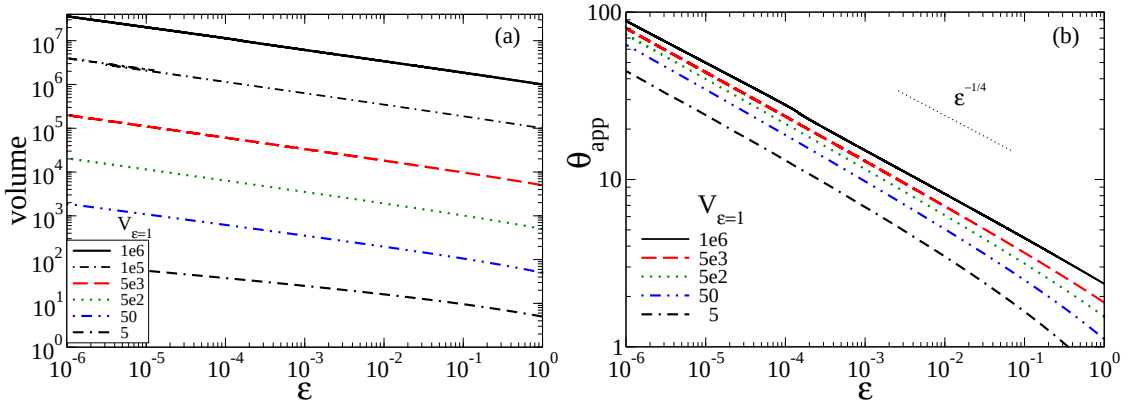


FIGURE 3.7: Shown are (a) drop volume and (b) apparent contact angle in dependence of the length scale ratio $\epsilon$. The total influx $q_0$ is constant for each line, respectively. The lines are characterised by the drop volume at $\epsilon = 1.0$ (see legends).

When increasing the influx for fixed $\epsilon$ the steady drops become larger in width and height [Fig. 3.3(a)]. This is indicated as well by the dependence of volume on influx [Fig. 3.6(a)]. The corresponding apparent contact angle is shown in Fig. 3.6(b). One clearly distinguishes a small-drop and large-drop regime with a crossover at about $V = 1$. In the small-drop regime volume and contact angle are both proportional to the influx. In the large-drop regime the contact angle approaches a constant (or increases with growing influx following a power law with an exponent smaller than 1/5), whereas the volume depends quadratically on influx. The latter is easily explained noticing that the evaporative outflux for large drops is proportional to the surface "area" of the drop (negligible influence of Laplace and disjoining pressure). For a constant contact angle the area under the parabola depends quadratically on its arc length. For the influx to balance the outflux, the surface area has to grow proportionally with the influx, i.e., the volume increases quadratically with the influx.

Inspecting Fig. 3.6 further, one notices that the overall behaviour is different for larger ($\epsilon \gtrsim 10^{-3}$) and smaller ($\epsilon \lesssim 10^{-3}$) drops. In the former case the transition between the small-drop and large-drop regime is monotonic, i.e., the slopes of the curves in Fig. 3.6 change monotonically. In contrast, for small $\epsilon \lesssim 10^{-3}$ in the transition range one may define a third region where the slopes of the $V(q_0)$ and $\theta_{\mathrm{app}}(q_0)$ curves pass through a maximum.

The tendency towards a constant contact angle for increasing volume can also be observed in Figs. 3.7(a) and (b) where we plot the drop volume and the apparent contact angle, respectively, as a function of the length scale ratio $\epsilon$ for various fixed influxes for rather large drops. We find that for large drops, the volume as well as the contact angle decrease for increasing length scale ratio $\epsilon$ roughly as $\epsilon^{-1/4}$. This agrees with the asymptotic expression determined above in Section 3.3.

For smaller drops, deviations from the power law are found at larger $\epsilon$. Interestingly, the dependence of the contact angle on $\epsilon$ seems to approach a limiting curve for large drops. In the following, we employ the curve for the largest drops

in Fig. 3.4 as an approximation to the asymptotic dependence of $\theta_{\text{app}}$ on $\epsilon$ for infinitely large drops.

## 3.5 Time evolution without influx

Next, we study the time evolution of evaporating droplets without influx through the substrate, i.e., we simulate Eq. (3.5) with $q(x) = 0$. The domain size $D$ and boundary conditions at $x = 0$ and $x = D$ correspond to the ones used in the steady state calculations in the previous section. We use three different initial profiles $h_i(x) = h(x, t = 0)$ of equal maximal height $h_m$ and volume $V$: (i) a parabola $h_i(x) = (h_m - 1)(1 - x/x_c)^2 + 1$ with $x_c = 3V/(h_m - 1)$ for $0 \leq x \leq x_c$ and $h_i(x) = 1$ for $x > x_c$; (ii) a Gaussian $h_i(x) = (h_m - 1)\exp((x/\sigma)^2) + 1$ with $\sigma = 2V/\sqrt{\pi}(h_m - 1)$; and (iii) the steady-state solution of identical $V$ and $h_m$ obtained in section 3.4.

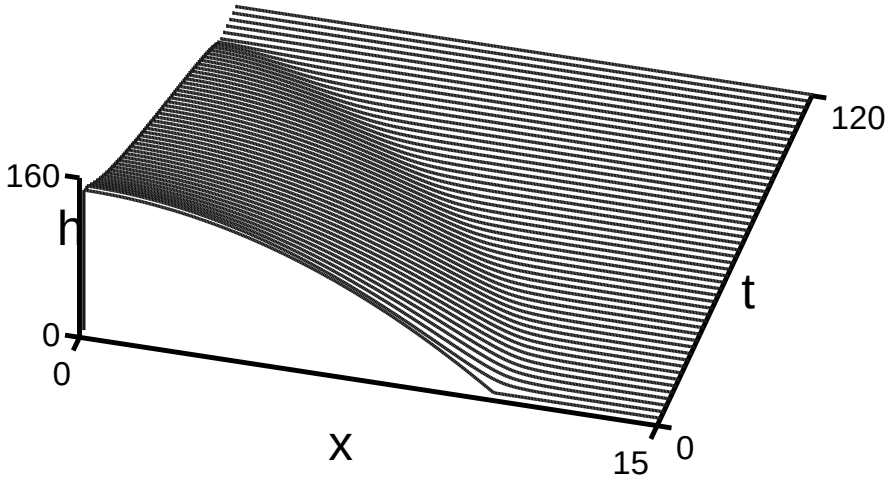


FIGURE 3.8: Space-time plot of an evaporating droplet for $\epsilon = 10^{-4}$. The initial profile is a parabola on a precursor film of thickness $h_p = 1$. It has a volume of $V = 1000$ and maximal height of $H_{\text{max}} = 140.6$. The corresponding contact angle is $\theta_{\text{ini}} = 26.3$. The initial height corresponds to the one at $V = 1000$ for the steady state drops with influx for the corresponding $\epsilon$ (obtained in section 3.4).

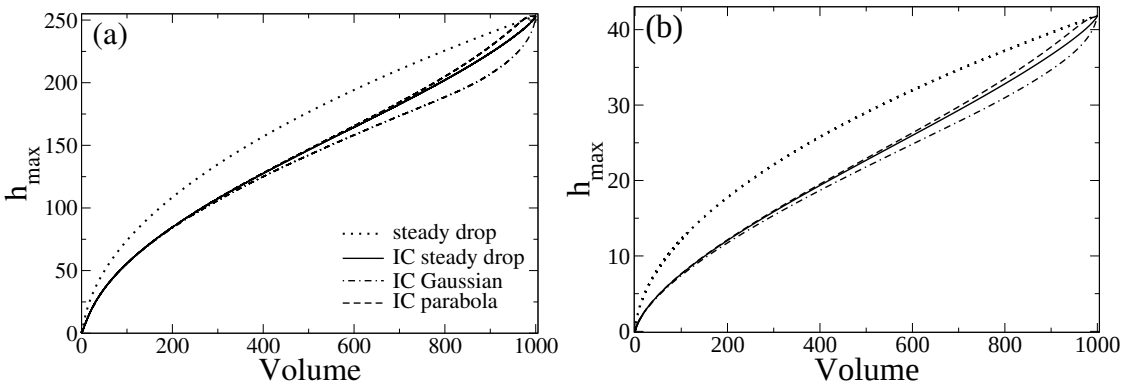


FIGURE 3.9: Trajectories in the phase plane spanned by the maximal drop height and drop volume for (a) $\epsilon = 10^{-6}$ and (b) $\epsilon = 1$. Shown are curves resulting from (i) time evolutions for three different initial profiles of equal maximal height and volume (parabola, Gaussian and steady state with influx), and (ii) calculations of steady state solutions with influx as obtained by continuation.

Fig 3.8 shows a space-time plot for a typical time evolution observed when using an initial parabolic drop profile that has the same height and volume as a fed drop obtained in section 3.4. The case shown is for $\epsilon = 10^{-4}$. At early times the contact line region relaxes under the influence of the disjoining pressure, thereby decreasing the apparent contact angle. Subsequently, the width and height of the drop decrease monotonically until at about $T = 100$ the drop has vanished and only the stable precursor film remains. When starting (as in the present case) with the drop measures (volume and height) as obtained for the drop with influx, the evolution always looks similar. In particular, we have not found that the drop macroscopically spreads at the beginning (by "macroscopic" we mean a spreading that goes beyond the small local relaxation at the contact line).

A more complete picture of the time evolution for different initial profiles is obtained by considering the dependence of overall measures on time, and the trajectories of time evolutions in various "phase planes". For the axes of the latter we choose measures that do not change when the domain size is varied for an identical drop. We give results in two such phase planes, namely, the one spanned by volume and maximal drop height (Fig. 3.9) and the one spanned by maximal drop height and apparent contact angle (Fig. 3.10). The change of the contact angle over time is given in Fig. 3.11, whereas Fig. 3.12 shows selected drop profiles. Figs. 3.9(a) and (b) compare results for very small $\epsilon = 10^{-6}$ and the largest used

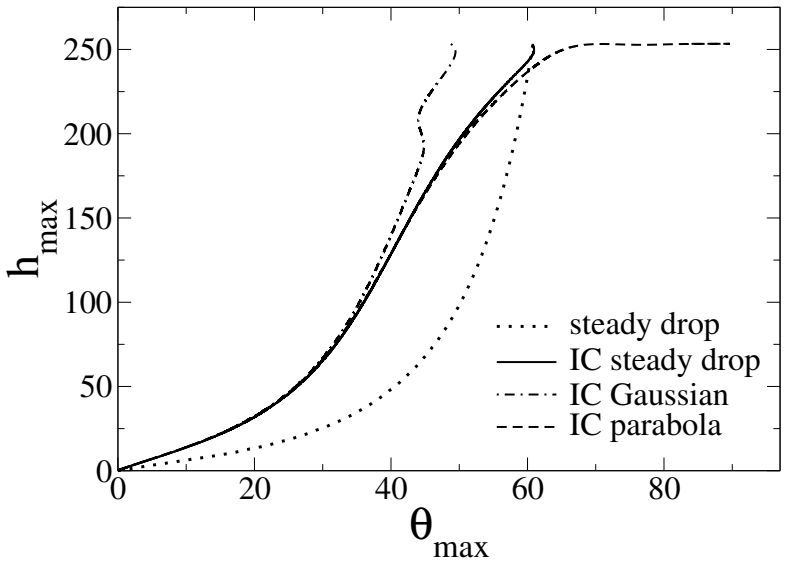


FIGURE 3.10: Trajectories in the phase plane spanned by the maximal drop height and apparent contact angle for $\epsilon = 10^{-6}$. Cases shown correspond to the ones in Fig. 3.9(a).

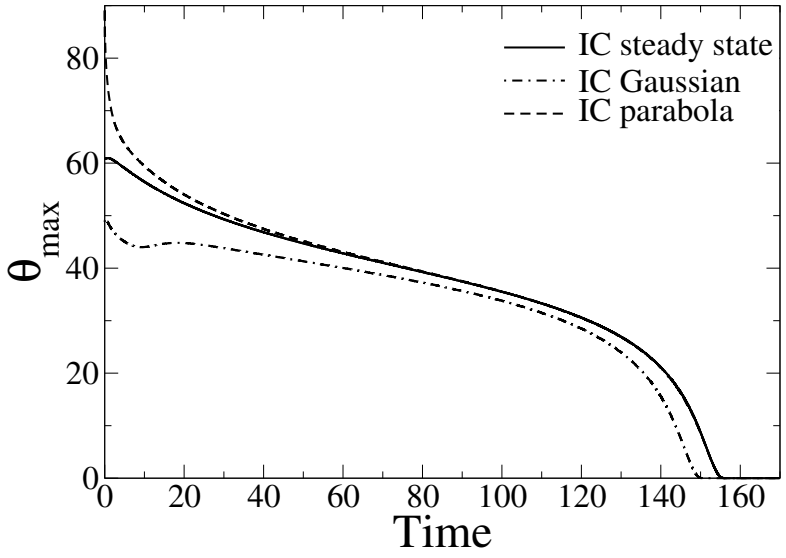


FIGURE 3.11: Shown is the dependence of the apparent contact angle on time for $\epsilon = 10^{-6}$. The given cases correspond to the three evaporating drops in Fig. 3.9(a).

$\epsilon = 1$. As the results are qualitatively rather similar, the remaining figures 3.10 to 3.12 are for $\epsilon = 10^{-6}$ only.

Scrutinising Figs. 3.9 to 3.12 one makes several observations: (i) The time evolutions starting from the three different initial profiles converge after some initial adjustments whose details depend on the particular initial profile shape. (ii) The

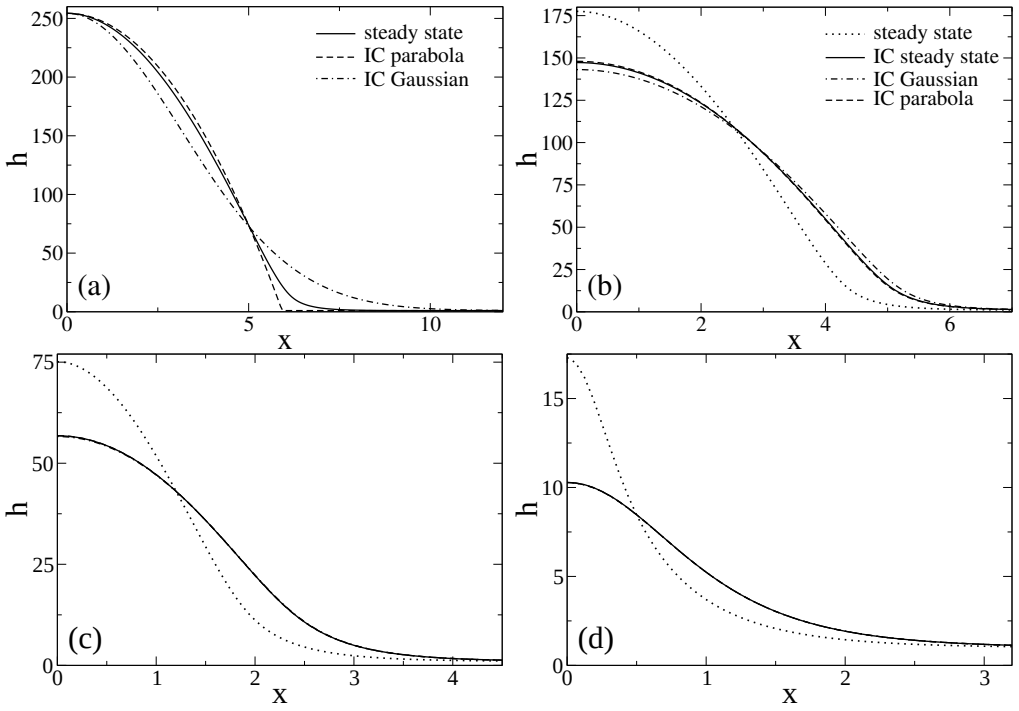


FIGURE 3.12: Given are for $\epsilon = 10^{-6}$ drop profiles for selected drop volumes during the course of evaporation (for the three different initial profiles). We show as well the steady state drop of the same volume. Panel (a) gives the initial profiles at $V = 1000$ whereas panels (b) to (d) show profiles at $V = 500$, $V = 100$, and $V = 10$, respectively.

convergence is slightly faster for smaller $\epsilon$. Here, "faster" means that the trajectories approach each other at higher volume [cf. Fig. 3.9]. In absolute terms the overall evolution becomes faster with increasing $\epsilon$. Thereby, the trajectories of the initial parabola and the initial profile taken from the steady state calculations approach each other earlier than they are approached by the trajectory of the initial Gaussian. (iii) The family of steady profiles with influx represents drops clearly distinct from the unsteady shrinking drops without influx. The family of steady profiles does not approach the trajectories of evaporating profiles when the drops become small. Even for very small drops their contact angle remains always larger by a roughly constant factor than the one of the evaporating drops. The factor is about two for $\epsilon = 10^{-6}$ and approaches four for $\epsilon = 1$. (iv) The overall picture in Fig. 3.9 for different $\epsilon$ looks very similar, only the $h_{\max}$ axes scale differently. A similar observation holds for the representations as given in Figs. 3.10 to 3.12 where, however, both axes would need to be scaled.

Next, we discuss the behaviour of the different initial drop profiles at early times. For larger $\epsilon$ the behaviour is slightly less pronounced, but all the curves look qualitatively the same (not shown). For instance, one obtains a plot that is roughly the one for $\epsilon = 1$ when scaling the $h_{\max}$-axis and $\theta_{\text{app}}$-axis of Fig. 3.10 by factors of 1/6 and 1/40, respectively. A similar rule applies to Fig. 3.11, when additionally scaling time by about 1/5. In Figs. 3.10 and 3.11, one finds for the initial parabola profile a strong decrease in the apparent contact angle at early times. This corresponds to an adjustment of the contact line region to the influences of the disjoining pressure. As the central drop region nearly coincides with the initial steady profile (per definition at same volume and height) the two curves approach each other rather fast. In the course of the time evolution the central part of the profile remains a parabola. However, for the Gaussian at early times the contact angle changes non-monotonically: The profile adjusts on the one hand its contact line region to the disjoining pressure influences (related to the "earlier wiggle" in the curve for the parabola in Fig. 3.10). On the other hand, its central region adapts to a parabola (second "wiggle" in the curve in Fig. 3.10).

All three profiles approach each other after the initial adjustments. Their central part can be well fitted by a parabola, e.g., for $V = 500$ [$V = 100$] and $\epsilon = 10^{-6}$ down to thicknesses of about $h = 60$ [$h = 35$]. Keeping the drop volume constant, that thickness decreases with increasing $\epsilon$ and vice versa. In contrast, the steady profile of the drop with influx can be fitted by a parabola in a smaller central part of the drop. The deviation from the parabola becomes clearly visible, e.g., for $V = 500$ [$V = 100$] and $\epsilon = 10^{-6}$ at about $h = 120$ [$h = 60$] (already 20-30% below the maximum). This percentage range remains roughly the same when changing $\epsilon$ for fixed drop volume.

A comparison of evaporating steady state drops with influx and evaporating drops without influx shows that a freely evaporating shrinking drop has always a smaller apparent contact angle than the steady fed drop. This has been shown for a wide range of length scale ratios from $\epsilon = 10^{-6}$ to $\epsilon = 1$. Note, however, that the differences slowly decrease for decreasing $\epsilon$.

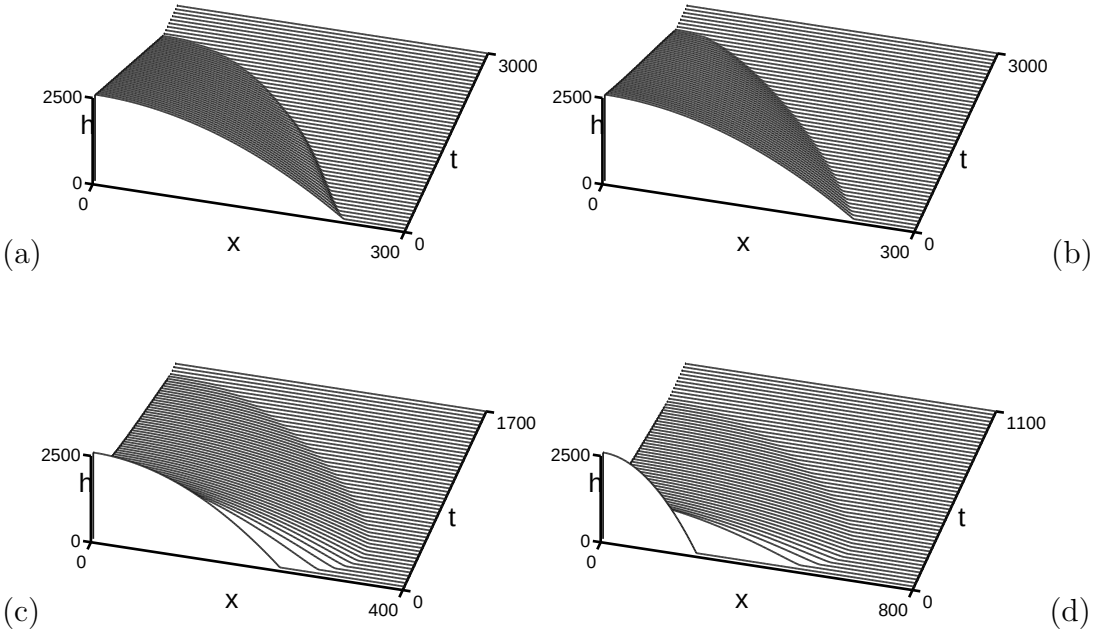


FIGURE 3.13: Space-time plots of an evaporating droplets for (a) $\epsilon = 10^{-6}$, (b) $\epsilon = 10^{-4}$, (c) $\epsilon = 10^{-2}$, and (d) $\epsilon = 1.0$. The initial profile is always the same parabola of maximal height $H_{\max} = 2500$ and volume $4 \times 10^5$ on a precursor film of $h = 1$. The corresponding contact angle is $\theta_{\text{ini}} = 20.8$.

We have observed that freely evaporating drops with a similar initial geometry (volume and height) as per steady-state drops, for the range of $\epsilon$ explored, never spread macroscopically before their contact line recedes. However, an initial spreading phase is often observed in experiments [21, 29, 150]. To investigate this further we perform a number of simulations starting with large parabolic drops. Fig. 3.13 gives a set of space time plots obtained for different length scale ratios from $\epsilon = 10^{-6}$ to $\epsilon = 1$. All of them start from the identical initial profile. For small $\epsilon \lesssim 10^{-3}$ [panels (a) and (b)] the behaviour is very similar to the one described above for drops with the same initial geometry as the steady drops: the drops shrink monotonically, their height and width decrease slowly. However, at larger $\epsilon \gtrsim 10^{-3}$ [panels (c) and (d)] the behaviour is qualitatively different: At early times the drops spread. Thereby they lose height and gain width quite fast, the apparent contact angle decreases strongly. Then the drop reaches a maximal width before the contact line starts to recede again. In the shrinking stage, the height and width of the drop decrease slowly as before. The spreading is faster for

larger $\epsilon$ [Fig. 3.13(d)].

The contact angle for the initial profile is in all cases $\theta_{\text{ini}} = 20.8$. Comparing this with Fig. 3.7(b) one notices that this angle roughly coincides with the limiting contact angle (for large drops) for $\epsilon \approx 3 \times 10^{-4}$. This value lies between the regions (in $\epsilon$) where we find receding and spreading evaporating drops, respectively. Extrapolating from this finding, we formulate the hypothesis that the steady state drops with influx studied above in section 3.4 represent limiting solutions between the case of spreading and shrinking freely evaporating drops (without influx).

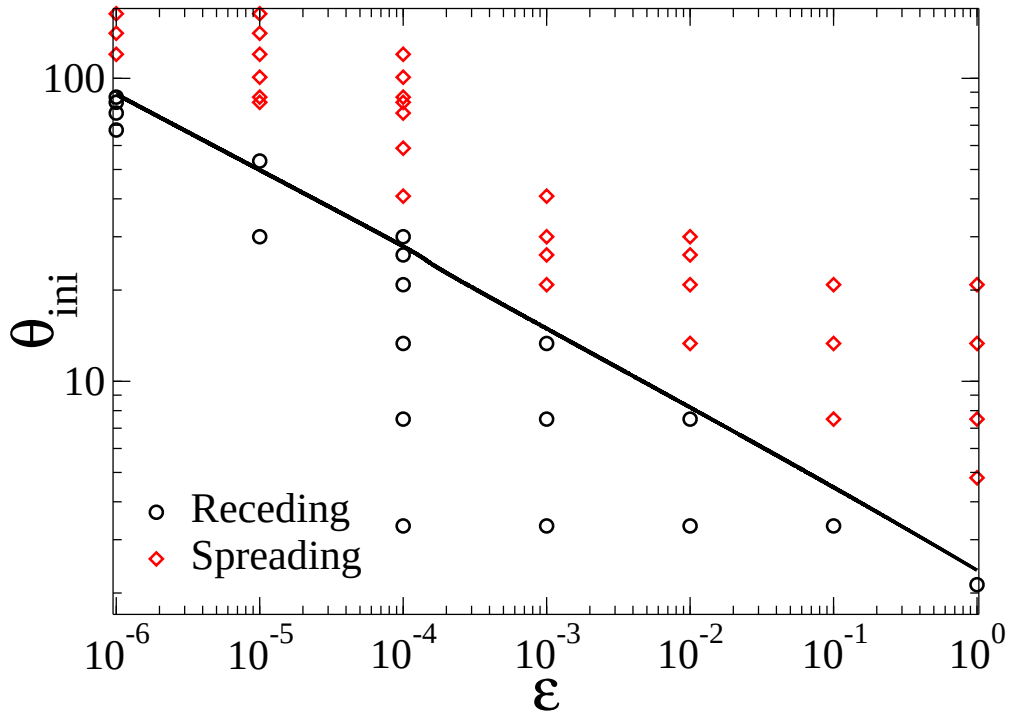


FIGURE 3.14: Phase diagram indicating the initial behaviour of an evaporating drop. In the plane spanned by the initial contact angle $\theta_{\text{ini}}$ and the length scale ratio $\epsilon$ we indicate where the drop initially spreads, and where the contact line recedes right from the beginning. Each symbol corresponds to a time simulation. The solid line corresponds to the numerical result characterising the large steady drops with influx (cf. Fig. 3.7(b)).

To test the hypothesis we perform a number of time simulations with parabolic initial drops of different initial contact angle and at different $\epsilon$. All of them are of the same (large) volume. The results are given as a scatter plot in Fig. 3.14 together with the curve for the large steady drops obtained in section 3.4 [solid line of Fig. 3.7(b)]. For each initial condition we record whether the drop spreads

initially or directly starts to recede. Our results indicate that the above hypothesis seems to hold. The transition between initial spreading for large initial contact angle and a receding of the contact region right from the beginning roughly coincides with the power law dependence $\theta \sim \epsilon^{-1/4}$ (Fig. 3.7(b), curve for large volume) not only in the power but as well in the prefactor. The prefactor of the curve obtained from the steady drops with influx seems to be slightly below the transition found in the time simulations. Further studies will be necessary to give a more detailed account.

## 3.6 Conclusions

We have analysed a thin film evolution equation for a wetting evaporating liquid on a smooth solid substrate. We have focused on slowly evaporating small sessile droplets where thermal effects are insignificant. Employing the model, we have first studied evaporating drops as steady state solutions for the case when they are fed through a porous part of the substrate. In particular, an asymptotic analysis has focused on the transition region between the precursor film and the bulk drop; and a numerical continuation of steady state drops has determined the fully nonlinear drop profiles as a function of the overall influx for various values of the length scale ratio $\epsilon$. We have found that for large steady drops, the volume as well as the apparent contact angle decrease for increasing $\epsilon$ roughly as $\epsilon^{-1/4}$. This agrees well with the scaling $\epsilon^{-1/4}$ determined via the asymptotic analysis. Note that the mentioned logarithmic corrections to both the overlap range where the matching is done and the resulting profile slope (apparent contact angle) are found to have opposite effects and are too subtle for order-of-magnitude estimates.

Furthermore, we have employed the model to study the time evolution of freely evaporating drops that are not fed through the substrate, i.e., the full evolution equation has been numerically integrated. Thereby the time evolution of several different initial drop shapes (for identical maximal height and volume) has been compared. It has been shown that freely evaporating drops with different initial

profiles converge onto certain trajectories in phase space. A comparison of the freely evaporating drops without influx with the evaporating steady state drops with influx has shown that a freely evaporating shrinking drop has always a smaller apparent contact angle than the steady drop with influx. Here this has been investigated for a wide range of length scale ratios from $\epsilon = 10^{-6}$ to $\epsilon = 1$. However, as the differences between the two types of profiles slowly decrease with decreasing $\epsilon$, further studies should scrutinise the case of even smaller $\epsilon$.

We have noted that in our simulations the freely evaporating drops with a similar initial geometry (volume and height) to steady-state drops with influx, never spread macroscopically before their contact line starts to recede and the drop shrinks. As drops undergo an initial spreading phase in many experiments, we have investigated this further and found that drops spread [shrink] from the beginning if their initial contact angle is larger [smaller] than the apparent contact angle of large evaporating drops with influx.

# Chapter 4

# Influence of concentration – dependent wettability of mixtures on film stability and static drop properties

## 4.1 Introduction

In this Chapter we discuss the behaviour of thin films of non-volatile liquid mixtures, colloidal suspensions and polymer solutions on a solid substrate.

The dynamics and stability of thin liquid films has attracted much attention over the last decades as they are of a major importance to numerous technological and industrial applications ranging from biology, chemical industry, pharmaceutic science and geophysics to coating technology and manufacturing of micro– and nanodevices [11, 55, 57, 66, 85, 188]. Typically, the involved liquid films are ultrathin, having thicknesses of the order of 100 nm. At these thicknesses, the issue of stability becomes extremely important as films often become unstable and rupture causing dewetting of the liquid from the substrate. The mechanisms for dewetting can be among (i) *spinodal dewetting* driven by the action of destabilising van

der Waals interactions [13, 103, 134, 146], (ii) *heterogeneous nucleation*, caused by defects on the substrate which can give rise to local gradients in the chemical potential and wettability and lead to formation of holes in the film [27, 78, 147], (iii) density variations, etc [154]. For single-layer free surface films of simple or polymeric liquids [13, 134, 147], experimental results and their theoretical interpretation [17, 100, 142, 172] are well developed. However, the dynamical properties of complex liquids composed of components with different macroscopic properties attract an increasing amount of interest. Popular examples for complex liquids include various mixtures, nanoparticle suspensions, polymer solutions and blends, nematic liquid crystals [24, 41, 42, 55, 104, 110, 124, 126, 175, 186, 191, 192]. In these systems the interfacial effects may couple with diffusive transport of solutes or surfactants, as well as phase separation and evaporation/condensation of the solvent.

The theoretical models for systems in which effects like these are involved are still insufficient. Currently, there exist several long–wave theoretical approaches towards films of mixtures.

One could introduce coupling effects of the film thickness of a colloidal solution and the concentration of the particles by introducing concentration–dependent viscosity [53]. In [36, 97] the authors employ particle concentration–dependent structural disjoining pressures to model spreading of suspensions of nanoparticles. However, this is done by directly replacing the disjoining pressure $\Pi(h)$ in the dynamical equations by an expression $\Pi(h, \phi)$ depending both on the film thickness $h$ and the height–averaged particle concentration $\phi$. As is will become clear from the forthcoming Section 4.3, and also as suggested in [163], in order to obtain a consistent description it is crucial that one includes such a dependence in the local free energy $f(h)$ (cf. Eq. (2.36)), which results into additional coupling terms in the coupled evolution equations for the film thickness and concentration.

In his *ad hoc* model Clarke [34, 35, 175] postulates coupled equations for the film height and mean solute concentration to model the combined effects of phase separation and dewetting. The model is based on an energy functional which

is similar to the one used in [163] and discussed in Section 2.3.2 of this Thesis. However, the dynamical equations from [35] describe the time evolution in terms of the conserved field $h$ and the non-conserved local concentration $\phi$ and they do not agree with our system of equations (2.52) and (2.53), which expreses the time evolution of the fields $h$ and $\psi = h\phi$ that are both conserved. We are unable to see how in the limit of non-interacting solute molecules these equations will result in the hydrodynamic equations (2.37) and (2.38).

In [112] the authors develop a variational approach, based on a long–wave expansion of model-H (which couples fluid flow with the convective Cahn–Hilliard equation), which aims to describe the effects of coupling between dewetting and decomposition.

The lubrication model presented in [23] investigates the dynamics of thin film of mixtures of binary mixtures with and without heat transport, without evaporation. The authors derive coupled equations describing the evolution of the free surface and the mean concentration. They study component separation induced by the Soret effect (formation of a mass flux due to a temperature gradient) in heated films and the fusion and mixing of two thin films of perfectly mixing components in the isothermal case.

In this Chapter we develop a thin film description for solutions and suspensions that accounts for concentration–dependent wettability (cf. Fig. 4.1).

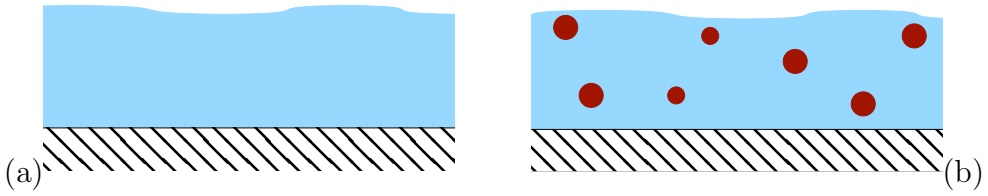


FIGURE 4.1: A sketch of a solid substrate covered by a thin film of (a) a simple liquid and (b) a mixture. A major question we are investigating is how the wetting behaviour of the two types of systems differ.

In Section 4.2 we discuss a way to obtain a concentration–dependent Hamaker constant, hence a height– and concentration–dependent Derjaguin (disjoining) pressure. This is achieved by combining the classical theory of effective molecular interactions between the free surface of the film and the smooth solid substrate, which we discuss in Section 4.2.1, with homogenisation techniques to obtain effective optical characteristics, which we introduce in Section 4.2.2. In Sections 4.2.3 and 4.2.4 we show how the dependence of the Hamaker constant on the concentration can be approximated by a linear function and applied to some selected mixtures. We continue in Section 4.3 by introducing coupled dynamical equations for films and drops of mixtures and in Section 4.4 we discuss how they can be non-dimensionalised. Further, in Section 4.5 we perform a linear stability analysis of a flat homogeneous film with solute. In particular, we investigate how the stability thresholds are influenced by the incorporation of the additional degree of freedom related to the concentration field. We discuss how one can obtain coexisting states (binodals) for the case of mixtures in Section 4.6. As we study the effects of the solute on the stability of the system, we differentiate two main cases of interest - a pure solvent which is either (i) stable or (ii) unstable on its own. In Section 4.7 we present our results from the linear stability analysis and discuss non-linear thickness and concetration profiles, binodal lines and time evolution for cases (i) and (ii). Finally, in Section 4.8 we give our conclusions.

The work presented in this Chapter involved a collaboration with Dr. Hender Lòpez at Loughborough University. He contributed with the time–dependent numerical simulations, some results from which are presented and discussed in Section 4.7.

## 4.2 Hamaker constants of mixtures

We consider thin films of suspensions or solutions, which we will refer to as "**mixtures**". The components of the mixture we will call "**solvent**" and "**solute**", where the latter represents the phase used to modulate the wetting properties

of the reference state of pure solvent. In Fig. 4.2 a sketch of a three-component system is shown. The components are marked "1", "2" and "3", where "1" is a smooth solid substrate, "2" is a gas (or vacuum) phase and "3" is a film of a mixture of two materials. First, we consider the case when component "3" is a

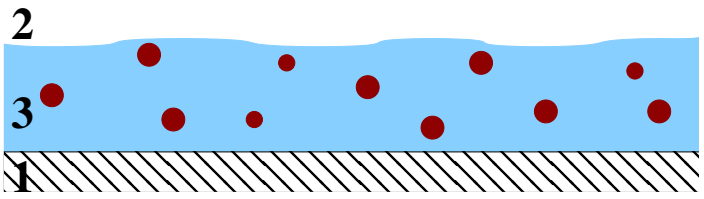


FIGURE 4.2: A sketch of a 3–component system, where one of the components is a mixture. The whole system is characterised by a Hamaker constant $A_{123}(\phi_0)$, where $\phi_0$ is the mean solute concentration, measured as a volume fraction.

film of a pure liquid and discuss the intermolecular forces acting in the system in the framework of the Lifshitz theory.

### 4.2.1 Lifshitz theory

The Hamaker constants, characterising the strength of van der Waals forces between macroscopic bodies in vacuum or air, can be estimated using Hamaker's method derived assuming pairwise additivity of the interactions [74]. Although conceptually simple, this method is not really accurate and is not applicable for the types of systems we are interested in. Hamaker's method neglects many-body interactions along with entropic contributions and other factors. These effects are taken into consideration in the alternative and complicated theoretical method suggested by Lifshitz and coworkers in 1961 [74]. The interacting particles and surrounding media are treated as continuous phases and the interactions in the system are considered to arise from the interference between fluctuating electromagnetic fields which extend beyond the surfaces of the particles. In that way, the Hamaker constants are calculated as functions of the frequency-dependent bulk dielectric fields characterising the continuous phases. Namely, Lifshitz's theory of van der Waals forces uses as input parameters the dielectric permittivities and refractive indices of the materials comprising the system (Fig. 4.3). The approxi-

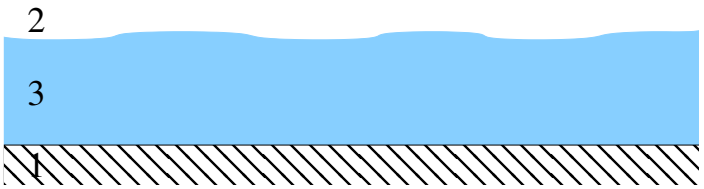


FIGURE 4.3: Sketch of a 3–component system characterised by a Hamaker constant $A_{123}$, where component "3" consists of a pure liquid.

mated expression for the 3-component Hamaker constant of such a system is

$$A_{123} = \frac{3k_bT}{4}\left(\frac{\epsilon_1-\epsilon_3}{\epsilon_1+\epsilon_3}\right)\left(\frac{\epsilon_2-\epsilon_3}{\epsilon_2+\epsilon_3}\right)$$
$$+\frac{3h\nu_e}{8\sqrt{2}}\frac{(n_1^2-n_3^2)(n_2^2-n_3^2)}{\sqrt{(n_1^2+n_3^2)(n_2^2+n_3^2)}\left(\sqrt{n_1^2+n_3^2}+\sqrt{n_2^2+n_3^2}\right)}. \tag{4.1}$$

Here $\nu_e$ is the main electronic absorption frequency in the UV range of the optical spectrum with a typical value of $3\times10^{15}s^{-1}$ and it is assumed that all the materials in the system have the same main electronic absorption frequency [74]; $k_b$ stands for the Boltzmann constant and $h$ is Planck's constant, known from quantum mechanics; $n_i$ and $\epsilon_i$ are the refractive indices and dielectric constants, respectively, of the material number $i$ with $i = 1, 2, 3$ [74].

The values of the optical constants are measured and documented for many materials. However, in the case when any of the 3 components of the system consists of a mixture of 2 or more materials, Eq. (4.1) can not be applied directly. We use homogenisation techniques in order to obtain effective values for $n$ and $\epsilon$ of the mixture as functions of the optical parameters of its components and their volume fraction.

### 4.2.2 Effective Medium Approximation

The effective medium approximation (EMA) is a tool, broadly used for the calculation of the effective optical parameters of non-homogeneous substances [26, 65, 113]. The non-homogeneous medium is treated as an effective one, having the

same dielectric response as the system of interest (Fig. 4.4). The dielectric constant and refractive index of the effective system are calculated based on the ones of its components, assuming a certain model which accounts for the interaction between the components and the geometry of the arrangement.

Various effective medium theories exist, that consider different types of microstructure of the mixture ([26, 113, 176]). These models use the definition of an effective medium, according to which a random cell, embedded in the effective medium, should not be detectable experimentally with electromagnetic radiation in a certain range of wavelengths [113]. However, we will not enter into details about the derivation of the existing models and we will readily use the final formulas for the effective constants, characterising the effective medium.

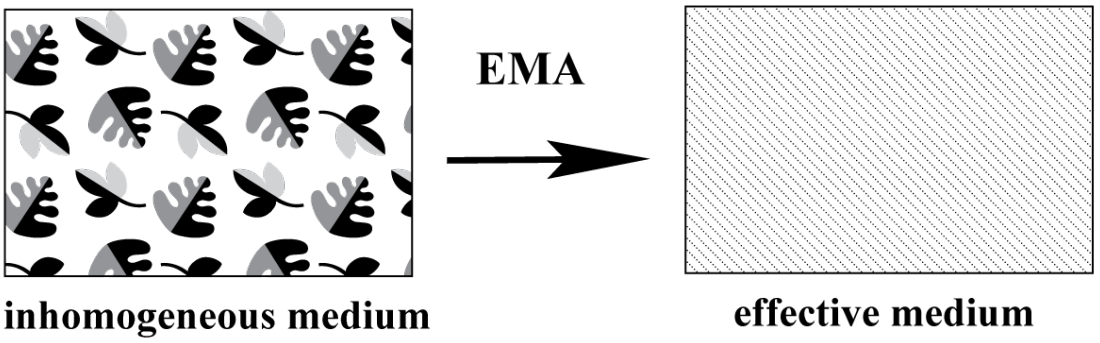


FIGURE 4.4: The effective medium approximation (EMA) as a general tool for the homogenisation of inhomogeneous media.

### A) Maxwell – Garnett mixing rule

There exists a model, called the Maxwell-Garnett mixing rule, where the heterogeneous medium is treated non-symmetrically regarding its components, i.e. the solvent is treated as a continuous medium and the solute is treated as an inclusion [26, 113]. This assumption makes the use of the model reasonable only in the limit of small concentrations. According to Maxwell – Garnett, the heterogeneous system is optically equivalent to an effective system with dielectric constant $\epsilon_{\text{eff}}$,

which solves the equation

$$\frac{\epsilon_{\text{eff}} - \epsilon_a}{\epsilon_{\text{eff}} + 2\epsilon_a} = \phi_0 \frac{\epsilon_b - \epsilon_a}{\epsilon_b + 2\epsilon_a}, \tag{4.2}$$

where $\epsilon_a$ and $\epsilon_b$ are the dielectric constants of the solvent (or material "$a$") and solute (material "$b$"), respectively, and $\phi_0$ stands for the normalised bulk concentration of the solute in the system, measured as volume fraction.

**B) Bruggeman's mixing rule**

Another setup, considered by Bruggeman, allows for all concentrations of the solute in the range $[0, 1]$, as it is completely symmetric regarding the components of the mixture [26, 113]. The effective dielectric constant is calculated from the equation

$$(1 - \phi_0) \frac{\epsilon_a - \epsilon_{\text{eff}}}{\epsilon_a + 2\epsilon_{\text{eff}}} = \phi_0 \frac{\epsilon_{\text{eff}} - \epsilon_b}{\epsilon_b + 2\epsilon_{\text{eff}}}, \tag{4.3}$$

where the same notations as in Eq. (4.2) are used.

We assume that Eqs. (4.2) and (4.3) are valid when replacing the dielectric constants with the respective squared refractive indices, i.e. $\epsilon_i = n_i^2$. This assumption is reasonable when the imaginary parts of the refractive indices are negligible, which is the case for many systems of interest to us, such as polymer mixtures, some nanoparticle suspensions and solutions.

### 4.2.3 Hamaker constant as a function of solute concentration.

Solving Eqs. (4.2) or (4.3) with respect to the effective optical constants of the mixture allows us to substitute the obtained values directly into Eq. (4.1). Thus

we arrive at the expression

$$A_{123}(\phi_0) = \frac{3k_bT}{4}\left(\frac{\epsilon_1 - \epsilon_{\rm eff}(\phi_0)}{\epsilon_1 + \epsilon_{\rm eff}(\phi_0)}\right)\left(\frac{\epsilon_2 - \epsilon_{\rm eff}(\phi_0)}{\epsilon_2 + \epsilon_{\rm eff}(\phi_0)}\right)$$
$$+\frac{3h\nu_e}{8\sqrt{2}}\frac{(n_1^2 - n_{\rm eff}^2(\phi_0))(n_2^2 - n_{\rm eff}^2(\phi_0))}{\sqrt{(n_1^2 + n_{\rm eff}^2(\phi_0))(n_2^2 + n_{\rm eff}^2(\phi_0))}\left(\sqrt{n_1^2 + n_{\rm eff}^2(\phi_0)} + \sqrt{n_2^2 + n_{\rm eff}^2(\phi_0)}\right)}, \quad (4.4)$$

which allows us to calculate the concentration–dependent 3–component Hamaker constant for the interaction of two media 1 and 2 across a medium 3 that is itself a mixture of components "$a$" and "$b$", characterised by the concentration of the second component $\phi_0$ (Fig. 4.2). Here $\nu_e$ is the main electronic absorption frequency of the solvent.

### 4.2.4 Results for selected mixtures

Since data for the dielectric constants and refractive indices of many pure materials can be found in the literature ([2, 74] and references therein), we can now use Eq. (4.4) to determine how the Hamaker (4.4) changes over the whole concentration range $0 \leq \phi_0 \leq 1$. As from now on we consider systems where the solid substrate interacts with the gas phase across a mixture film, we denote the corresponding Hamaker constants by $A_{\rm smg}$ (**s**olid-**m**ixture-**g**as).

Table 4.1 provides the optical constants for the materials we use in our calculations. For the systems we explore, we find that the results for $A_{\rm smg}(\phi_0)$ do practically not depend on the particular EMA model used. Therefore from now on we only use Bruggeman's approximation (4.3).

The suggested scheme allows us to model the Hamaker constants for various types of systems and depending on the optical properties of the components, we observe versatile behaviour of $A_{\rm smg}(\phi_0)$, as shown in Figs. 4.5 – 4.7. For example, if we consider a silicon substrate with a layer of mixed toluene and polystyrene (PS) under air, we observe a Hamaker constant that monotonically decreases with increasing PS concentration (see solid red line in Fig. 4.5).

| material | ε | n |
|---|---|---|
| polystyrene (PS) | 2.55 | 1.59 |
| poly(methyl methacrylate) (PMMA) | 2.90 | 1.49 |
| poly(styrene-co-acrylonitrile) (PSAN) | 8.30 | 1.58 |
| Poly(vinylmethylether) (PVME) | 5.90 | 1.47 |
| toluene | 2.40 | 1.50 |
| acetone | 21.00 | 1.36 |
| silicon (Si) | 11.90 | 4.11 |
| silicon oxide (SiO) | 5.50 | 1.48 |

TABLE 4.1: Dielectric constants $\epsilon$ and refractive indices $n$ of some typical polymers, solvents and solid substrate materials.

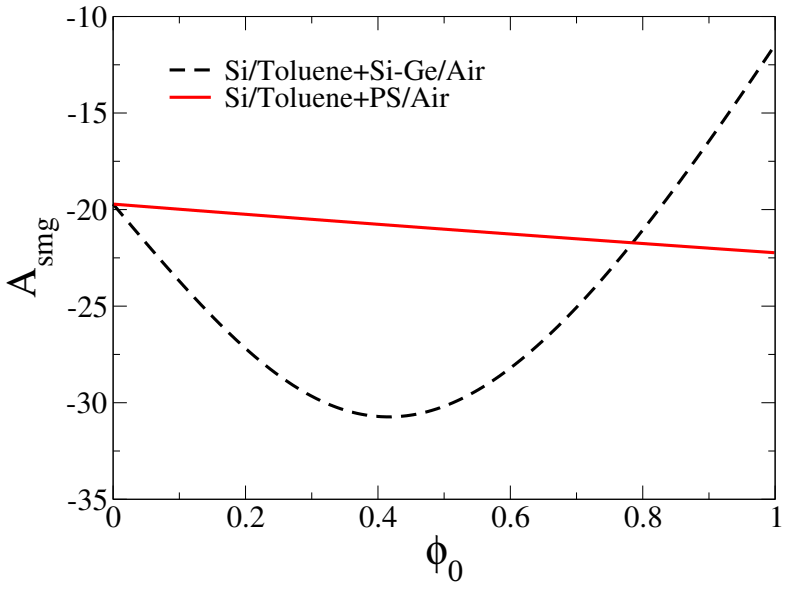


FIGURE 4.5: The 3-component Hamaker constant $10^{20} \times A_{\rm smg}$ [N.m] for Si/ Toluene+PS/ Air (solid line) and Si/ Toluene+Si-Ge/ Air (dashed line) in dependence of the mean concentration $\phi_0$ of the solute, measured as volume fraction.

Interestingly, when we replace the polystyrene in the system with Si-Ge semiconductor crystaline nanoparticles, the Hamaker constant exhibits a minimum at a certain concentration of the particles (dashed black line in Fig. 4.5). The reason for

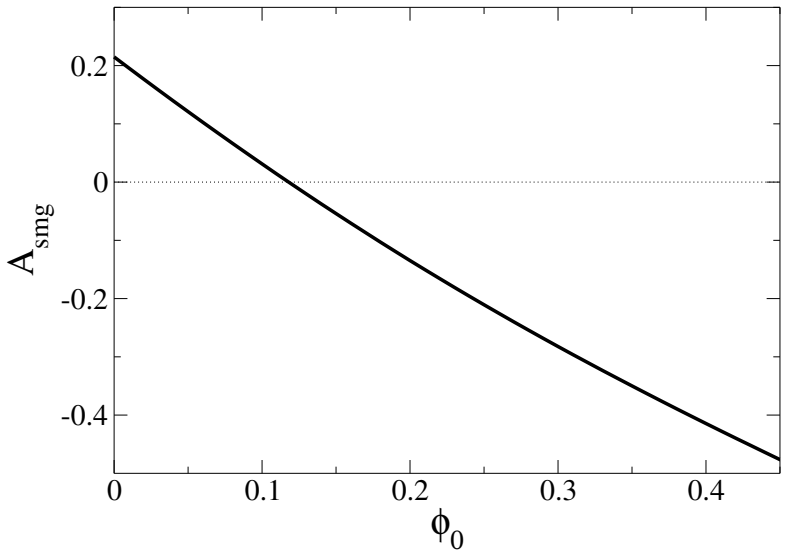


FIGURE 4.6: The 3-component Hamaker constant $10^{20} \times A_{\text{smg}}$ [N.m] for SiO/ Toluene+Acetone/ Air in dependence of the mean concentration $\phi_0$ of the solute, measured as volume fraction.

this behaviour can be found in the dramatic difference between the optical properties of the solvent and the semiconductor, resulting in non-monotonic behaviour of the effective dielectric constant and effective refractive index of the mixture ($\epsilon_{\text{eff}}$ and $n_{\text{eff}}$, respectively, and hence the Hamaker constant (4.4) of the system.

Another interesting situation is shown in Fig. 4.6, which represents the dependence on the Hamaker constant $A_{\text{smg}}$ of a system with a mixture of toluene and acetone over the concentration $\phi_0$ of acetone. The pure toluene is unstable on a SiO substrate ($A_{\text{smg}}(0) > 0$), but the addition of solute reduces $A_{\text{smg}}$ and eventually for a certain concentration it becomes negative, which means a film of the mixture becomes stable (assuming it stays homogeneous).

If the optical indices of the solvent and solute are similar, then we can confidently approximate the dependence of $A_{\text{smg}}$ on $\phi_0$ with a linear function, i.e.

$$A(\phi_0) = |A_0|(\delta + M_1\phi_0), \quad \text{where} \quad \delta = \pm 1. \tag{4.5}$$

Fig. 4.7 shows as an example the case of a PMMA/PS polymer blend on a SiO substrate under air. The dependence of the Hamaker constant on concentration,

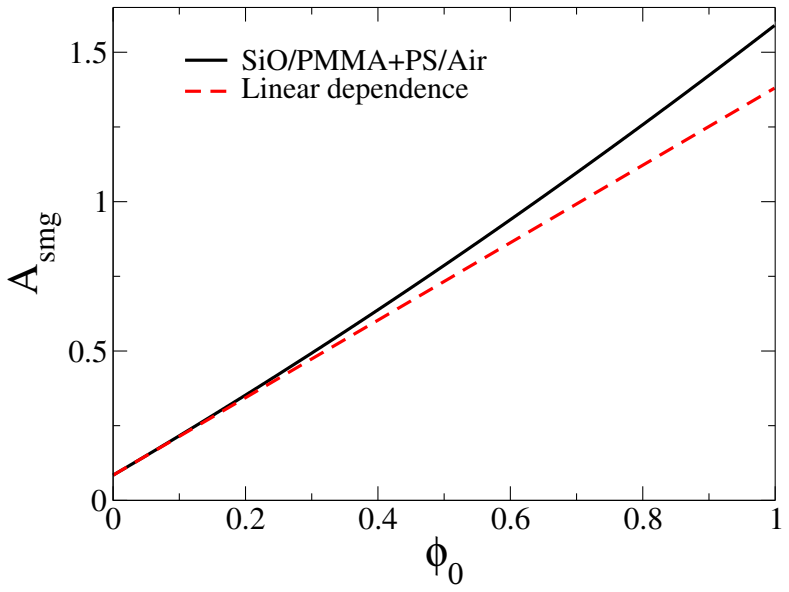


FIGURE 4.7: The 3-component Hamaker constant $10^{20} \times A_{\text{smg}}$ [N.m] for SiO/ PMMA+PS /Air in dependence of the mean concentration $\phi_0$ of the solute, measured as volume fraction (solid black line). The dashed red line represents a linear approximation of $A_{\text{smg}}$.

calculated using Eq. (4.4) with $\epsilon_{\text{eff}}$ and $n_{\text{eff}}$ determined from Eq. (4.3), is represented by the solid black curve, while the dashed red line corresponds to a linear approximation. Obviously, in the range of relatively small concentrations ($\phi_0 < 0.2$) the two curves coincide and even for $\phi_0 > 0.2$ the approximation is still reasonable.

Table 4.2 gives the results for ten different combinations of substrates and mixture components, where in all cases the gas phase is chosen to be air. The notations "$A_{\text{mgm}}$" and "$A_{\text{sms}}$" correspond to the symmetric cases where two slabs of mixture are separated by a gas layer and vice versa (**m**ixture-**g**as-**m**ixture and **s**olid-**m**ixture-**s**olid, respectively) and are given for completeness. As demonstrated in Figs. 4.5, 4.6 and 4.7 and Table 4.2, $A_{\text{smg}}$ can be either positive or negative. We will see below in Section 4.3 that this corresponds to unstable or stable film configurations, respectively, but only if assuming that the films remain always homogeneous.

| Sub | Mixture | | Asmg [N.m] | | Amgm [N.m] | | Asms [N.m] | |
|---|---|---|---|---|---|---|---|---|
| | solvent | solute | $\delta\|A_{smg_0}\|$ | $M_1$ | $\delta\|A_{mgm_0}\|$ | $M_1$ | $\delta\|A_{sms_0}\|$ | $M_1$ |
| SiO | PS | PMMA | 1.59E-20 | -1.1 | 9.31E-20 | -0.28 | 3.32E-21 | -1.62 |
| SiO | PMMA | PS | 8.44E-22 | 15.4 | 6.83E-20 | 0.34 | 3.12E-22 | 1.92 |
| Si | PS | PMMA | -2.22E-19 | -0.1 | 9.31E-20 | -0.28 | 6.34E-19 | 0.07 |
| Si | PMMA | PS | -1.95E-19 | 0.1 | 6.83E-20 | 0.34 | 6.774E-19 | -0.06 |
| SiO | Toluene | PS | 1.74E-21 | 7.1 | 6.98E-20 | 0.31 | 5.34E-22 | 1.34 |
| Si | Toluene | PS | -1.97E-19 | 0.1 | 6.98E-20 | 0.31 | 6.75E-19 | -0.06 |
| SiO | Toluene | Acetone | 2.06E-21 | -9.0 | 6.98E-20 | 0.31 | 5.34E-22 | -6.25 |
| Si | Toluene | Acetone | -1.97E-19 | -0.2 | 6.98E-20 | -0.45 | 6.75E-19 | 0.09 |
| SiO | PMMA | PSAN | 8.44E-22 | 13.9 | 6.83E-20 | 0.32 | 3.12E-22 | -1.71 |
| Si | PMMA | PSAN | -1.95E-19 | 0.1 | 6.83E-20 | 0.32 | 6.77E-19 | -0.06 |

TABLE 4.2: The 3-component Hamaker constants $A_{\mathrm{smg}}$, $A_{\mathrm{mgm}}$ and $A_{\mathrm{sms}}$ for various mixtures, approximated as linear functions of the solute concentration $\phi_0$. For definitions of $\delta$ and $M_1$ see Eq. (4.5)

## 4.3 Thin film evolution equations for mixtures

The main focus of our work on mixtures is to investigate the effects that result from a contribution in the free energy functional $F$, discussed in Section 2.3.2, that accounts for the dependence of the wettability of liquid mixtures, suspensions or polymer solutions, on the concentration of the solute. Typically, when employing thin film theory to describe films or droplets of solutions, approaches in the literature [36, 53, 54, 97] assume that the wetting energy of the system does not depend on the concentration, which may not always be a reasonable approximation. For example, in the case of evaporating solutions, in the contact line region the concentration of solute locally becomes relatively large and the assumption that the wetting energy does not depend on it will normally not hold.

In the general case, $F$ is the free energy functional

$$F[h,\psi] = \int \left[ e(h,\psi) + \frac{\gamma}{2}(\nabla h)^2 + \frac{\sigma}{2} h \left( \nabla \left( \frac{\psi}{h} \right) \right)^2 \right] \mathrm{d}s. \tag{4.6}$$

The first term in the integral represents the contribution from the local free energy, while the second and the third one stand for the surface and interfacial contributions, respectively. Here $\gamma$ is the mixture-air surface tension, $\sigma$ is (related to) the interfacial stiffness of the solute - solvent interface in case of decomposition. The concentration-dependent local free energy is

$$e(h,\psi) = f(h,\psi) + hg\left(\frac{\psi}{h}\right). \tag{4.7}$$

In our case, the concentration - dependent adhesion (or wetting) energy $f(h,\psi)$ is

$$f(h,\psi) = -\frac{A\left(\frac{\psi}{h}\right)}{2h^2} + \frac{B}{5h^5} \tag{4.8}$$

and we approximate the Hamaker coefficient $A\left(\frac{\psi}{h}\right)$ as a linear function of the solute concentration

$$A\left(\frac{\psi}{h}\right) = |A_0|\left(\delta + M_1 \frac{\psi}{h}\right). \tag{4.9}$$

Here we assume that $B$ is a constant – it does not depend on the solute concentration. This implies that there exists a precursor film of a thickness, which depends on the concentration, $h_p = \left(\frac{B}{A(\phi)}\right)^{1/3}$ (again assuming the film always remains homogeneous). Note that we combine a concentration-dependent Hamaker constant $A(\phi)$ and a constant $B$ in the short-range contribution. One may as well introduce a concentration dependent short-range contribution[1] or use a different form for the short-range contribution; however, these choices do not affect the main results. The system behavior is very similar if wetting energies of a similar form are chosen that result in identical precursor film heights and equilibrium contact angles.

[1]Note that this is just one of a few options for $B$. Other options include (i) fixing $h_p$ to keep the value it has at $\phi = 0$ and calculating $B$ as a function of $h_p$ and $\phi$ or (ii) assuming a certain dependence of $B$ on $\phi$, e.g. $B = B_0 \mathrm{e}^{\alpha\phi}$ with $\alpha \gg 1$.

The disjoining pressure is related to the local free energy by $\Pi = -\partial_h f(h,\psi)$. The related chemical potential is $\Omega = -\partial_\psi f$.

The function $g\left(\frac{\psi}{h}\right)$ is the bulk part of the free energy (4.6) and accounts in the simplest case only for entropic contributions to the local free energy, i.e., one assumes the solute molecules/particles do not show any net attractive interaction between them[2]:

$$g\left(\frac{\psi}{h}\right) = \frac{k_b T}{a^3}\frac{\psi}{h}\ln\frac{\psi}{h}. \tag{4.10}$$

Here $a$ is a molecular length scale related to the solute, $k_b$ is the Boltzmann constant and $T$ is the absolute temperature.

Note that in the limit of a constant film thickness, Eq. (2.53) with $F$ given by (4.6) and $\sigma = 0$ becomes the standard Fickian diffusion equation for $\phi$.

The resulting variations of the free energy (4.6) with respect to the conserved fields $h$ and $\psi$ are

$$\frac{\delta F}{\delta h} = \partial_h e - \frac{2\sigma\psi}{h^3}\nabla h\nabla\psi + \frac{3\sigma\psi^2}{2h^4}(\nabla h)^2 + \frac{\sigma}{2h^2}(\nabla\psi)^2 - \left(\frac{\sigma\psi^2}{h^3} + \gamma\right)\Delta h + \frac{\sigma\psi}{h^2}\Delta\psi, \tag{4.11}$$

$$\frac{\delta F}{\delta \psi} = \partial_\psi e - \frac{\sigma\psi}{h^3}(\nabla h)^2 + \frac{\sigma}{h^2}\nabla h\nabla\psi + \frac{\sigma\psi}{h^2}\Delta h - \frac{\sigma}{h}\Delta\psi. \tag{4.12}$$

The Euler - Lagrange equations that describe film thickness and concentration profiles of extremal energy, i.e. steady states of the system, are

$$\frac{\delta F}{\delta h} - \mu_h = 0; \tag{4.13}$$

$$\frac{\delta F}{\delta \psi} - \mu_\psi = 0, \tag{4.14}$$

where in the considered non-volatile case $\mu_h$ and $\mu_\psi$ are the Lagrange multipliers accounting for mass conservation of the mixture and solute, respectively. For

[2]One can consider different extensions for g: (i) in the case of weakly interacting colloidal particles, i.e. no solute-solvent decomposition, one can choose $g \sim \phi\log\phi - b\phi^2$; (ii) in the case of strongly interacting colloidal particles one can recover the long–wave limit of model-H [112] with $g \sim \kappa(\nabla\phi)^2 + (\phi^2-1)^2$.

homogeneous flat films they may be obtained from equations (4.11) and (4.12) in terms of the mean film thickness $h_0$ and mean local amount of solute $\psi_0$:

$$\begin{aligned}\mu_h &= (\partial_h f + g + h\partial_h g)|_{h_0,\psi_0} = \frac{A_0}{h_0^3} - \frac{B}{h_0^6} - \frac{k_b T}{a^3}\frac{\psi_0}{h_0} + |A_0|M_1\frac{3\psi_0}{2h_0^4};\\ \mu_\psi &= (\partial_\psi f + h\partial_\psi g)|_{h_0,\psi_0} = -\frac{|A_0|M_1}{2h_0^3} + \frac{k_b T}{a^3}\left(\ln\frac{\psi_0}{h_0} + 1\right).\end{aligned} \tag{4.15}$$

It is also interesting to observe how the convective and diffusive fluxes introduced in Section 2.3.2 look like when one includes the explicit dependence on the solute concentration in the pressure term.

If one substitutes $\phi$ for $\psi/h$ in Eqs. (2.43) and (2.44), the convective and diffusive fluxes take the form

$$\begin{aligned}J_{\text{conv}} &= \frac{h^3}{3\eta}\left\{\gamma\nabla\Delta h - \nabla\partial_h f + \frac{\partial_\phi f}{h}\nabla\phi - \frac{\sigma}{h}\left[\nabla\cdot(h\nabla\phi)\nabla\phi - \frac{\sigma}{2}\nabla|\nabla\phi|^2\right]\right\}\\ J_{\text{diff}} &= -\frac{\widetilde{D}h\phi}{\eta}\nabla\left[\frac{\partial_\phi f}{h} + \partial_\phi g - \frac{\sigma}{h}\nabla\cdot(h\nabla\phi)\right]\end{aligned} \tag{4.16}$$

respectively [171].

In the convective flux [Eq. (4.16)] the first term is due to Laplace pressure gradients ($\gamma(\phi)$ is often replaced by a constant reference value $\gamma_0$ [114]); the second term is the Derjaguin pressure contribution due to wettability; and the final two terms represent the Korteweg flux, i.e., a bulk concentration-gradient-driven flux (cf. Ref. [8] for a discussion of the related bulk model H). The third term is a flux driven by concentration gradients within the bulk of the film but only if the film is sufficiently thin such that its two interfaces feel each other. This novel flux is a direct consequence of the concentration dependence of the wetting energy and has a similar magnitude as the Derjaguin pressure contribution. The first term of the diffusive flux [Eq. (4.16)] is also not common in the literature although it is a natural consequence of the gradient dynamics form. It represents the influence of the concentration-dependent wettability on diffusion. The second term is the flux due to gradients of the chemical potential $\mu = \partial_\phi g$ in the bulk of the film

while the final term is a Korteweg contribution to diffusion that counters steep concentration gradients, e.g., for decomposing solvent-solute films.

In this section we introduced the general set of coupled evolution equations for the film thickness (2.52) and local amount of solute (2.53) in a variational form and proposed a particular example for the free energy functional (4.6). In the next step we non-dimensionalise the governing equations, thus reducing the number of parameters in them.

## 4.4 Non–dimensional form of the equations

In this section we introduce suitable scales for time, space and energy. Substituting the proposed set of scaled variables in the expression for the free energy functional (4.6) and in its variations with respect to $h$ and $\psi$ allows us to arrive at a non-dimensional formulation for the evolution equations (2.52) and (2.53).

The set of scaling parameters is

| | | | | | | |
|---|---|---|---|---|---|---|
| Dimensionless | $\tilde{t}$ | $\tilde{x}$ | $\tilde{y}$ | $\tilde{h}$ | $\tilde{\psi}$ | $\tilde{e}$ |
| Scale | $T$ | $L$ | $L$ | $l$ | $l$ | $\kappa$ |
| Dimensional | $t = \tau\tilde{t}$ | $x = L\tilde{x}$ | $y = L\tilde{y}$ | $h = l\tilde{h}$ | $\psi = l\tilde{\psi}$ | $e = \kappa\tilde{e}$ |

Note that $x$ and $y$ scale differently from $z$, naturally allowing for a long-wave approach. Using the proposed scales we obtain for the area element, nabla operator and mobility coefficients

$$\mathrm{d}s = L^2\mathrm{d}\tilde{s}, \quad \nabla = \frac{1}{L}\widetilde{\nabla}, \quad Q_{ij} = \frac{l^3}{\eta}\tilde{Q}_{ij}, \tag{4.17}$$

respectively. Applying the scaling, we obtain the dimensionless local free energy

$$\tilde{e} = \frac{1}{\kappa}\left[-\frac{\delta|A_0|}{2\tilde{h}^2 l^2} - \frac{|A_0|M_1\tilde{\psi}}{2\tilde{h}^3 l^2} + \frac{B}{5\tilde{h}^5 l^5} + \frac{k_b T l\tilde{\psi}}{a^3}\ln\left(\frac{\tilde{\psi}}{\tilde{h}}\right)\right]. \tag{4.18}$$

For the dimensionless gradient terms in the free energy functional (4.6) we obtain

$$\frac{1}{\kappa}\left[\frac{\gamma}{2}(\nabla h)^2 + \frac{\sigma}{2}h\left(\nabla\left(\frac{\psi}{h}\right)\right)^2\right] = \frac{1}{\kappa}\left[\frac{\gamma l^2}{2L^2}(\widetilde{\nabla}\tilde{h})^2 + \frac{\sigma l\tilde{h}}{2L^2}\left(\widetilde{\nabla}\frac{\tilde{\psi}}{\tilde{h}}\right)^2\right]. \tag{4.19}$$

If one choses the energy (per area) density scale $\kappa = \frac{|A_0|}{l^2}$, the dimensionless free energy functional becomes

$$\widetilde{F}[\tilde{h},\tilde{\psi}] = \int\left[-\frac{\delta}{2\tilde{h}^2} - \frac{M_1\tilde{\psi}}{2\tilde{h}^3} + \frac{\widetilde{B}}{5\tilde{h}^5} + M_2\tilde{\psi}\ln\left(\frac{\tilde{\psi}}{\tilde{h}}\right) + \frac{\tilde{\gamma}}{2}(\widetilde{\nabla}\tilde{h})^2 + \frac{\tilde{\sigma}}{2}\tilde{h}\left(\widetilde{\nabla}\frac{\tilde{\psi}}{\tilde{h}}\right)^2\right]\mathrm{d}\tilde{s}, \tag{4.20}$$

where we used $\widetilde{F} = \frac{F}{\kappa L^2}$. The introduced dimensionless parameters are

$$\widetilde{B} = \frac{B}{|A_0|l^3}; \tag{4.21}$$

$$M_2 = \frac{l^3 k_b T}{|A_0|a^3}; \tag{4.22}$$

$$\widetilde{\gamma} = \frac{l^4\gamma}{L^2|A_0|}; \tag{4.23}$$

$$\widetilde{\sigma} = \frac{l^3\sigma}{|A_0|L^2}. \tag{4.24}$$

Using the new scales one finds for the dimensionless variations of the free energy functional

$$\frac{\delta\widetilde{F}}{\delta\tilde{h}} = \frac{l^3}{\kappa L^2}\frac{\delta F}{\delta h}; \tag{4.25}$$

$$\frac{\delta\widetilde{F}}{\delta\tilde{\psi}} = \frac{l^3}{\kappa L^2}\frac{\delta F}{\delta\psi}. \tag{4.26}$$

The nondimensional form of the evolution equations (2.39) and (2.40) is

$$\partial_{\tilde{t}}\tilde{h} = \widetilde{\nabla}\cdot\left[\widetilde{Q}_{\tilde{h}\tilde{h}}\widetilde{\nabla}\frac{\delta\widetilde{F}}{\delta\tilde{h}} + \widetilde{Q}_{\tilde{h}\tilde{\psi}}\widetilde{\nabla}\frac{\delta\widetilde{F}}{\delta\tilde{\psi}}\right]; \tag{4.27}$$

$$\partial_{\tilde{t}}\tilde{\psi} = \widetilde{\nabla}\cdot\left[\widetilde{Q}_{\tilde{h}\tilde{\psi}}\widetilde{\nabla}\frac{\delta\widetilde{F}}{\delta\tilde{h}} + \widetilde{Q}_{\tilde{\psi}\tilde{\psi}}\widetilde{\nabla}\frac{\delta\widetilde{F}}{\delta\tilde{\psi}}\right], \tag{4.28}$$

where we have fixed the timescale as $\tau = \frac{l\eta}{\kappa}$.

From now on we will only refer to the non-dimensional equations and will, for convenience, omit the tilde symbols from the non-dimensional variables and parameters.

## 4.5 Linear stability of the flat film

We start the analysis of our 2-field model for a mixture with concentration dependent wettability by discussing the linear stability of flat homogeneous films. Equations (4.27) and (4.28) are linearised in $\epsilon$ for small amplitude disturbances described by the ansatz

$$\begin{aligned} h(x,t) &= h_0 + \epsilon e^{ikx+\beta t}; \\ \psi(x,t) &= \psi_0 + \epsilon\chi e^{ikx+\beta t}, \end{aligned} \tag{4.29}$$

where $k$, $\beta$ and $\epsilon\boldsymbol{\chi} = \epsilon(1,\chi)$ are the wave number, growth rate and amplitude vector of the disturbance. Here, $\epsilon \ll 1$ is the small amplitude of the perturbation of the film height and $\chi$ is the ratio of the amplitudes of the perturbations of the solute layer thickness and the film thickness. The sign of $\chi$ determines whether the modulations of the concentration field and the film thickness are in-phase (positive) or anti-phase (negative). The magnitude of $\chi$ indicates whether the instability is driven by the film thickness field ($|\chi| \ll 1$), by the solute layer thickness field ($|\chi| \gg 1$) or by the coupling of the two fields ($|\chi| \approx 1$).

One obtains for the linearised functional derivatives (4.25) and (4.26)

$$\begin{aligned}\frac{\delta F}{\delta h} &= \epsilon\left(\partial_{hh}e^0+\partial_{h\psi}e^0\chi+\gamma k^2-\sigma k^2\frac{\psi_0}{h_0^2}\chi+\sigma k^2\frac{\psi_0^2}{h_0^3}\right)\mathrm{e}^{ikx+\beta t}+\mu_h+O(\epsilon^2);\\ \frac{\delta F}{\delta \psi} &= \epsilon\left(\partial_{\psi h}e^0+\partial_{\psi\psi}e^0\chi-\sigma k^2\frac{\psi_0}{h_0^2}+\frac{\sigma k^2}{h_0}\chi\right)\mathrm{e}^{ikx+\beta t}+\mu_\psi+O(\epsilon^2),\end{aligned} \tag{4.30}$$

where $e^0=e(h_0,\psi_0)$.

This can be written in matrix form using the symmetric energy matrix $\mathcal{E}$ that corresponds to the matrix of the second variations of $F[h,\psi]$ in Fourier space [124]:

$$\begin{pmatrix}\frac{\delta F}{\delta h}\\ \frac{\delta F}{\delta \psi}\end{pmatrix}=\begin{pmatrix}\mu_h\\ \mu_\psi\end{pmatrix}+\epsilon\mathrm{e}^{ikx+\beta t}\begin{pmatrix}\mathcal{E}_{11}&\mathcal{E}_{12}\\ \mathcal{E}_{21}&\mathcal{E}_{22}\end{pmatrix}\begin{pmatrix}1\\ \chi\end{pmatrix}+O(\epsilon^2), \tag{4.31}$$

where

$$\mathcal{E}=\begin{pmatrix}\partial_{hh}e^0+\gamma k^2+\sigma k^2\frac{\psi_0^2}{h_0^3} & \partial_{h\psi}e^0-\sigma k^2\frac{\psi_0}{h_0^2}\\ \partial_{\psi h}e^0-\sigma k^2\frac{\psi_0}{h_0^2} & \partial_{\psi\psi}e^0+\frac{\sigma k^2}{h_0}\end{pmatrix}. \tag{4.32}$$

The dispersion relation $\beta(k)$ is obtained by solving the eigenvalue problem resulting from (4.27) and (4.28)

$$(-k^2\mathcal{Q}\cdot\mathcal{E}-\beta\mathcal{I})\boldsymbol{\chi}=0, \tag{4.33}$$

where $\mathcal{Q}$ is the scaled symmetric mobility matrix taken at $(h_0,\psi_0)$, $\mathcal{Q}\cdot\mathcal{E}$ is the corresponding non-symmetric Jacobi matrix and $\mathcal{I}$ is a $2\times 2$ identity matrix.

The condition $\det(-k^2\mathcal{Q}\cdot\mathcal{E}-\beta\mathcal{I})=0$ yields the dispersion relations

$$\beta_{1,2}=\frac{\mathrm{tr}(-k^2\mathcal{Q}\cdot\mathcal{E})}{2}\pm\sqrt{\left(\frac{\mathrm{tr}(-k^2\mathcal{Q}\cdot\mathcal{E})}{2}\right)^2-\det(-k^2\mathcal{Q}\cdot\mathcal{E})}, \tag{4.34}$$

where

$$\mathrm{tr}(-k^2\mathcal{Q}\cdot\mathcal{E}) = -k^2(2\mathcal{Q}_{12}\mathcal{E}_{12}+\mathcal{Q}_{11}\mathcal{E}_{11}+\mathcal{Q}_{22}\mathcal{E}_{22}), \tag{4.35}$$

$$\det(-k^2\mathcal{Q}\cdot\mathcal{E}) = k^4\det\mathcal{Q}\det\mathcal{E} \tag{4.36}$$

and we have used the symmetries of the matrices $\mathcal{Q}$ and $\mathcal{E}$. As $Q$ is symmetric and positive definite, the onset of the instability is at $\det\mathcal{E}=0$ and this condition leads to a biquadratic equation for the critical wave number

$$\alpha_1 k_c^4+\alpha_2 k_c^2+\alpha_3=0, \tag{4.37}$$

with coefficients

$$\alpha_1 = \frac{\gamma\sigma}{h_0}; \tag{4.38}$$

$$\alpha_2 = \frac{\sigma}{h_0}\partial_{hh}e^0+\left(\gamma+\frac{\sigma\psi_0^2}{h_0^3}\right)\partial_{\psi\psi}e^0+2\frac{\sigma\psi_0}{h_0^2}\partial_{\psi h}e^0; \tag{4.39}$$

$$\alpha_3 = \partial_{hh}e^0\partial_{\psi\psi}e^0-(\partial_{\psi h}e^0)^2. \tag{4.40}$$

As the surface and interfacial tension terms in $\mathcal{E}$ are always positive and $\mathcal{E}$ is symmetric, the stability borders are determined by the condition $\alpha_3=0$ and the instability is always long–wave, i.e. at onset always $k=0$.

Typical dispersion relations are shown on Fig. 4.8. If all the roots of Eq. (4.37) are complex, $\beta(k)$ does not cross the $k$-axis and this situation corresponds to a linearly stable film. For unstable films there exists a region of unstable modes with wave numbers $0<k<k_c$, where $k_c$ is the wave number at $\beta(k_c)=0$, known as the critical wave number. The corresponding critical wavelength of the perturbation is $L_c=2\pi/k_c$. The harmonic film thickness and solute layer thickness profiles of vanishing amplitude at $k=k_c$ are neutrally stable and small amplitude harmonic periodic steady solutions of Eqs. (4.27) and (4.28) are found at $k\approx k_c$. The maximum of the dispersion relation occurs at the most unstable wavelength - it corresponds to the fastest growing unstable mode. In the decoupled case it

is at $k' = k_c/\sqrt{2}$. It defines a typical lateral length scale $L' = 2\pi/k'$ known as the *spinodal wavelength*. It corresponds to the characteristic length scale of the domains formed by thiner films which undergo spinodal dewetting, i.e. their breakup occurring through the growth of uniformly distributed surface undulations [134].

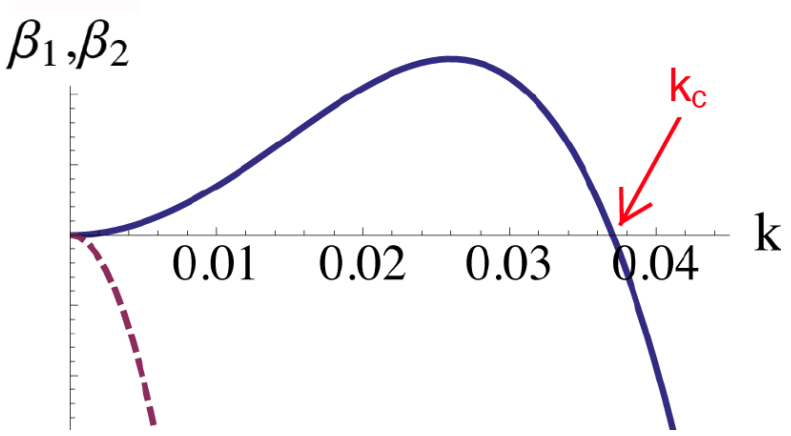


FIGURE 4.8: Dispersion relations for a flat film of mixture on a horizontal homogeneous substrate. The dotted and solid lines represent the linearly stable and unstable cases, respectively.

Employing linear stability analysis, we can obtain the stability thresholds in the space spanned by the non-dimensional parameters in the non-dimensional free energy functional (4.20), and the mean film thickness and mean solute concentration. The resulting stability diagrams will be presented and analysed in Section 4.7. They will allow us to study how the effects of coupling of the two fields influence the stability of the system. The gained information also helps to calculate and analyse non-trivial steady states and the time evolution of a flat film. The linear and non–linear behaviour will be discussed together in Sections 4.7.1 and 4.7.2 for the cases when the pure solvent is stable ($\delta = -1$) or unstable ($\delta = 1$), respectively.

Another important issue in any multicomponent system is the presence of coexisting phases or states. In our isothermal model, where the concentration of the solute is vertically averaged and both fields are conserved, we would expect to observe coexisting film and solute layer thicknesses that e.g. characterise the state

which a time evolution will converge to in the long–time (thermodynamic) limit. They can be predicted using thermodynamic and geometric considerations and will be discussed in the following Section 4.6.

## 4.6 Binodal lines

In thermodynamics, the condition at which two distinct phases may coexist is characterised by the so called coexistence curve or *binodal* curve. The local free energy is usually approximated by a double-well potential which means there exists a critical point and if we consider a flat homogeneous film in the vicinity of this point, its stability and phase behaviour can be sketched on a diagram, like the one shown in Fig. 4.9. The $y$-axis corresponds to the relevant control parameter (typically temperature) and $x$-axis is corresponding to the order parameter of the problem. The dashed red line represents the *spinodal* curve, that is the border below which the film is unstable. The solid black line, which is the binodal line, marks the boundary above which the film is absolutely stable. In the region between the two lines the system is *metastable*. The latter means that the system can rupture when a certain threshold (critical nucleation solution) is overcome.

For the case of a simple liquid, the binodal curve is typically calculated by equating the chemical potentials, the temperature and pressure for each of the coexisting phases. The spinodal curve is defined as the border where the curvature of the free energy is zero.

In the case of a mixture, however, the calculation of the binodal and spinodal lines is more challenging, due to the large number of parameters in the model. To calculate the binodals for the case of a non-volatile film of a two-component mixture on a solid substrate, we assume to have two coexisting states at thermodynamic equilibrium. Therefore, there are four conditions which need to be satisfied.

From a thermodynamic point of view, a given system is fully described if the appropriate thermodynamical potential can be calculated. For an isothermal system

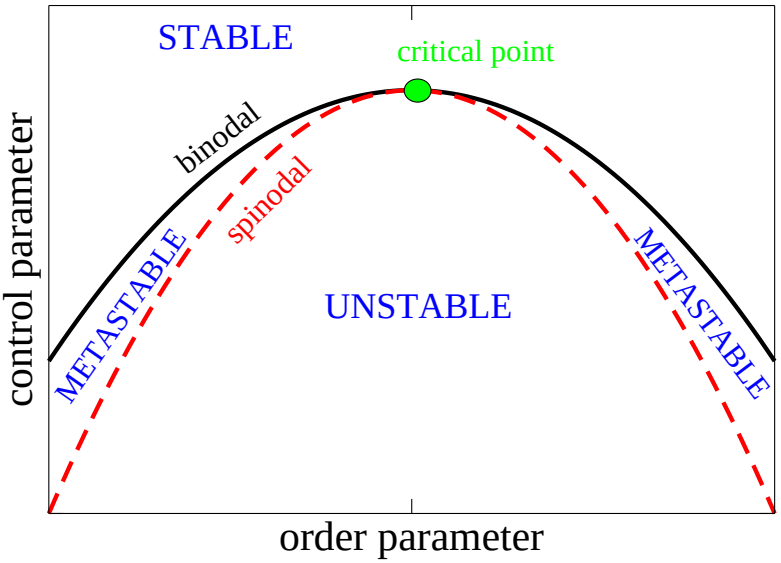


FIGURE 4.9: Schematic equilibrium coexistence or binodal curve (solid black line) and spinodal curve (dashed red line). The $x$- and $y$-axis correspond to the relevant order parameter of the problem and the control parameter, respectively. The critical point, stable, unstable and metastable regions are marked accordingly.

in thermodynamic equilibrium with free energy $e$, the thermodynamic function we use to describe the considered system with mixture is the grand potential $\omega$, defined as $\omega = e - \mu\chi$ where $\mu$ is the relative chemical potential and $\chi$ is the relevant composition variable.

For a two-component mixture in thermodynamic equilibrium, the grand potentials, characterising the two coexisting phases of the isothermal system need to be the equal. Further, the chemical potentials of the mixture and the solute should be equal, which amounts to three conditions for the four unknowns. In order to obtain the necessary fourth condition, we assume that the two coexisting states are two flat films of different thicknesses $h_1$ and $h_2$, and concentrations $\phi_1$ and $\phi_2$, as sketched in Fig. 4.10. For any given $x = x_i$ the relation $\psi_i = h_i\phi_i$ is fulfilled. In other words, one requests that the borders between the two states in $h$ and in $\phi$ coincide.

The grand potential of a given phase is

$$\omega = e - \mu_h h - \mu_\psi \psi, \tag{4.41}$$

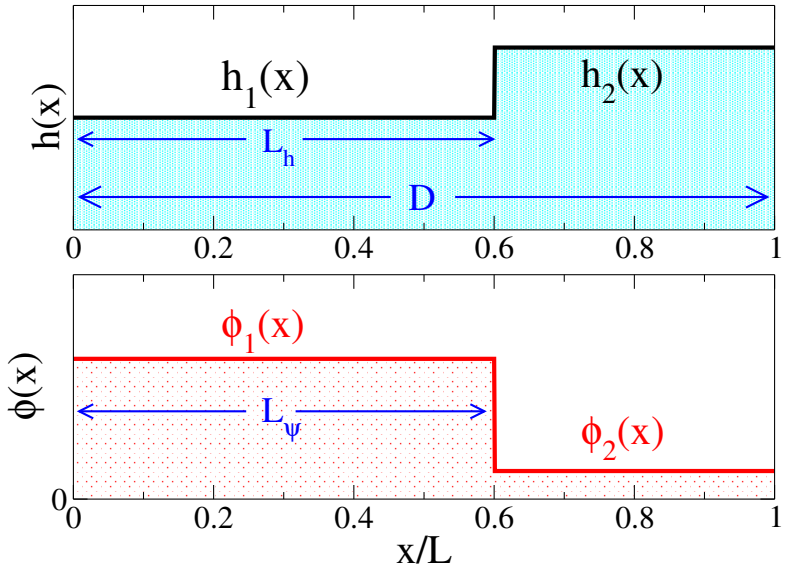


FIGURE 4.10: Coexisting flat states: film heights and concentrations

where the chemical potentials are

$$\mu_h = \frac{\partial e}{\partial h}, \tag{4.42}$$

$$\mu_\psi = \frac{\partial e}{\partial \psi}. \tag{4.43}$$

If we consider the geometry sketched in Fig. 4.10, we see that if the mean film thickness $h_0$ changes, the characteristic length $L_h$ needs to adjust accordingly and the mean solute thickness $\psi_0$ has to change in such a way that $L_\psi$ remains equal to $L_h$. This construction holds even in the thermodynamic limit ($D \to \infty$) as well as in a 2-dimensional situation where areas $A_h$ and $A_\psi$ would take the role of $L_h$ and $L_\psi$, respectively.

If one chooses $L_\psi = L_h = L$ and denotes the domain size by $D$, one obtains the relations

$$(D - L)h_2 + Lh_1 = Dh_0, \tag{4.44}$$

$$(D - L)\psi_2 + L\psi_1 = D\psi_0. \tag{4.45}$$

Eliminating $\tilde{L} = \frac{L}{D}$, one arrives at the fourth condition, needed for the calculation of the binodal thicknesses. It has to hold for any $D$, even in the thermodynamic

limit $D, L \to \infty$. Then the system for the 4 unknowns is completely determined:

$$\omega(h_1, \psi_1) = \omega(h_2, \psi_2); \tag{4.46}$$

$$\mu_h(h_1, \psi_1) = \mu_h(h_2, \psi_2); \tag{4.47}$$

$$\mu_\psi(h_1, \psi_1) = \mu_\psi(h_2, \psi_2); \tag{4.48}$$

$$\frac{h_0 - h_2}{h_1 - h_2} = \frac{\psi_0 - \psi_2}{\psi_1 - \psi_2}. \tag{4.49}$$

This system of equations is employed to determine the binodals presented below in Sections 4.7.1.2 and 4.7.2.2 for the cases when a solute is added to an stable or unstable solvent, respectively.

## 4.7 Results

The wetting energy (4.8) contains a concentration-dependent long-range part, in which the dependency on concentration is incorporated via the Hamaker constant $A(\phi) = |A_0|(\delta + M_1\phi)$ with $\delta = \pm 1$. For a chosen combination of materials, i.e. fixed $A_0$ and $M_1$, the value of $A(\phi)$ depends on the solute concentration and can either be positive or negative. For the sign convention chosen in Eqs. (4.6) and (4.8) positive [negative] Hamaker constants correspond to destabilising [stabilising] long-range interactions. This means that $\delta = -1$ characterises a linearly stable film of pure solvent, while $\delta = 1$ implies a film of pure solvent that is linearly unstable above $h_c = (2B)^{1/3}$. Adding a solute, characterised by $M_1 < 0$ [$M_1 > 0$] into the system, we add a material that on its own would form a stable [unstable] film on the given substrate. A major question is whether adding solute to a film of pure solvent results in a stabilisation [destabilisation] of the mixture film.

The short-range part in Eq. (4.8) is always stabilising ($B > 0$). The other free parameters that we can use to control the properties of the system (see Eqs. (4.15)), are the constant in the entropic term $M_2$, the mean film thickness $h_0$ and the mean local amount of solute $\psi_0$ (or the mean solute concentration $\phi_0 = \psi_0/h_0$).

| substrate | mixture | | $A=\|A_0\|\ (\delta+M_1\phi)$ | | |
|---|---|---|---|---|---|
| | solvent | solute | $\delta$ | $\|A_0\|$ in Nm | $M_1$ |
| SiO | PS | PMMA | 1 | 1.59E-20 | -1.07 |
| SiO | PMMA | PS | 1 | 8.44E-22 | 15.37 |
| Si | PS | PMMA | -1 | 2.22E-19 | -0.11 |
| Si | PMMA | PS | -1 | 1.95E-19 | 0.15 |
| SiO | Toluene | PS | 1 | 1.74E-21 | 7.10 |
| Si | Toluene | PS | -1 | 1.97E-19 | 0.14 |
| SiO | Toluene | Acetone | 1 | 2.06E-21 | -9.00 |
| Si | Toluene | Acetone | -1 | 1.97E-19 | -0.20 |
| SiO | PMMA | PSAN | 1 | 8.44E-22 | 13.85 |
| Si | PMMA | PSAN | -1 | 1.95E-19 | 0.13 |

TABLE 4.3: Hamaker coefficient $A$ as a linear function of the solute concentration $\phi$ for various substrate/solvent+solute/air combinations. The first three columns represent the materials in the three–component system and the last three columns give $\delta, |A_0|$ and $M_1$ characterising the Hamaker coefficient of the mixture. The shaded rows mark the cases for which a film of pure solvent is linearly stable.

From an experimental point of view, changing the value of the parameter $M_1$ corresponds to choosing a different material as a solute. For the range of materials given in Table 4.3, the values of $M_1$ lie in the range $[-10, 15]$. However, there exist material combinations, characterised by values of $M_1$ of larger magnitude.

Using Eq. (4.22) one can give a rough estimate for practically important values of the parameter $M_2$. For the range of materials listed in Table 4.3 one deduces that $|A_0|$ belongs to the range $[10^{-22}, 10^{-19}]$ Nm. At room temperature the thermal energy is $kT = 4.1 \times 10^{-21}$ Nm. Assuming the vertical length scale $l \sim 10^{-9}$ m and considering values for the molecular length scale $a$ between $10^{-10}$ m and $10^{-6}$ m, one obtains a rather broad interval of plausible values for the dimensionless parameter $M_2 \in [10^{-11}, 10^{4}]$.

In order to investigate how the linear stability reflects changes in the main parameters of the two coupled equations, we obtain the corresponding stability thresholds from (see Section 4.5)

$$\alpha_3 = \partial_{hh}e^0\partial_{\psi\psi}e^0 - (\partial_{\psi h}e^0)^2 = 0. \tag{4.50}$$

This allows us to express the critical value of each parameter as a function of the other parameters:

$$M_1^{c\pm} = -\left(\frac{2}{3}h_0^3M_2 \pm \sqrt{\frac{h_0M_2(6B - 3\delta h_0^3 + h_0^5M_2\psi_0)}{\psi_0}}\right); \tag{4.51}$$

$$\psi_0^c = \frac{(8B - 4\delta h_0^3)h_0M_2}{(3M_1 + 4h_0^3M_2)M_1}; \tag{4.52}$$

$$M_2^c = \frac{9M_1^2}{4h_0^4\left(-\frac{3M_1}{h_0} - \frac{3\delta}{\psi_0} + \frac{6B}{h_0^3\psi_0}\right)}. \tag{4.53}$$

Next, we present some particular results of the linear stability analysis for homogeneous flat films of mixture. We distinguish two main cases depending on the value of the parameter $\delta$. As we suggested earlier, this allows us to observe how the introduction of a solute influences the stability of the homogeneous flat layer.

### 4.7.1 Stable solvent

First, we focus on the case with $\delta = -1$, i.e. when a film of pure solvent is linearly stable. Adding a solute, characterised by $M_1 < 0$, results in a Hamaker constant of the mixture $A$, which remains negative at all concentrations of solute and has a larger absolute value than the one of the pure solvent. Examples are given in Table 4.3 and include PS + PMMA and toluene + acetone on Si substrates. The other possible situation is the inclusion of a solute, characterised by $M_1 > 0$, to the linearly stable film of a pure solvent. In this situation, the resulting Hamaker

constant of the mixture may switch its sign depending on the concentration. Examples for mixtures with positive $M_1$ include PMMA + PS, toluene + PS and PMMA + PSAN on Si substrate.

#### 4.7.1.1 Linear stability

In Fig. 4.11 we present a stability diagram in the plane spanned by the parameters $M_1$ and $h_0$ obtained using Eq. (4.51). The pure solvent film is stable ($\delta = -1$) and the remaining parameters are fixed as $M_2 = 0.01$ and $\phi_0 = 0.1$. The solid black curves separate the plane into three regions, as marked on the graph. As expected in this case, for $M_1 = 0$ (no solute) the system is always stable. For any fixed mean thickness $h_0$, an increase of $M_1$ from zero leads to an expected destabilisation, thus resulting in the linearly unstable region for positive $M_1$. What seems at first glance surprising is the occurrence of another unstable region for moderate $M_1 < 0$, observed for sufficiently thin films. This means that even when both, the pure solvent (characterised by $\delta = -1$) and the pure solute (characterised by $M_1 < 0$), are stable on their own, still there can exist a region in the parameter space where the mixture is linearly unstable. This observation is rather nontrivial, as it predicts a new type of thin film instability based on the coupling of height and concentration fluctuations.

For comparison, the stability borders in the $(M_1, h_0)$ plane for the case of an imposed homogeneous distribution of the solute within the film are represented in Fig. 4.11 by a dotted line. The assumption of a constant and homogeneous concentration $\phi(x,t) = \phi_0$ simplifies the analysis to the one of a single field. The local part of the free energy (4.20) is

$$e = -\frac{\delta + M_1\phi_0}{2h^2} + \frac{B}{5h^5} + M_2 h\phi_0 \ln\phi_0. \tag{4.54}$$

Now, the condition $\partial_{hh} e = 0$ alone determines the linear stability borders:

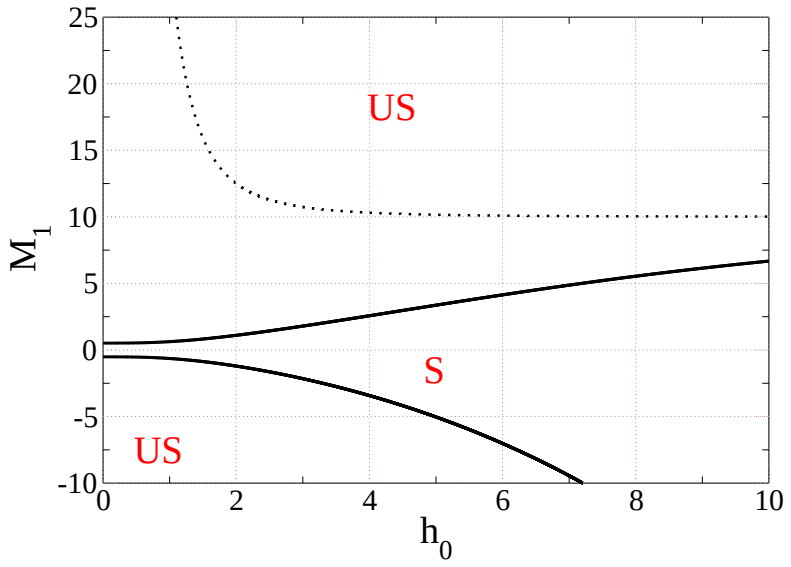


FIGURE 4.11: Stability diagram in the space spanned by $M_1$ and $h_0$ for $\delta = -1$ (stable solvent) for fixed $M_2 = 0.01$ and $\phi_0 = 0.1$. The dotted line corresponds to the case of imposed homogeneous concentration as obtained via Eq. (4.55). The stability regions are marked "S" for "linearly stable" and "US" for "linearly unstable".

$$M_1^h = \frac{1}{\phi_0}\left(\frac{2B}{h_0^3} - \delta\right). \tag{4.55}$$

Obviously, the linear stability thresholds for the situation when the concentration field and the film thickness change in a coupled way (Eq. (4.51)) look dramatically different from the case of imposed homogenous solute distribution. As visible in Fig. 4.11, for the coupled case not only there exists a linearly unstable region for $M_1 < 0$, but also the upper instability (for $M_1 > 0$) appears at much smaller, positive values of the parameter, compared to the decoupled case.

To investigate the influence of the other parameters on the stability borders in the $(M_1, h_0)$–plane, we substitute different values for $\phi_0$ and $M_2$ in Eq. (4.51). The results are shown in Figs. 4.12 and 4.13. Fig. 4.12 gives two sets of stability borders calculated for $\phi_0 = 0.1$ (solid black curves) and $\phi_0 = 0.3$ (dashed red curves), while the dotted curves represent the case of imposed homogeneous distribution of solute for the two cases. For higher mean solute concentration the stable region becomes

narrower in $M_1$ as compared to the case of smaller concentrations, as $A(\phi)$ becomes positive for smaller absolute values of $M_1$.

In Fig. 4.13 one can see the resulting stability thresholds for $M_2 = 0.01$ and $M_2 = 0.1$. The unstable region occurring at negative $M_1$ for small $h_0$, becomes more pronounced for smaller values of $M_2$. In other words, for a given $h_0$, the ratio between the molecular length scale related to the solute, $a$, and the vertical length scale related to the precursor height of the pure solvent, $l$, entering the non-dimensional parameter $M_2$, is critical for the linear stability of the system.

One may see the new instability as a higher order equivalent of Turing instability in a two-component reaction diffusion system [119]. Here the two diffusion processes that interact are the (high order) diffusion of the film height and the diffusion of the solute. However, note that the analogy is incomplete as here both fields are conserved and the instability is of infinite wavelength at onset.

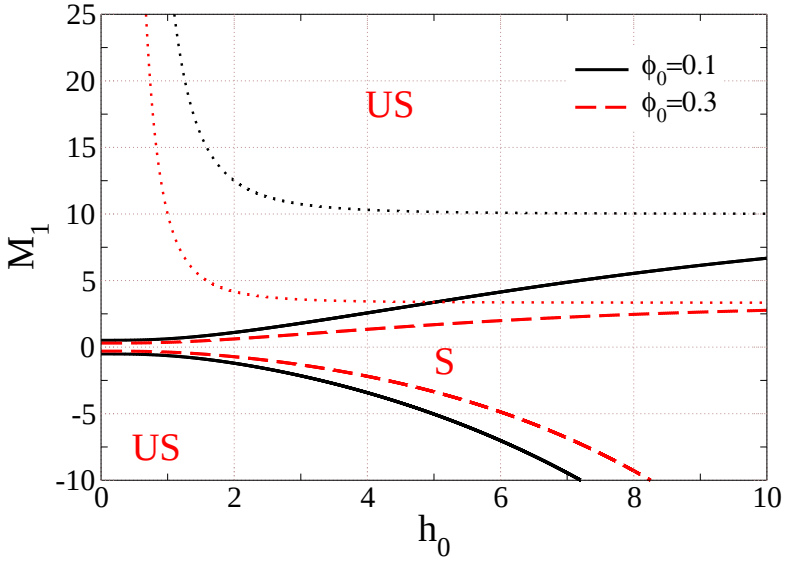


FIGURE 4.12: Stability diagrams in the space spanned by $M_1$ and $h_0$ for $\delta = -1$ (stable solvent) for fixed $M_2 = 0.01$ and $\phi_0 = 0.1$ (solid black curves) or $\phi_0 = 0.3$ (dashed red curves). The dotted black and red lines correspond to the case of imposed homogeneous concentration for the two cases. The stability regions are marked "S" for "linearly stable" and "US" for "linearly unstable".

Next, we employ Eq. (4.51) to plot the critical $M_1$ as a function of $M_2$ for fixed $h_0$ and $\phi_0$, which determines the stability borders of the system in the $(M_1, M_2)$–plane. The function has two branches, corresponding to the two conjugate roots

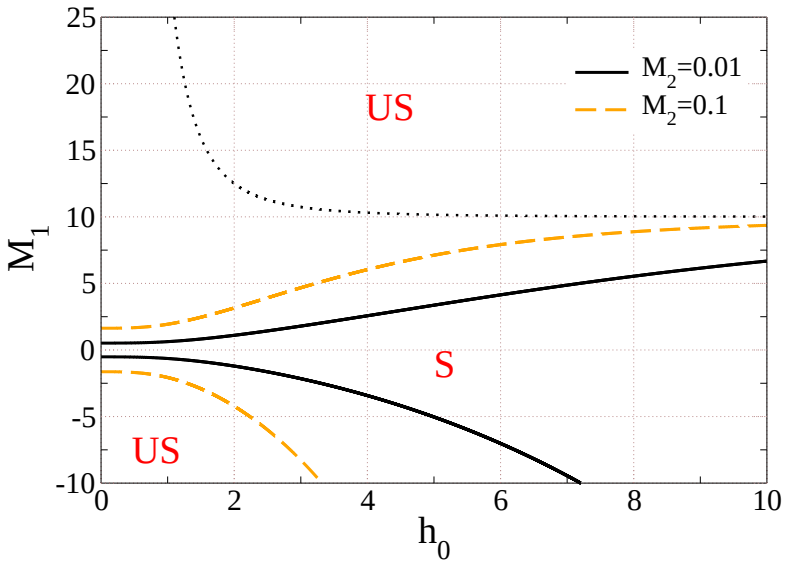


FIGURE 4.13: Stability diagrams in the space spanned by $M_1$ and $h_0$ for fixed $\delta = -1$ (stable solvent) and $\phi_0 = 0.1$. The two sets of black and orange curves correspond to the two conjugate roots for $M_1(h_0)$ for values of $M_2$ as given in legend. The stability regions are marked "S" for "stable" and "US" for "unstable". The dotted black line corresponds to the case of imposed homogeneous concentration (identical for both values of $M_2$).

of $M_1$. Fig. 4.14 shows the resulting curves for $h_0 = 5$ and $\phi_0 = 0.1$. The existence of the unstable region for negative $M_1$ is well demonstrated on this type of plot. Again, the system is always linearly stable for $M_1 = 0$, for all values of $M_2$. Then, if a destabilising solute is introduced, this results in an unstable region for $M_1 > 0$. Again, there exists another unstable region in the $M_1 < 0$ half–plane, implying that the mixing of two stable materials can result in an unstable film.

Varying $M_2$, one effectively changes the coefficient in front of the entropic term of the free energy (cf. Eq. (4.20)) that may be used to control diffusion of the solute. The destabilisation results from a decrease of the stabilising influence of the entropy, hence an analogy with homogeneous "cooling" of the system can be made (Fig. 4.14). Accordingly, moving from the unstable region towards larger $M_2$ corresponds to the opposite situation – diffusion is strengthened and the system is stabilised by entropy, related to homogeneous "heating". Reducing the parameter $M_2$ can switch the system from the stable to the unstable regime even when the total disjoining pressure term is stabilising.

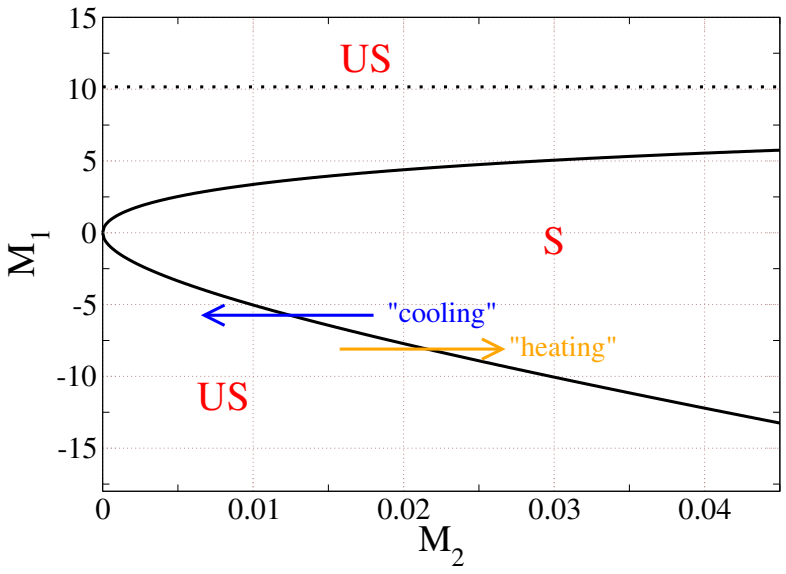


FIGURE 4.14: Stability diagram in the space spanned by $M_1$ and $M_2$. The rest of the parameters are fixed as follows: $\delta = -1$ (stable solvent), $h_0 = 5$ and $\phi_0 = 0.1$. The stability regions are marked "S" for "stable" and "US" for "unstable". The dotted black line corresponds to the case of imposed homogeneous concentration. The arrows are explained in the main text.

Moreover, for any given value of $M_2$ there exists a critical negative $M_1$, below which the system is linearly unstable. The dotted line corresponds to the case of imposed homogeneous concentration field and is included for comparison, to demonstrate the effects of the coupling.

The coordinates of the turning point of the stability border in Fig. 4.14 are $(M_1, M_2) = (0, 0)$ as calculated from Eq. (4.51) for the case of a stable pure solvent. They are $(M_1, M_2) = \left(\frac{4B-2\delta h_0^3}{h_0^2\psi_0}, \frac{-6B+3\delta h_0^3}{h_0^5\psi_0}\right)$ for the case of unstable pure solvent considered below in Section 4.7.2.

To analyse the influence of the choice of $h_0$ on the form of the stability borders in the $(M_1, M_2)$–plane, next we consider films of different thicknesses at a fixed mean solute concentration $\phi_0 = 0.1$. The resulting stability diagrams are shown in Fig. 4.15 for three values of $h_0$, where the dotted black line is the stability threshold when the concentration inside the film is assumed to remain always homogeneous. As demonstrated in the figure, if one assumes a model, in which the concentration does not change in a coupled way with the film thickness, the stability borders do practically not change when one varies $h_0$ (cf. Eq. 4.55), which

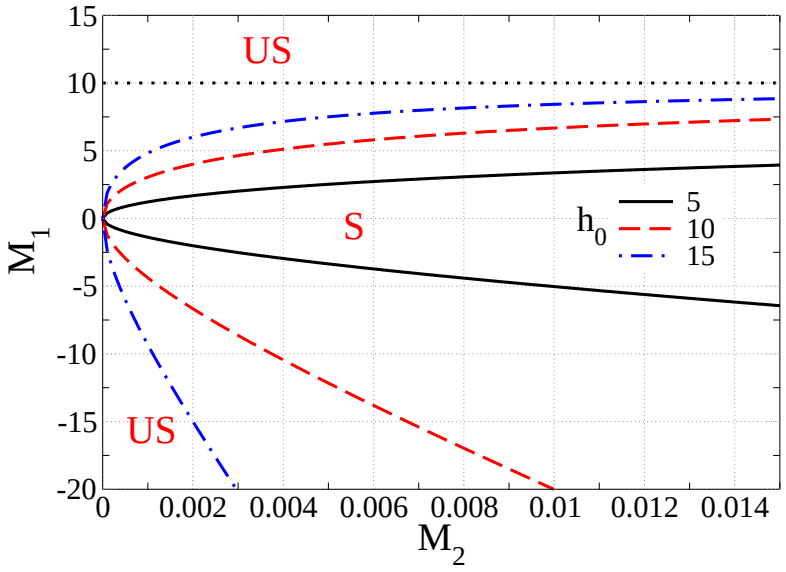


FIGURE 4.15: Stability diagrams in the space spanned by $M_1$ and $M_2$ for fixed $\delta = -1$ (stable solvent), $\phi_0 = 0.1$ and $h_0 = 5$ (solid black line), $h_0 = 10$ (dashed red line) or $h_0 = 15$ (dot-dashed blue line). The dotted black line is the stability border corresponding to the case when the concentration of solute remains homogeneous and is valid for all the cases shown in the Figure. The stability regions are marked "S" for "stable" and "US" for "unstable".

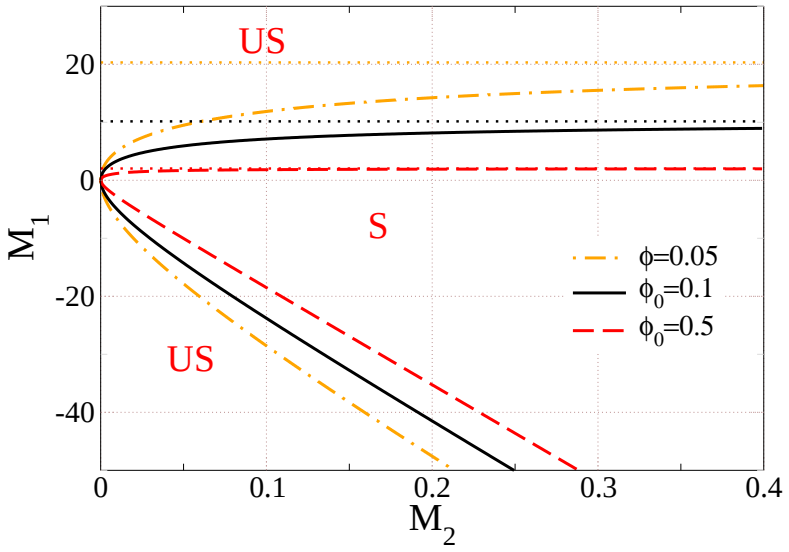


FIGURE 4.16: Stability diagrams in the space spanned by $M_1$ and $M_2$ for fixed $\delta = -1$ (stable solvent), $h_0 = 5$ and $\phi_0 = 0.05$ (dashed red line), $\phi_0 = 0.1$ (solid black line) or $\phi_0 = 0.5$ (dot-dashed orange line). The stability regions are marked "S" for "stable" and "US" for "unstable". The thin dotted lines correspond to the respective cases of imposed homogeneous concentration of solute.

is not the case for the coupled model. For any given value of $M_1 < 0$ there exists a region, where the mixture is linearly unstable. The comparison for different mean thicknesses demonstrates that a smaller $h_0$ needs a larger coefficient $M_2$ in front of the stabilising diffusion term to switch into a linearly stable state. In other words, for the same strength of the diffusion, to become unstable thicker films need more strongly destabilising solutes as compared to thinner films. This is visible in Fig. 4.15 if one considers a vertical cut $M_2 = \text{const}$.

Fig. 4.16 demonstrates the influence of the mean solute concentration on the stability behaviour in the $(M_1, M_2)$–plane. The smaller $\phi_0$ is, the wider the "stable" region is. For any given value of $M_1$ one needs to strengthen the stabilising effect of the diffusion in order to stay in the linearly stable regime when increasing the mean concentration of the solute. The dotted lines show the results in the case of imposed homogeneity.

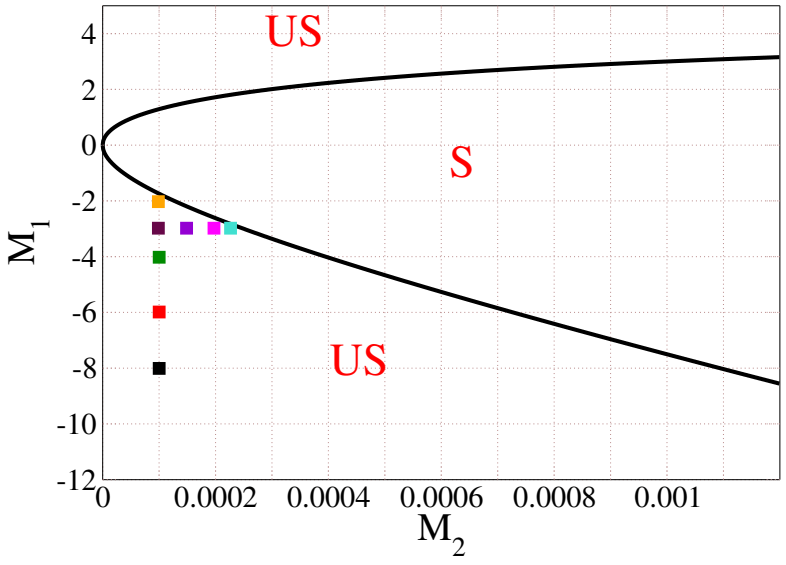


FIGURE 4.17: Stability diagram in the space spanned by $M_1$ and $M_2$ for fixed $\delta = -1$ (stable solvent), $\psi_0 = 3.0$ ($\phi_0 = 0.2$) and $h_0 = 15$. The stability regions are marked "S" for "stable" and "US" for "unstable". The coloured square symbols mark points for which we present the corresponding dispersion relations in Figs. 4.18 and 4.19, where the same colour coding is used.

#### 4.7.1.2 Non-linear steady states and time evolution

Next, we investigate steady solutions by continuing solution families through the parameter space in the case of a stable solvent, or $\delta = -1$. We fix the mean solute concentration to $\phi_0 = 0.2$ and the mean film thickness to $h_0 = 15$. The corresponding $(M_1, M_2)$–diagram is shown in Fig. 4.17.

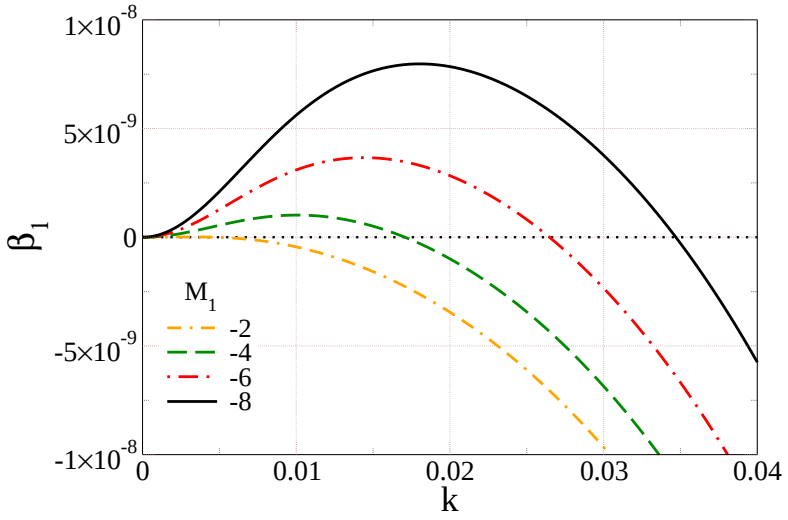


FIGURE 4.18: Dispersion relations for a flat film of mixture on a horizontal substrate. The colour code corresponds to different values of the parameter $M_1$, as given in the legend. The rest of the parameters is fixed: $\delta = -1$ (stable solvent), $\phi_0 = 0.2, h_0 = 15$ and $M_2 = 0.0001$. The colouring of the curves corresponds to the colouring of the square symbols in Fig. 4.17.

First, we calculate the dispersion relations corresponding to selected linearly unstable points from the diagram, marked by coloured square symbols in Fig. 4.17. The colour code corresponds to the one used in Figs. 4.18 and 4.19 . Their purpose is to demonstrate how the shape of the dispersion relation and the value of the critical wave number $k_c$ change when we change position in the stability diagram. On the one hand, when we increase $M_1$ at fixed $M_2$ (see Fig. 4.18), $k_c$ decreases, which means the critical domain size $L_c$ increases, until eventually $L_c$ diverges and the stability threshold is crossed. On the other hand, if $M_2$ increases for a fixed value of $M_1$ (see Fig. 4.19), then $k_c$ decreases as well - the instability onset is observed at larger domain size.

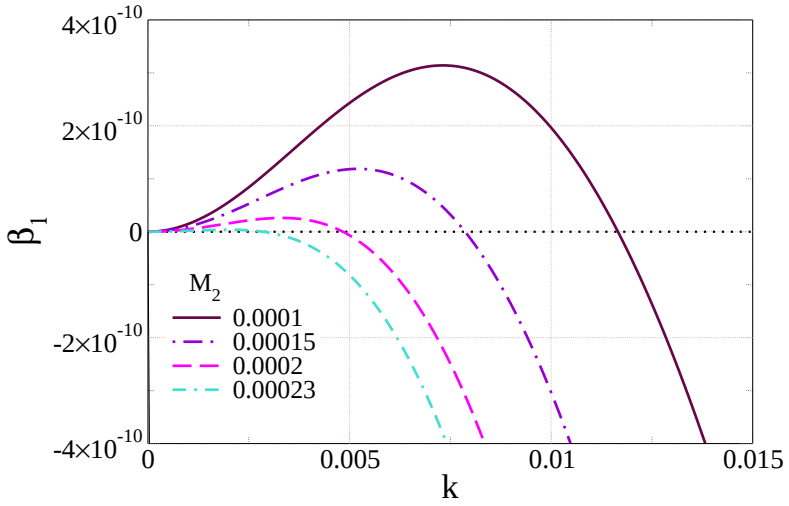


FIGURE 4.19: Dispersion relations for a flat film of mixture on a horizontal substrate for various values of the parameter $M_2$, as given in the legend. The rest of the parameters are fixed: $\delta = -1$ (stable solvent), $\phi_0 = 0.2, h_0 = 15$ and $M_1 = -3$. The colouring of the curves corresponds to the colouring of the square symbols in Fig. 4.17.

One also observes in Fig. 4.18 that the maximal growth rate $\beta_{\max}$, corresponding to the fastest growing instability mode, increases when one decreases $M_1$ and so does the corresponding wave number $k_{\max}$. On the other hand, as visible in Fig. 4.19, both $\beta_{\max}$ and $k_{\max}$ increase when $M_2$ decreases.

If we pick a particular point from the linearly unstable region of this diagram, we can observe how the parameters influence the shape of the steady film profiles, as well as the profiles of the vertically averaged concentration of the solute.

Fig. 4.20 shows a family of fully non-linear drop and hole solutions obtained for $M_1 = -8$ and $M_2 = 0.001$ when varying the domain size $L$, while Fig. 4.21 demonstrates how the steady drop and concentration profiles change along the upper branch of Fig. 4.20 when continuing towards large domain size. Starting from small-amplitude sinusoidal modulations of a flat film at a critical domain size $L_c$ determined by the linear stability analysis, these solutions are calculated using continuation techniques [45–47], as discussed in Chapter 3. Three solution measures are presented in Fig. 4.20: the "amplitude" of the film thickness profile $h_{\max} - h_{\min}$, the $L_2$-norm of the film thickness $||\delta h||$, and the 10-times magnified $L_2$-norm of the concentration field $||\delta\phi||$.

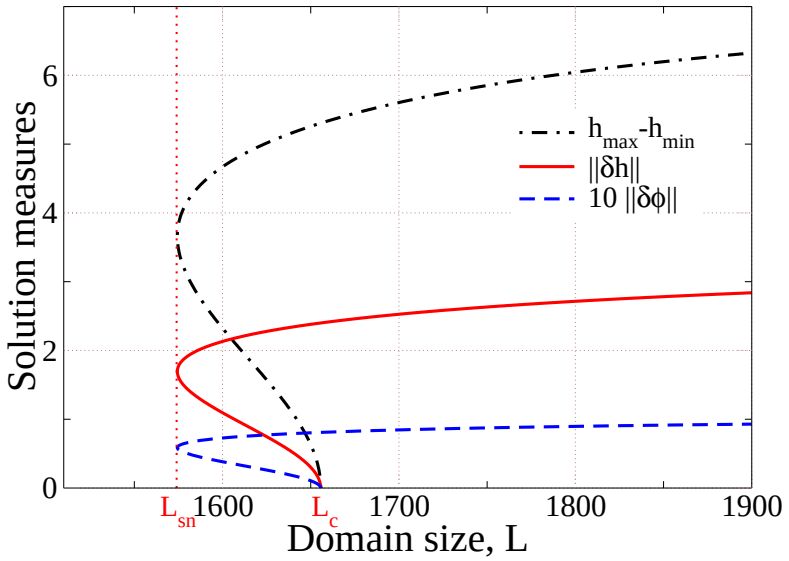


FIGURE 4.20: Solution family obtained when varying the domain size for fixed $\delta = -1$ (stable solvent), $h_0 = 15$, $\phi_0 = 0.2$, $M_2 = 0.001$ and $M_1 = -8$. The black dot-dashed curve represents the amplitude of the height profile $h_{\max} - h_{\min}$, the red solid curve is the $L_2$-norm of the film thickness $||\delta h||$, and the 10-times magnified $L_2$-norm of the concentration field $||\delta\phi||$ is given as dashed blue curve.

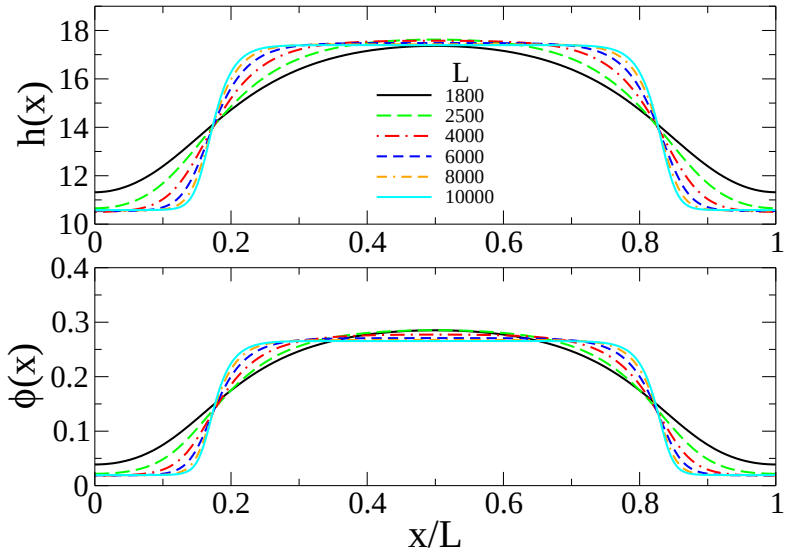


FIGURE 4.21: Film thickness and the corresponding solute concentration profiles at various domain size $L$, as given in the legend. The solutions, shown here, belong to the upper branch emerging from the saddle-node bifurcation in the bifurcation diagram in Fig. 4.20.

Only the upper branch of the diagram in Fig. 4.20 corresponds to stable stationary solutions. Their $L_2$ - norm increases monotonically with increasing the domain size. These solutions are linearly stable if one takes one period as the unit for the

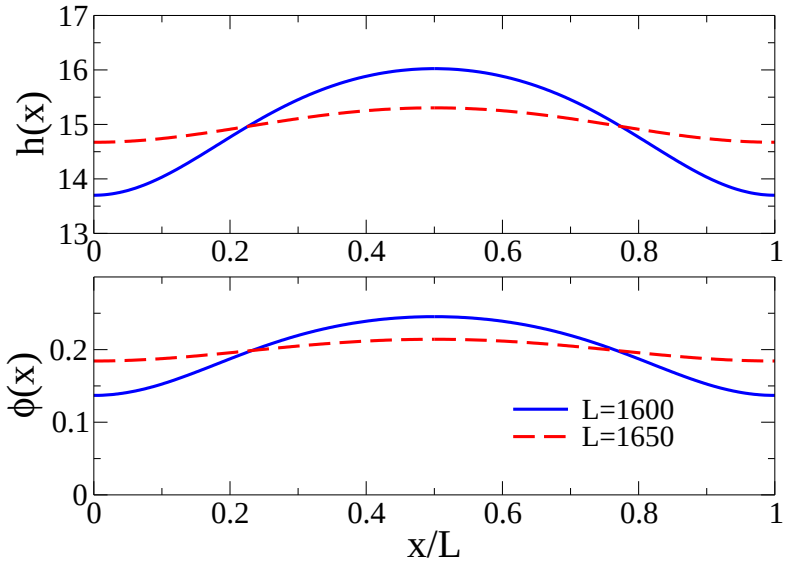


FIGURE 4.22: Film thickness and corresponding solute concentration profiles of two different domain sizes $L$, as given in the legend. The profiles, shown here, belong to the lower branch emerging from the saddle-node bifurcation in Fig. 4.20 and represent nucleation solutions.

stability analysis. The lower branch has an amplitude that goes to zero when the domain size approaches the critical wavelength $L_c = 2\pi/k_c$ obtained in the linear stability analysis. It represents *nucleation* solutions – unstable solutions that need to be overcome in order to break a film into structures with a length scale smaller than $L_c$.

As visible from Fig. 4.21, an increase of the domain size results in a change of the solution shape, until eventually a coexistence of two film and solute thicknesses, corresponding to the values on the binodal line (discussed in Section 4.6), is established. Such "pancake" drops could otherwise not be obtained with a disjoining pressure based on two power laws. Two nucleation solutions belonging to the lower branch are shown in Fig. 4.22.

Next, we look at the time evolution of flat homogeneous films in 1D. For the time dependent calculations, Eqs. (4.27) and (4.28) are solved numerically using a second order central finite difference scheme in space. For the time integration, we used a variable-order and variable-step Backward Differentiation Formulae algorithm. The number of grid points used is chosen depending on the total length of the system. Knowing the domain size $L$, one can determine the grid spacing

in $x$. In all calculations, periodic boundary conditions for both the fields ($h$ and $\psi$) are used. As an initial condition we use a flat $h$ and $\psi$ profiles which are then perturbed by a small (0.1%) uniform noise. It is carefully checked that the total volume of $h$ and $\psi$ does not change during this process.

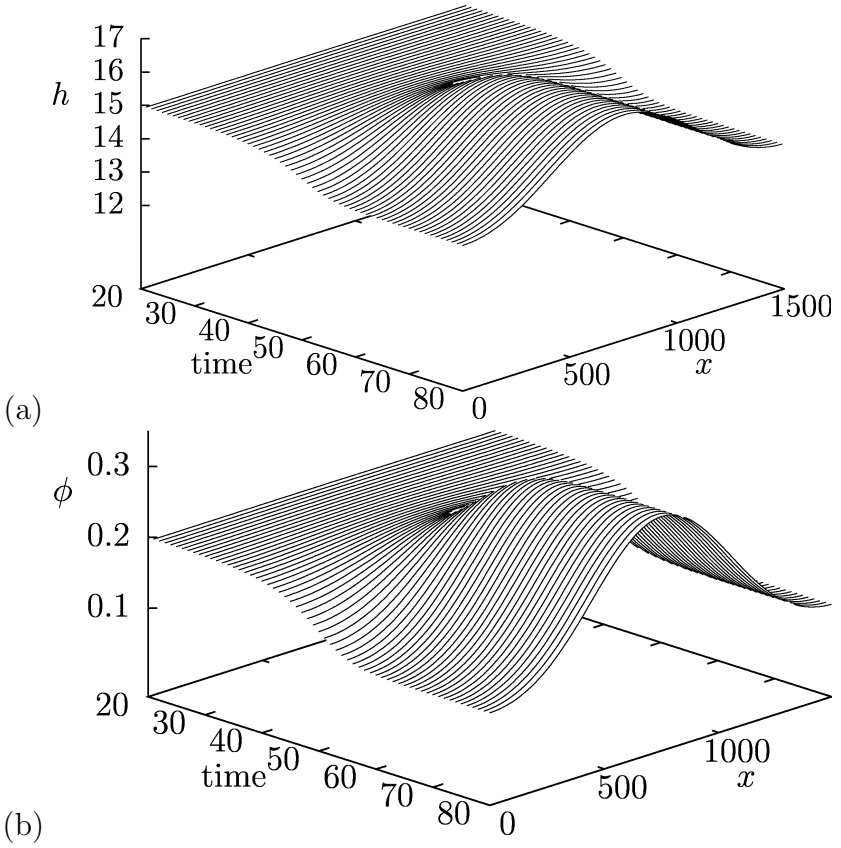


FIGURE 4.23: Time evolution of film thickness (a) and concentration (b) profiles for $\delta = -1$ (stable solvent), $M_1 = -3, h_0 = 15, \phi_0 = 0.2$ and (a) $M_2 = 0.0002, L = 1500$.

Figs. 4.23 (a) and (b) show "space-time" plots corresponding to the time evolution of the film thickness and concentration profiles for a system with parameters as given in the legend. Starting from a flat film with uniformly distributed solute, one observes how a droplet forms with a peak of solute concentration inside. For this particular choice of parameters, the local concentration increases with the film thickness and exhibits a maximum corresponding to the maximum of the local film thickness.

Fig. 4.24 shows some selected height and concentration profiles corresponding to consecutive stages of the time evolution for the very same case shown in Fig. 4.23.

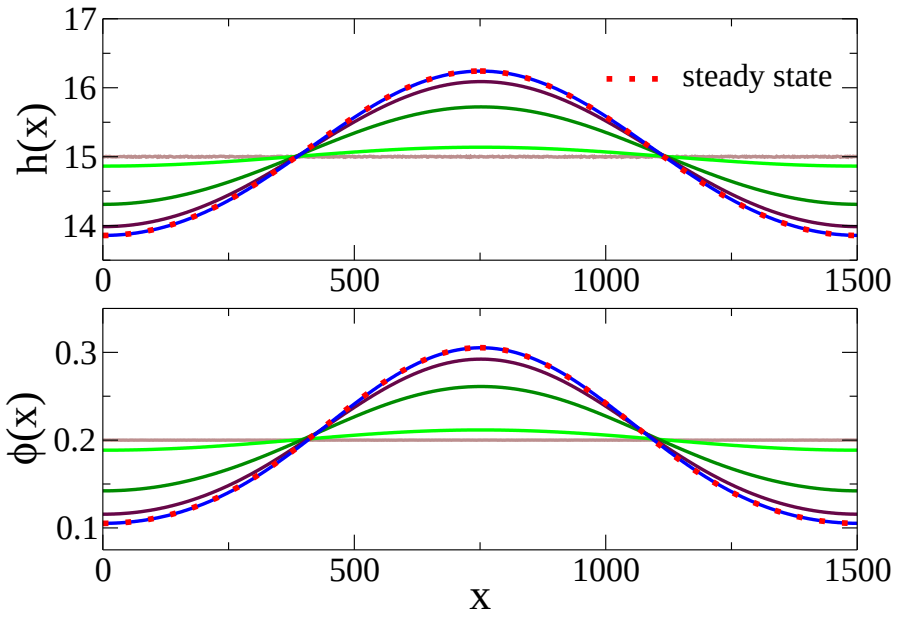


FIGURE 4.24: Time evolution of a flat film (solid brown line) on a solid substrate. The system is characterised by $\delta = -1$ (stable solvent), $M_1 = -3, h_0 = 15, \phi_0 = 0.2$ and $M_2 = 0.0002, L = 1500$ (linearly unstable region in Fig. 4.17). The solid lines of different colour represent subsequent profiles obtained through the time evolution until a stationary shape is established (solid blue line). The dotted red line is the steady state, obtained with AUTO.

The figure serves to demonstrate that in the final stage of the time evolution, the $h$ and $\phi$ profiles agree very well with the steady state profiles that minimise the free energy, obtained by numerical continuation.

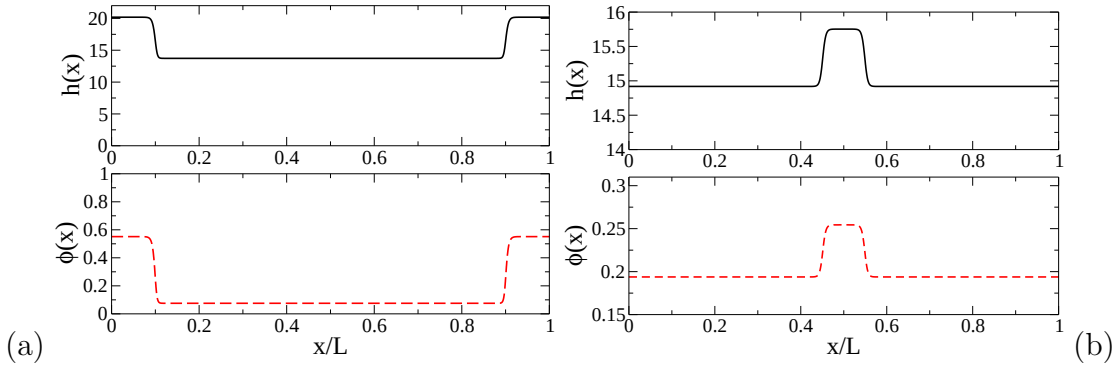


FIGURE 4.25: Film thickness and concentration profiles for $\delta = -1$ (stable solvent), $M_1 = -3, h_0 = 15, \phi_0 = 0.2$ and (a) $M_2 = 0.0002, L = 10^5$ (linearly unstable region in Fig. 4.17) or (b) $M_2 = 0.00025, L = 5 \times 10^5$ (linearly stable region).

Fig. 4.25 shows stationary solutions for the film thickness of the mixture and the corresponding concentration of the solute, for parameter configurations belonging

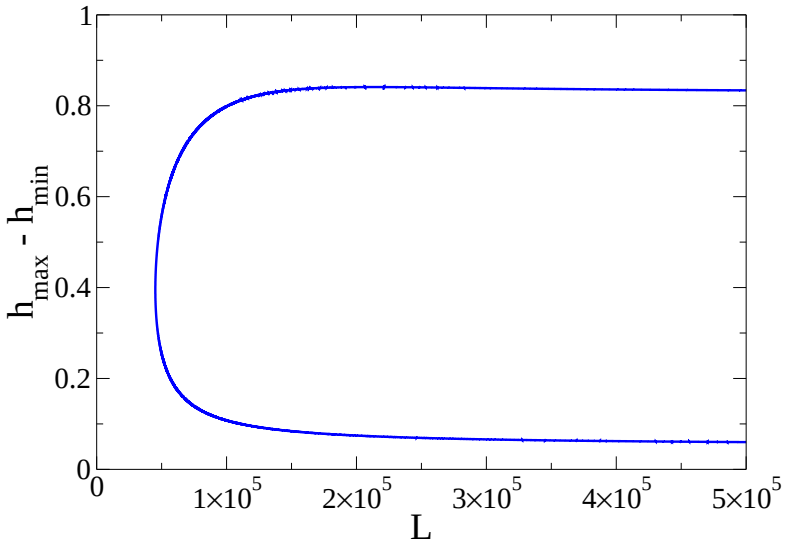


FIGURE 4.26: Solution families obtained when varying the domain size for fixed $\delta = -1, h_0 = 15, \phi_0 = 0.2$, $M_2 = 0.00025$ and $M_1 = -3$ .

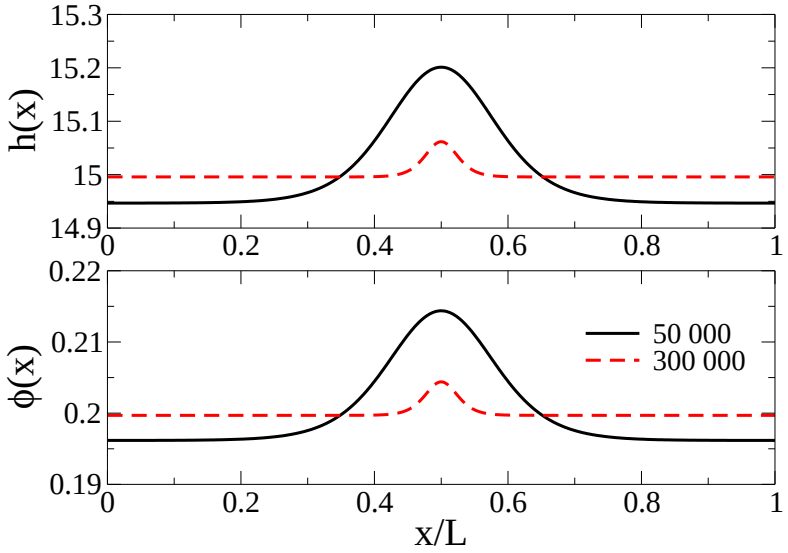


FIGURE 4.27: Film thickness and the corresponding solute concentration profiles of two different domain sizes $L$, as given in the legend. The profiles belong to the lower branch emerging from the saddle-node bifurcation in Fig. 4.26 and represent nucleation solutions.

to the linearly unstable (a) and the linearly stable (b) regions in Fig. 4.17. The second one is obtained by using $M_2$ as a continuation parameter starting with the profile in (a). In analogy to the case pictured in Fig. 4.20, first, a family of solutions is obtained in dependence of domain size $L$ for fixed $h_0 = 15, \phi_0 = 0.2, M_1 = -3$ and $M_2 = 0.0002$. The profile at $L = 10^5$ from the resulting branch of stable

solutions is shown in Fig. 4.25 (a). Keeping all the other parameters fixed, but increasing $M_2$ to 0.00025, we cross the stability border and enter the linearly stable region. Now we continue in $L$ again and obtain the family shown in Fig. 4.26. It qualitatively differs from the one in Fig. 4.20. The flat film is metastable, i.e. there exist two branches of periodic solutions that both continue towards infinite period, as shown in Fig. 4.26. The lower branch represents linearly unstable nucleation solutions for different domain sizes, while the upper branch represents the linearly stable solutions similar to the ones shown in Fig. 4.21. A stable profile at large domain size from the upper branch is pictured in Fig. 4.25 (b), while Fig. 4.27 represents two profiles from the lower branch of Fig. 4.26, i.e. nucleation solutions and the corresponding concentration profiles.

Fig. 4.28 shows the binodal curves in terms of the coexisting equilibrium film thicknesses $h$ (solid black lines) and solute concentration $\phi$ (dashed red lines) for $\delta = -1$ and four parameter sets, as explained in the caption. The dotted vertical lines mark the situation captured in Fig. 4.25 (a) and its crossing points with the binodal curves agree well with the coexisting values in Fig. 4.25 (a). This demonstrates that knowledge of the binodal curves $h_b$ and $\phi_b$ over $h_0, \phi_0, M_1$ or $M_2$ with the rest of the parameters fixed, allows us to predict the coexisting film thickness and concentration values relevant at large domain sizes (and long times).

It is interesting to note that the turning points of the binodal curves in Fig. 4.28 do not coincide with the linear stability thresholds indicated by the vertical dashed orange lines, which is best visible in Fig. 4.28(b). The reason for this is the existence of the metastable region discussed earlier – the system is unstable to finite amplitude disturbances and for large system sizes one observes coexisting states.

The steady state configuration, which we just described, is universal for $\delta = -1$. In all of the studied cases within the linearly unstable region of the corresponding $M_1 : M_2$ diagram for $M_1 < 0$ the solution families look like the one shown in Fig. 4.20. In all of the observed cases, the flat film appears to be metastable in a small region close to the stability border. However, in the half-plane $M_1 > 0$ we were not

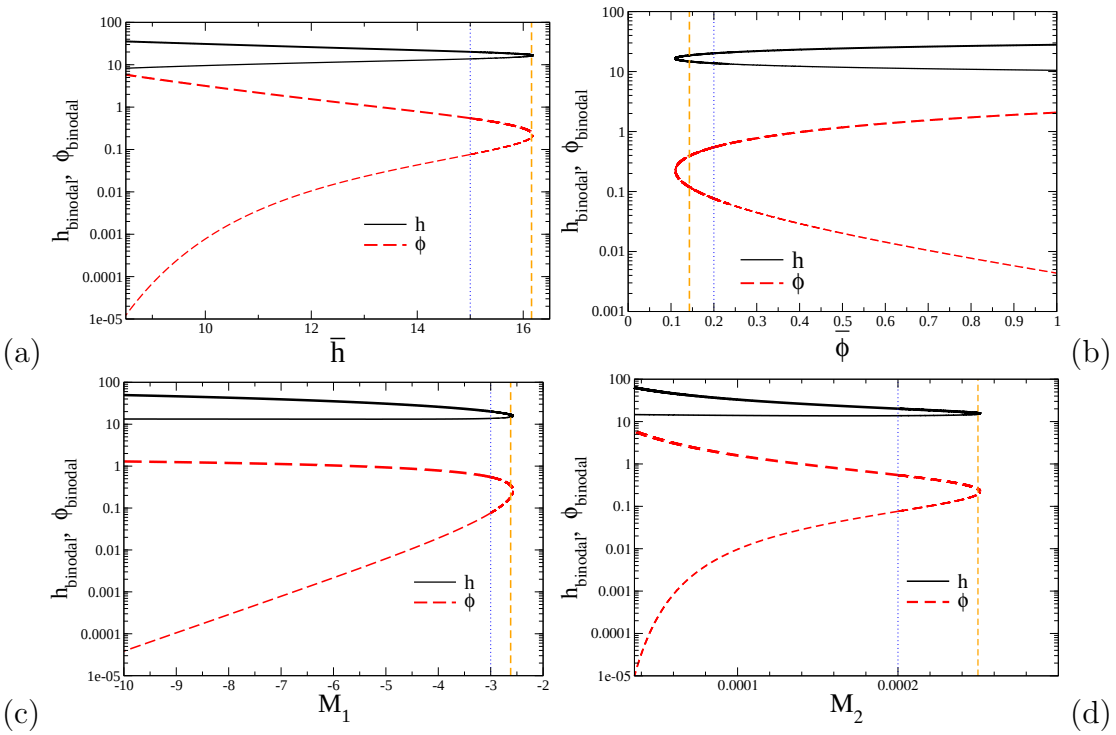


FIGURE 4.28: Binodal lines corresponding to coexisting equilibrium film thicknesses $h$ (solid black lines) and solute concentration $\phi$ (dashed red lines) for $\delta = -1$ (stable solvent) as functions of (a) the mean film thickness for fixed $\phi_0 = 0.2, M_1 = -3, M_2 = 0.0002$, (b) the mean solute concentration for fixed $h_0 = 15.0, M_1 = -3, M_2 = 0.0002$, (c) $M_1$ for fixed $h_0 = 15, \phi_0 = 0.2, M_2 = 0.0002$ and (d) $M_2$ for fixed $h_0 = 15, \phi_0 = 0.2, M_1 = -3$. The vertical dotted blue lines mark the case shown in Fig. 4.25(a), whereas the vertical dashed orange lines indicate the linear stability threshold. Note, that it does not coincide with the critical point of the binodal curves. The two different thicknesses of the binodal lines indicate correspondence between the coexisting thicknesses and concentrations in the two phases.

able to obtain any linearly stable steady solutions for large domain sizes, as in all the cases we looked at, numerical convergence problems occurred most probably because the concentration locally becomes very small ($< 10^{-6}$). Below, the case is further studied.

As an example, we consider the case when $h_0 = 10$ and $\phi_0 = 0.3$. The corresponding stability diagram in the $(M_1, M_2)$–plane is shown in Fig. 4.29.

Employing linear stability analysis, now we calculate the dispersion relations corresponding to points from the linearly unstable region at $M_1 > 0$, marked by coloured square symbols in Fig. 4.29, where the colour code corresponds to the

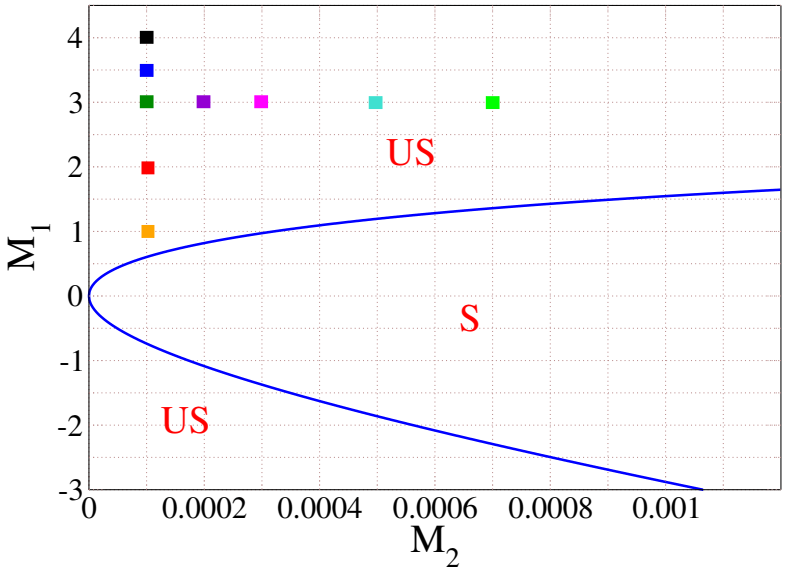


FIGURE 4.29: Stability diagram in the $(M_1, M_2)$ – plane for fixed $\delta = -1$, $\phi_0 = 0.3$ and $h_0 = 10$. The coloured boxes mark points from the stability diagram, for which we present the corresponding dispersion relations in Figs. 4.30 and 4.31, where the same colour coding is used.

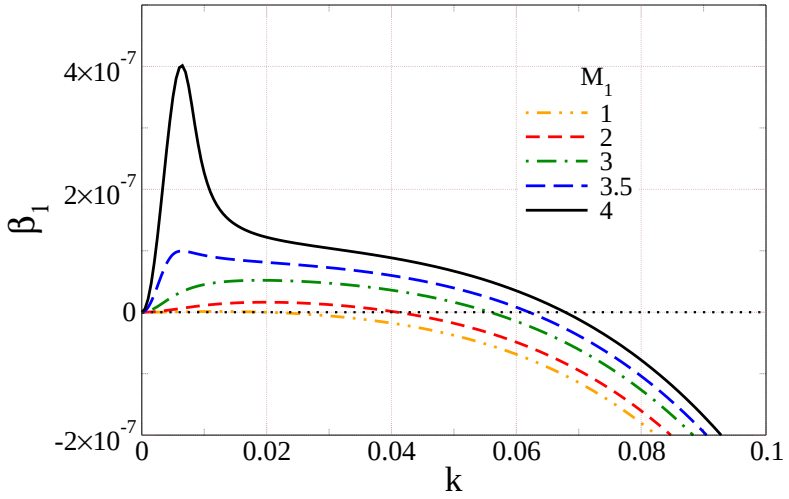


FIGURE 4.30: Dispersion relations for a flat film of mixture on a horizontal substrate for $\delta = -1$ (stable solvent), $\phi_0 = 0.3, h_0 = 10$ and $M_2 = 0.0001$. The colour code corresponds to different values of the parameter $M_1$, as given in the legend.

one used in Figs. 4.30 and 4.31, which represent dispersion relations, i.e. the dependence of growth rate $\beta_1$ on the wave number $k$. In the case shown in Fig. 4.30 we have chosen $M_2 = 0.0001$ and the different curves result for the five values of $M_1$ given in the legend. As one increases the value of $M_1$ and moves further from the linearly stable region, the critical wave number increases - the instability onset

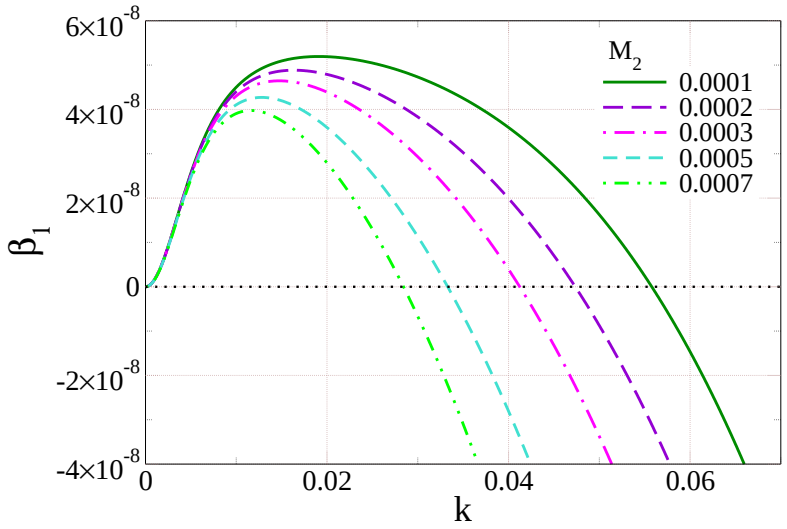


FIGURE 4.31: Dispersion relations for a flat film of mixture on a horizontal substrate for $\delta = -1$ (stable solvent), $\phi_0 = 0.3, h_0 = 10$ and $M_1 = 3$. The colour code corresponds to different values of the parameter $M_2$, as given in the legend.

occurs at smaller domain size, as observed earlier in Fig. 4.18. In the case when $M_1$ is fixed (Fig. 4.31) and we increase the value of $M_2$, the critical wave number increases as well.

If we pick a point from the linearly unstable region, e.g. $M_1 = 3, M_2 = 0.0005$ (light blue square symbol in Fig. 4.29 and the corresponding dispersion relation in Fig. 4.31) and use the predicted critical domain size to start a continuation run that varies the domain size, we obtain the solution family shown in Fig. 4.32 (a). The obtained branch consists of nucleation solutions, as the one shown in Fig. 4.33. The calculation terminates at the red square. The shape of the concentration profile, well visible in Fig. 4.33 (b), suggests that the reason for the termination of the calculation is purely numerical, as there appears to be a sharp transition between the high solute concentration where the film is depressed, and the extremely low concentration where the film is elevated. The closer one gets to the red square in Fig. 4.32 (a), the smaller the concentration outside the hole becomes, until it eventually reaches values smaller than $10^{-6}$.

Another possible situation is the one captured in Fig. 4.32 (b), where the solution branch bifurcates at $L_c$ supercritically from the unstable flat film, but does not

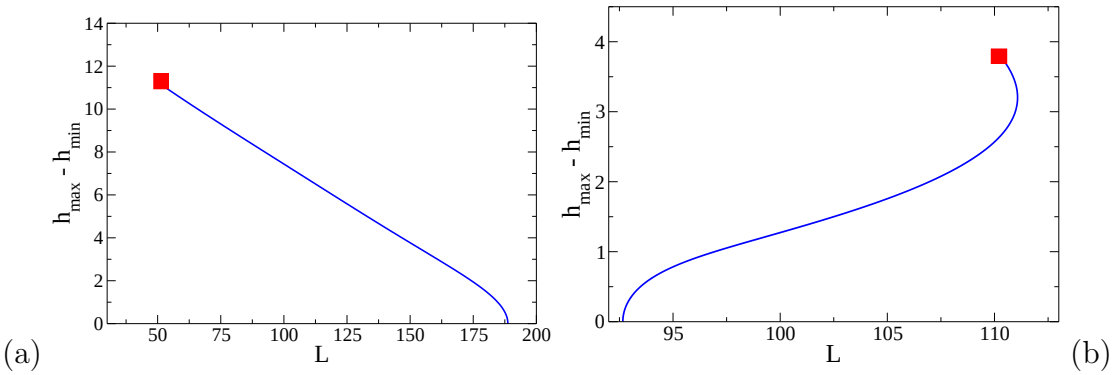


(a) (b)

FIGURE 4.32: Solution family obtained when varying the domain size for fixed $\delta = -1$ (stable solvent), $h_0 = 10, \phi_0 = 0.3$ and (a) $M_2 = 0.0005$, $M_1 = 3$ or (b) $M_2 = 0.0001$, $M_1 = 4$. The red square marks the region where the branch calculation terminates due to a numerical issue.

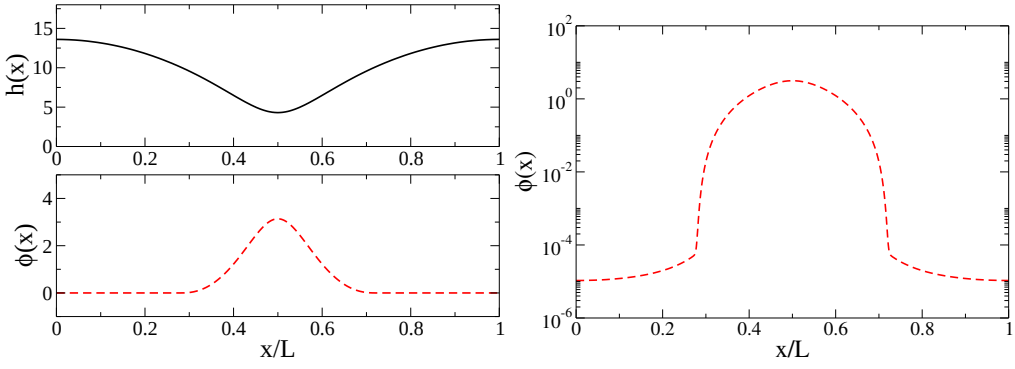


(a) (b)

FIGURE 4.33: Film thickness and concentration profiles for domain size $L \approx 50$ in proximity of the red square region from Fig. 4.32 (a) for $\delta = -1$ (stable solvent), $M_1 = 3, h_0 = 10, \phi_0 = 0.3$ and $M_2 = 0.0005$ in (a) linear and (b) logarithmic scale for the concentration field.

continue towards infinite period. Instead, the solution branch undergoes a saddle-node bifurcation, i.e. it folds back towards smaller $L$. Then, however, the same problem with an extremely low local concentration is encountered. This case is for $M_2 = 0.0001$ and $M_1 = 4$ and corresponds to the black square symbol in Fig. 4.29 and the black dispersion relation curve in Fig. 4.30. Two steady state profiles in proximity of the red square in Fig. 4.32 (b) are given in Fig. 4.34. Again, the shape of the concentration profiles indicates that the reason for the termination of the calculation is purely numerical.

On Fig. 4.35 is shown the time evolution of a film with parameters as given in the legend. Starting from a flat film with uniformly distributed solute, a droplet forms with a peak of solute concentration corresponding to the minimal film thickness.

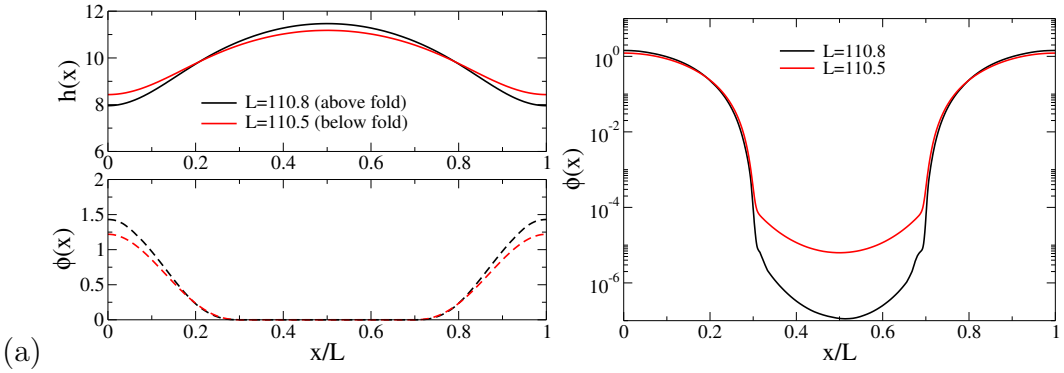


FIGURE 4.34: Film thickness and concentration profiles for domain size $L$ in proximity of the red square region from Fig. 4.32 (b) for $\delta = -1$ (stable solvent), $M_1 = 4, h_0 = 10, \phi_0 = 0.3$ and $M_2 = 0.0001$ in (a) linear and (b) logarithmic scale for the concentration field.

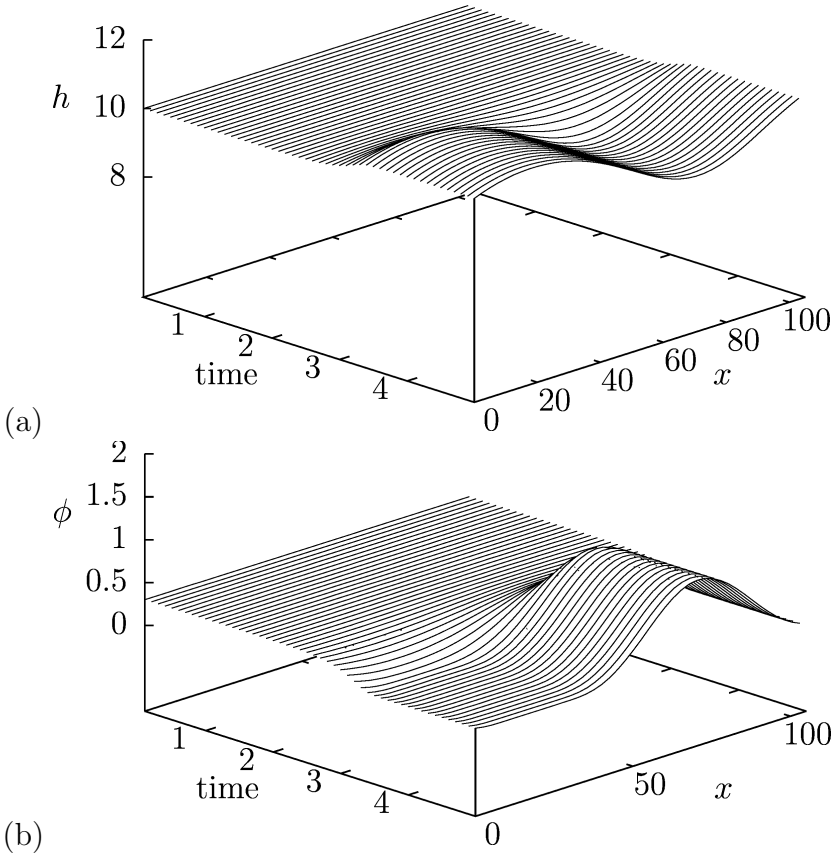


FIGURE 4.35: Time evolution of film thickness (a) and concentration (b) profiles for $\delta = -1$ (stable solvent), $M_1 = 4, h_0 = 10, \phi_0 = 0.3$ and (a) $M_2 = 0.0001, L = 110$.

Eventually, the shape of the evolving film and concentration profiles converge into the stationary shapes obtained by numerical continuation.

### 4.7.2 Unstable solvent

Next we focus on the case $\delta = 1$, when a film of the pure solvent is linearly unstable, i.e. the Hamaker constant of the pure solvent $A_0$ is positive. Examples for systems with $A_0 = \delta|A_0| > 0$ are given in Table 4.3 and include PS + PMMA, Toluene + PS and PMMA + PSAN on $SiO_2$ substrates. Depending on the sign of the coefficient $M_1$, when increasing the mean concentration of the solute $\phi_0$, the Hamaker constant of the mixture can stay positive for all $\phi_0$, if $M_1 > 0$, or it may switch sign at some $\phi_0$ if $M_1 < -1$.

#### 4.7.2.1 Linear stability

As an example we consider a system, characterised by $\delta = 1$ and $\phi_0 = 0.2$. Linear stability diagrams in the $(M_1, M_2)$ – plane are shown in Figs. 4.36 and 4.37. The first one demonstrates how the stability border shifts when we increase the mean film thickness from $h_0 = 10$ to $h_0 = 15$ – the stable region moves towards larger $M_2$. This implies that for a given combination of materials, thicker films are stabilised at smaller entropic influences. In the limit of very thick films ($h_0 \gg 1$), one observes that the film is always stable for $A = |A_0|(\delta + M_1\phi) < 0$. The coordinates of the turning point of the stability threshold are $(M_1, M_2) = \left(\frac{4B-2\delta h_0^3}{h_0^2\psi_0}, \frac{-6B+3\delta h_0^3}{h_0^5\psi_0}\right)$ and in the limit $h_0 \gg 1$ one finds $(M_1, M_2) = \left(-\frac{2\delta}{\phi_0}; 0\right)$. The dotted line represents the case when the concentration of the solute is imposed to remain homogeneous and practically does not change when one varies $h_0$ (cf. Eq. 4.55).

Fig. 4.37 demonstrates the influence of $\phi_0$ when all the remaining parameters are fixed, as given in the caption. Increasing the concentration the linearly stable region in the $(M_1, M_2)$–plane expands towards smaller values of $M_2$ and the turning point adjusts accordingly. The dotted lines correspond to the case of imposed homogeneous concentration.

Figs. 4.38 and 4.39 show the stability thresholds in the $(M_1, h_0)$-plane for fixed $M_2$ and different values of $\phi_0$ and fixed $\phi_0$ and two values of $M_2$, respectively.

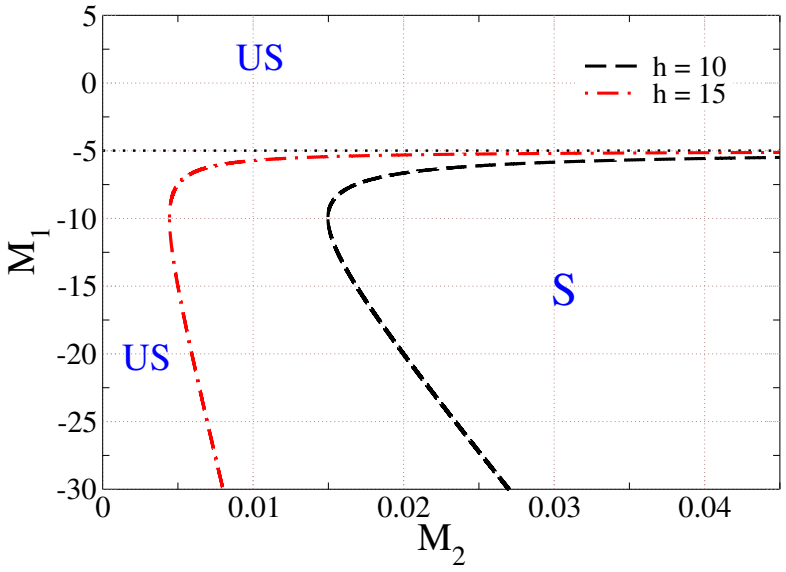


FIGURE 4.36: Stability diagram in the space spanned by $M_1$ and $M_2$ for fixed $\delta = 1$ (unstable solvent), $\phi_0 = 0.2$ and $h_0 = 10$ (dashed black line) or $h_0 = 15$ (dot-dashed blue line). The stability regions are marked "S" for "stable" and "US" for "unstable". The thin dotted red line is the stability border for the case when the concentration of solute is assumed to remain homogeneous. It is practically the same for all $h_0 \gtrsim 10$, about $1/\phi_0$.

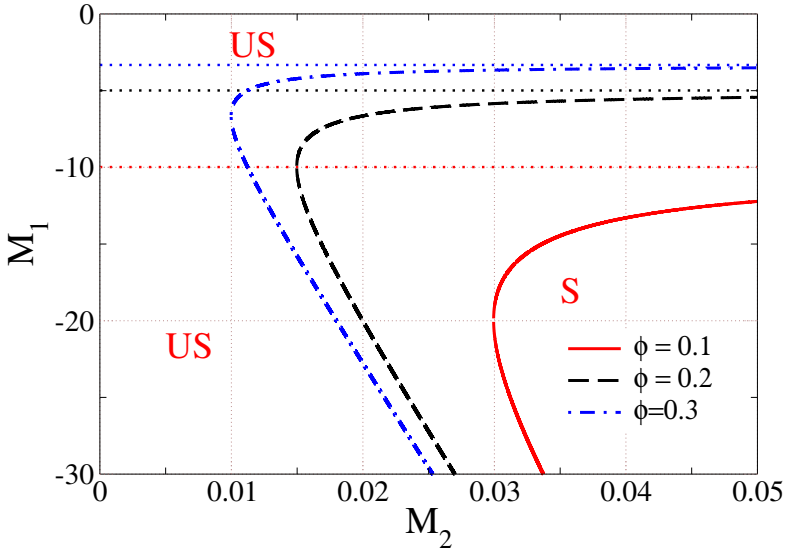


FIGURE 4.37: Stability diagrams in the space spanned by $M_1$ and $M_2$ for fixed $\delta = 1$ (unstable solvent), $h_0 = 10$ and $\phi_0 = 0.1$ (solid red line), $\phi_0 = 0.2$ (dashed black line) or $\phi_0 = 0.3$ (dot-dashed blue line). The stability regions are marked "S" for "stable" and "US" for "unstable". The thin dotted lines mark the stability borders corresponding to the case of imposed homogeneous concentration.

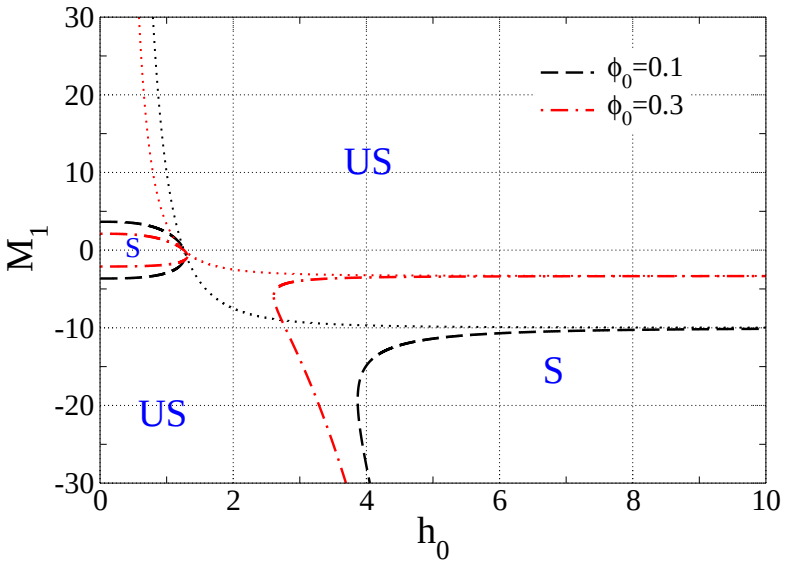


FIGURE 4.38: Stability diagrams in the space spanned by $M_1$ and $h_0$ for fixed $\delta = 1$ (unstable solvent), $M_2 = 0.5$ and $\phi_0 = 0.1$ (dashed black lines) or $\phi_0 = 0.3$ (dot-dashed red lines). The stable and unstable regions are marked "S" and "US", respectively. The two thin dotted lines mark the respective stability borders corresponding to the case of imposed homogeneous concentration.

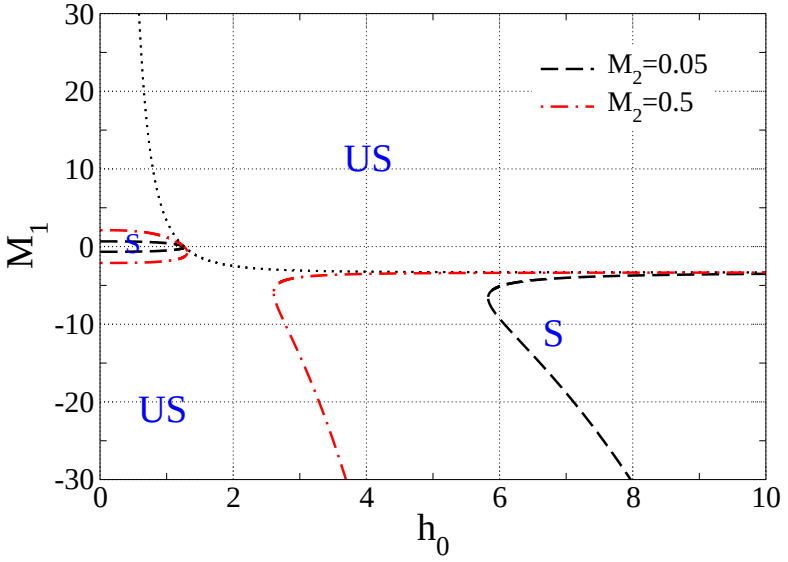


FIGURE 4.39: Stability diagrams in the space spanned by $M_1$ and $h_0$ for fixed $\delta = 1$ (unstable solvent), $\phi_0 = 0.3$ and$M_2 = 0.05$ (dashed black lines) or $M_2 = 0.5$ (dot-dashed red lines). The stable and unstable regions are marked "S" and "US", respectively. The thin dotted line is the stability border for imposed homogeneous concentration and it is valid for any $M_2$.

The thin dotted lines represent the case in which the concentration of the solute is imposed to be homogenous at all times.

#### 4.7.2.2 Non-linear steady states

Further, we investigate the types of steady profiles which occur in the parameter space in the case of an unstable solvent, or $\delta = 1$. We fix the mean solute concentration to $\phi_0 = 0.3$ and the mean film thickness of the mixture film to $h_0 = 10$. The corresponding $(M_1, M_2)$–diagram is shown in Fig. 4.40.

In analogy to Section 4.7.1, we employ linear stability analysis to calculate the dispersion relations corresponding to coloured square symbols in the unstable regions of Fig. 4.40, where the colour code corresponds to the one used in Figs. 4.41 and 4.42.

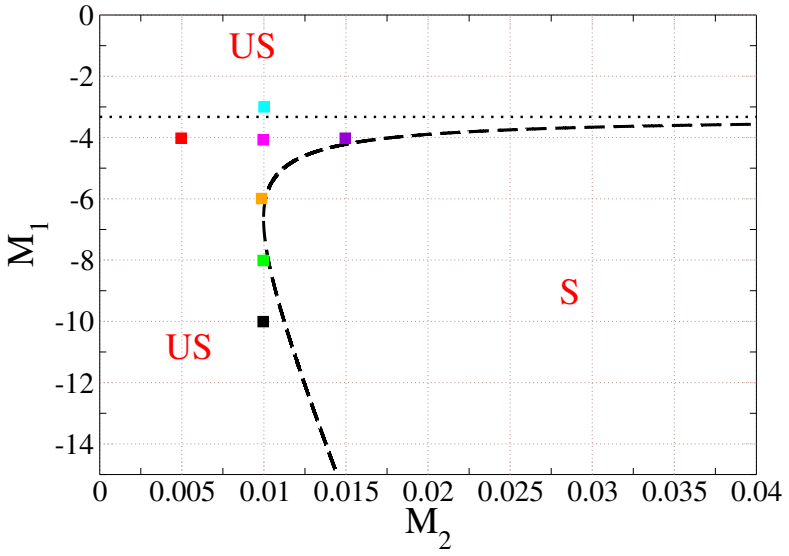


FIGURE 4.40: Stability diagram in the space spanned by $M_1$ and $M_2$ for fixed $\delta = 1$ (unstable solvent), $\phi_0 = 0.3$ and $h_0 = 10$. The regions are marked "S" for "stable" and "US" for "unstable". The coloured square symbols mark points for which we present the corresponding dispersion relations in Figs. 4.41 and 4.42.

We observe how the shape of the dispersion relations and the value of the critical wave number $k_c$ change between different positions in the stability diagram. In Fig. 4.41 we see that the value of the critical wave number $k_c$ changes non-monotonously when we increase the value of $M_1$. At first, while approaching the turning point of the stability threshold in the linearly unstable region, increasing the parameter $M_1$ from $-10$ to $-6$, $k_c$ decreases. Once we start going further from

the turning point, i.e. changing $M_1$ from $-6$ to $-3.5$, $k_c$ starts to increase. When we fix $M_1$ and change $M_2$, $k_c$ increases with $M_2$, as shown in Fig. 4.42.

Also, it is interesting to note that the growth rate characterising the fastest growing mode, $\beta_{\max}$, changes non-monotonically when one changes $M_1$. At first, when $M_1$ increases and one approaches the stable region in Fig. 4.40, $\beta_{\max}$ decreases and so does the corresponding wave number $k_{\max}$ (cf. Fig. 4.41). However, once one starts to move away from the linearly stable region, both $\beta_{\max}$ and $k_{\max}$ increase. On the other hand, when one fixes $M_1$ and varies $M_2$, one observes that $\beta_{\max}$ and $k_{\max}$ decrease when $M_2$ increases, as visible in Fig. 4.42.

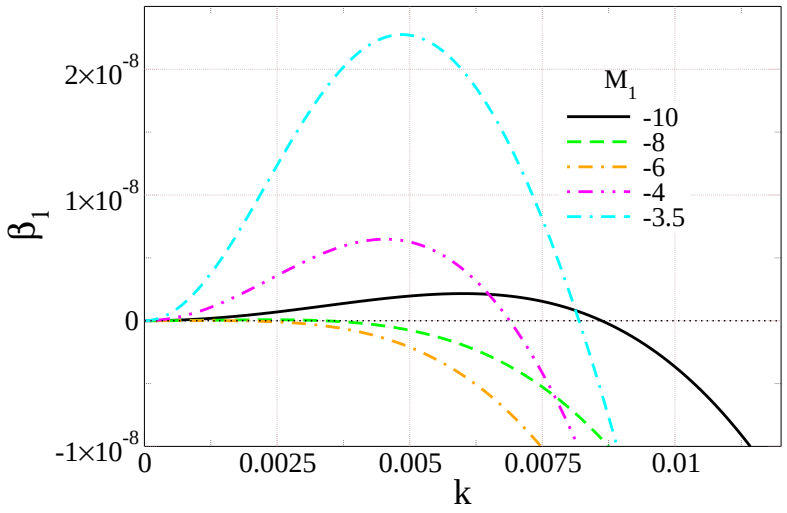


FIGURE 4.41: Dispersion relations for a flat film of mixture on a horizontal substrate for various values of $M_1$ as given in the legend. The remaining parameters are fixed: $\delta = 1$ (unstable solvent), $\phi_0 = 0.3, h_0 = 10$ and $M_2 = 0.01$. The colouring of the curves corresponds to the one of the square symbols in Fig. 4.40.

Fig. 4.43 (a) shows a typical solution family obtained by varying the domain size $L$, starting from the critical one determined from the linear stability analysis. All steady states on the solution branch shown in Fig. 4.43 (a) are nucleation solutions. When reducing $L$, a numerical convergence problem does not allow us to reach domain sizes below the red square or indeed the upper (stable) branch that we expect. Two film thickness and concentration profiles in the proximity of that region are given in Fig. 4.43 (b). Apparently, the local solute concentration in the

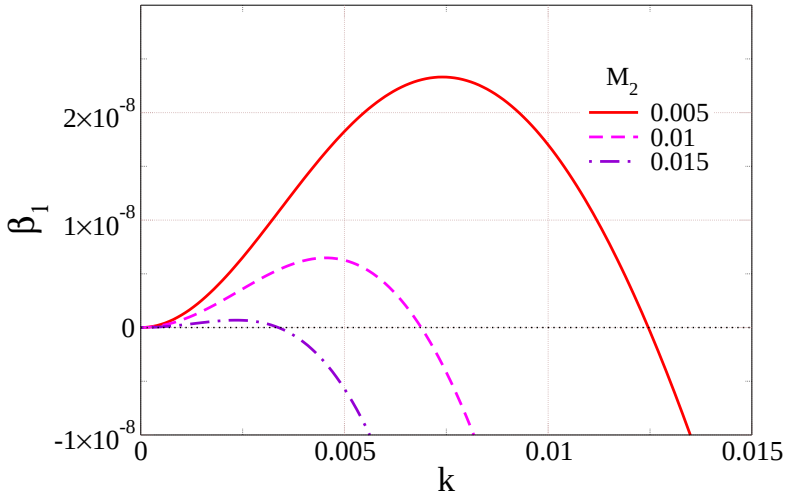


FIGURE 4.42: Dispersion relations for a flat film of mixture on a horizontal substrate for selected values of the parameter $M_2$ as given in the legend. The remaining parameters are $\delta = 1$ (unstable solvent), $\phi_0 = 0.3, h_0 = 10$ and $M_1 = -4$. The colouring of the curves corresponds to the one used for the square symbols in Fig. 4.40.

film becomes very small ($\phi \approx 10^{-6}$), as already observed in Section 4.7.1. The time evolution computations confirm that all the explored cases are unstable.

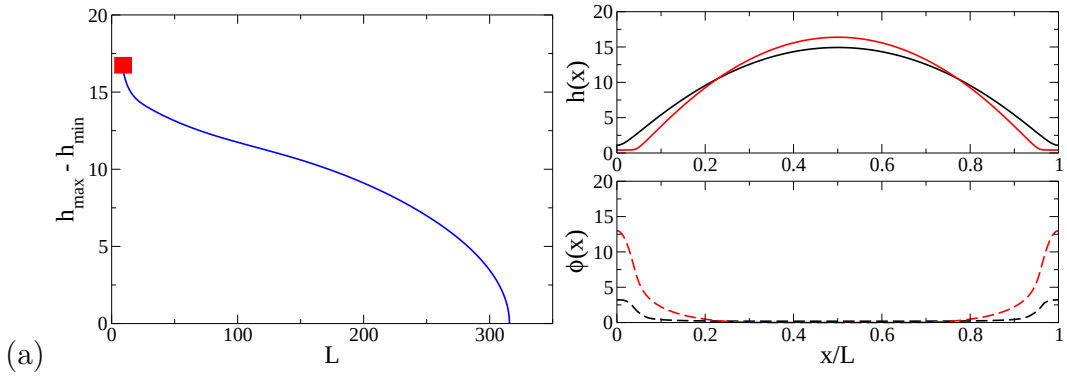


(a) (b)

FIGURE 4.43: (a) Solution family obtained when varying the domain size for fixed $\delta = 1, h_0 = 10$, $M_2 = 0.01$ and (b) $M_1 = 1$ and film thickness and solute concentration profiles, corresponding to the red square region in (a).

Fig. 4.44 shows the binodal curves in terms of the coexisting equilibrium film thicknesses $h$ (solid black lines) and solute concentration $\phi$ (dashed red lines) for $\delta = 1$ and parameter sets, as explained in the caption. The two different thicknesses of the binodal lines indicate correspondence between the coexisting thicknesses and concentrations in the two phases. One observes in Fig. 4.44 that the upper binodal thickness $h_{\text{binodal}}$ diverges when the mean film thickness approaches the value of

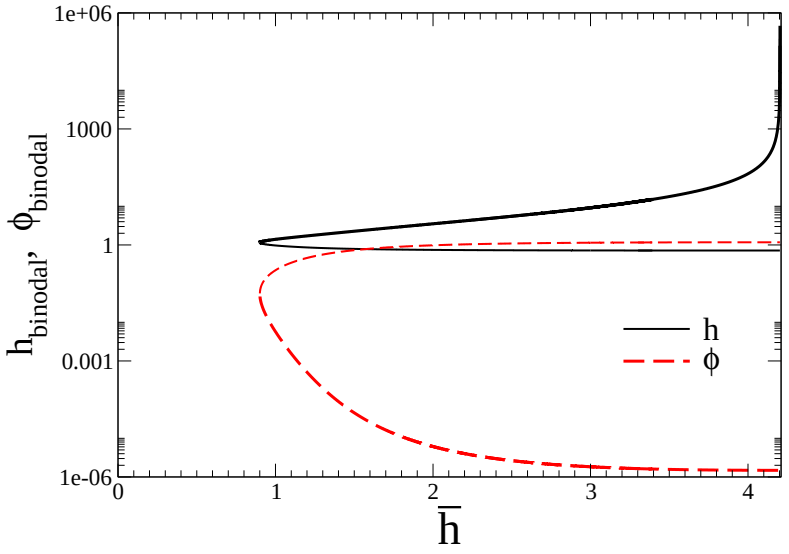


FIGURE 4.44: Binodal lines giving coexisting equilibrium film thicknesses $h$ (solid black lines) and solute concentrations $\phi$ (dashed red lines) as functions of the mean film thickness for fixed $\delta = 1, \phi_0 = 0.2, M_1 = 1$ and $M_2 = 0.1$. The two line thicknesses indicate correspondence between the coexisting thicknesses and concentrations in the two phases.

about 4.2. Unfortunately, we were not able to obtain any steady solutions for this case.

## 4.8 Conclusions

In this Chapter we have investigated the influence of the concentration-dependent wettability on the behaviour of thin films of non-volatile liquid films of mixtures. We have discussed in Section 4.2.1 how the Hamaker constant of simple liquids on solid substrates can be calculated in the framework of the Lifshitz theory using the permittivities and refractive indices of the solid, liquid and gas phase. In Section 4.2.2 we have introduced the Effective Medium Approximation (EMA) – a technique, which has allowed us to calculate effective permittivities and refractive indices of inhomogeneous media, based on knowledge about the optical indices of its components. Further, in Section 4.2.3 we have showed how EMA can be combined with the Lifshitz theory to obtain concentration–dependent Hamaker constants for films of mixtures on solid substrates. Next, in Section 4.2.4 we have

presented the results for the Hamaker constants for a set of selected systems with mixtures and suggested that for most of the systems we are interested in, the relevant Hamaker constants can be confidently approximated by a linear function of the solute concentration, distinguishing two main cases for the studied systems. The first case considers systems, for which a film of pure solvent is stable on its own while the second one includes cases for which the pure solvent forms an unstable film on its own.

Further, in Section 4.3 we have discussed coupled thin film equations for the film thickness and effective local solute thickness for films of mixtures. First, we have demonstrated how the free energy of the system can be extended to include a concentration–dependent wetting energy. It has then been incorporated into the gradient dynamics formulation of the coupled equations, which were introduced in Section 2.3.2. We have also discussed the resulting Euler–Lagrange equations describing film thickness and concentration profiles minimising the free energy of the system, i.e. the steady states. We have continued in Section 4.4 by demonstrating a procedure of non-dimensionalisation of the governing coupled equations and introducing a set of non-dimensional parameters characterising the problem. Next, in Section 4.5 we have analysed the linear stability of flat films of mixtures and we have discussed how one can obtain the stability thresholds in the space spanned by the non-dimensional parameters entering the non-dimensional free energy functional, and the mean film thickness and mean solute concentration. In Section 4.6 we have shown how the binodal lines for the studied case of mixtures can be calculated, allowing us to predict coexisting film and solute layer thicknesses.

Section 4.7 contains our main results for the two main cases we have studied, namely for stable and unstable solvent, presented in Sections 4.7.1 and 4.7.2, respectively. For the case of a stable solvent, we have first investigated how the linear stability borders change when once a solute is introduced into the system. The most spectacular effect we have observed is that even when both, the pure solvent and pure solute, are stable on their own, there still can exist a region in

the parameter space where the mixture of the two is linearly unstable. This observation is not trivial at all, as it points to the existence of a new type of thin film instability based on the coupling of fluctuations of the height and concentration. We have further investigated this finding in Section 4.7.1.2 where we have discuss dispersion relations and non-linear steady states. The latter we have compared to the binodal solutions for large computational domains. In Section 4.7.2 we have performed a similar analysis of the case when the pure solvent is unstable. In all of the cases considered we have observed that all of the existing instabilities get stronger due to the coupling between the film height and the solute concentration.

# Chapter 5

# Parameter passing between Molecular Dynamics and continuum models for droplets on solid substrates: The static case

We study equilibrium properties of polymer films and droplets on a solid substrate employing particle-based simulation techniques (Molecular Dynamics) and a continuum description. Parameter-passing techniques are explored that facilitate a detailed comparison of the two models. In particular, the liquid–vapour, solid–liquid and solid–vapour interface tensions, and the Derjaguin (disjoining) pressure are determined by Molecular Dynamics simulations. This information is then introduced into continuum descriptions accounting for (i) the full curvature and (ii) a long-wave approximation of the curvature (the *thin film* model). A comparison of the dependence of the contact angle on droplet size indicates that the theories agree well if the contact angles are defined in a compatible manner.

## 5.1 Introduction

In the previous decade increasing attention has focused on the behavior of small quantities of liquid on hard [13, 21, 81, 129, 132, 134, 162] or soft [109, 151] substrates in equilibrium or under the influence of driving forces parallel to the substrate [101, 149, 173]. Current research mainly considers two levels of description: particle-based models [37, 67, 81, 82, 89, 95, 99, 108] and continuum theory [13, 21, 25, 44, 50, 60, 101, 102, 111, 132, 172, 173, 183]. The former describes the liquid in terms of the position and momenta of particles. These may represent atoms in a chemically realistic model or one lumps together a small number of atoms into an effective interaction center (called "a bead") in a coarse-grained model. The reduction of the number of degrees of freedom and the soft interactions in the coarse-grained description facilitate the study of long time and length scales. The properties of particle-based models are studied by discrete stochastic simulations, i.e., Monte-Carlo simulation or Molecular Dynamics. The advantage of retaining the particle degrees of freedom consists of the ability to refine the model towards a chemically realistic description and to include effects of thermal fluctuations and of discreteness of matter that are expected to become important on small length scales. However, these stochastic simulation techniques are limited to droplets of a linear size that does not exceed a few nanometers.

Continuum models, in turn, describe the liquid in terms of collective variables that do not refer to individual particles. They can address engineering time and length scales but depend on phenomenological material constants that are often not related in a straightforward way to the microscopic interactions of the particle-based description. Thus effort has to be devoted to parameter-passing techniques that transfer information from particle-based models to the continuum description. To this end, two questions have to be addressed: (i) Which is the relevant information of the particle-based model needed in the continuum description and (ii) how can one extract this information from the particle-based description in the appropriate continuum form?

In the present work, we use a coarse-grained particle model of a polymer drop on a solid substrate, and a thin film description that characterizes the droplet shape by the location, $h$, of the liquid–vapour interface above the substrate. We explore the behavior of small nano-drops where both descriptions are computationally feasible. We extract the interface tensions and the Derjaguin or disjoining pressure [39, 132, 157] from Molecular Dynamics simulation of the particle-based model and pass them to continuum model. Then both approaches are used to determine the equilibrium contact angle of a droplet as a function of the size of the droplet and of interaction strength between the liquid and the substrate.

To our knowledge, such a parameter passing scheme has not yet been developed for the case of liquid droplets on solid substrates. However, the disjoining pressure itself can be extracted in grandcanonical ensemble [31, 61, 94, 107, 108]. Additionally, related works exist for other geometries in canonical ensemble, such as free standing films or films adsorbed in pores [68].

Bhatt *et al.* [19] extract a disjoining pressure as a function of chemical potential from MD simulations for a free standing film of a volatile Lennard-Jones liquid and compare the results with the ones of density functional theory. Their approach consists in the definition of the disjoining pressure as the difference of normal pressure in the film and the pressure in the homogeneous liquid at the same chemical potential as the film. However, as discussed in section 5.3, the measurement of the chemical potential in a canonical ensemble is difficult and requires additional simulations. Moreover, despite of truncated potentials, they relate the disjoining pressure with solely long-range van der Waals dispersion forces and provide therefore comparison to Hamaker theory. The short-range forces stay outside the scope of their research.

A planar liquid film bounded by a solid and vapour is studied by Han [63] using grandcanonical MD simulations with a truncated and shifted Lennard-Jones interaction. The disjoining pressure is extracted in a similar way as in Ref. [19] and again is associated with only long-range dispersion forces.

Note that parameter passing from MD simulations to continuum hydrodynamics is also frequently done in the context of liquid flow close to solid substrates [33, 62, 80, 128–130]. However, as these works do either not involve free interfaces [33, 128] or do not extract the disjoining pressure [62, 129, 130], we do here not discuss them further.

This Chapter is structured as follows. In section 5.2 we present the particle-based and continuum approaches. Then, section 5.3 details how we pass the parameters from the particle-based model into the continuum description. The subsequent section 5.4 presents the dependence of the equilibrium contact angle on droplet size for various interaction energies between the liquid and the substrate. In passing, we describe several ways to define the equilibrium contact angle and discuss their relation to the macroscopic Young-Laplace law. Section 5.5 concludes and gives an outlook beyond the case of equilibrium droplets.

The work presented in the Chapter is the result from a collaboration with Dr. Nikita Tretyakov and Prof. Marcus Müller (Institute for Theoretical Physics, Georg August University Göttingen). All the work related to the MD calculations and simulations was done by them and is published in more detail in Dr. Tretyakov's Dissertation [179].

## 5.2 Models

### 5.2.1 Molecular Dynamics (MD)

Here, the mesoscopic discrete stochastic description is provided by Molecular Dynamics simulations of a widely used coarse-grained polymer model [59], i.e., a polymer chain is not represented by each and every individual atom but it is modeled as a flexible, linear string of small conglomerates of atoms. These conglomerates are called "beads". The length of all polymer chains is fixed to $N_p = 10$ monomers [117, 149] in all simulations. The potentials used in MD are represented in Fig. 5.1.

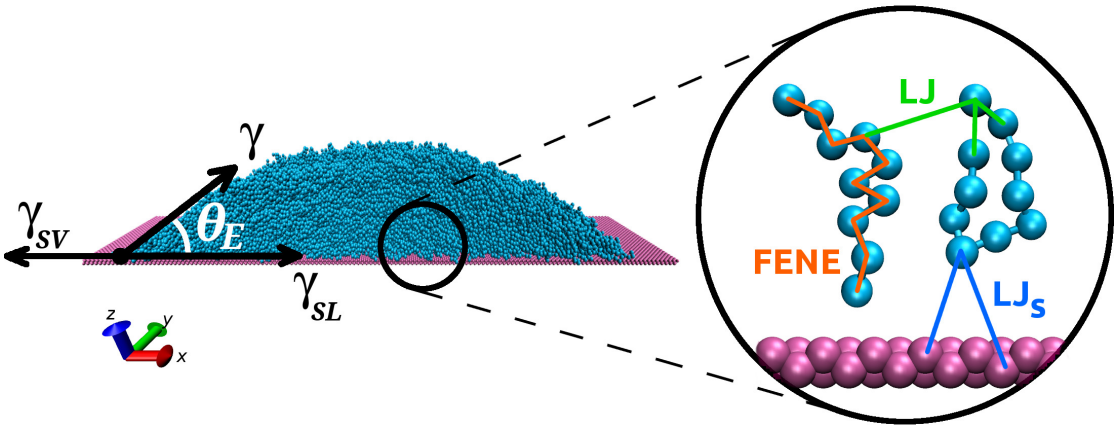


FIGURE 5.1: Snapshot from MD simulation of a cylindrical drop with illustration of Young's equation (left). The enlargement close to the substrate (right) sketches the pairwise bead potentials. Coarse-grained beads of polymer chains (blue) interact with each other and with the substrate modeled by two layers of face-centered-cubic lattice (lila)

All bonded and non-bonded beads have unit mass, $m = 1$, and interact via truncated and shifted Lennard-Jones (LJ) potentials

$$U(r) = U_{\mathrm{LJ}}(r) - U_{\mathrm{LJ}}(r_c) \tag{5.1}$$

with

$$U_{\mathrm{LJ}}(r) = 4\epsilon\left[\left(\frac{\sigma}{r}\right)^{12} - \left(\frac{\sigma}{r}\right)^{6}\right] \tag{5.2}$$

if their distance is smaller than the cutoff distance $r_c = 2 \times 2^{1/6}\sigma$. $U_{\mathrm{LJ}}(r_c)$ is the LJ potential evaluated at the cutoff distance. All LJ parameters are set to unity, $\epsilon = 1$ and $\sigma = 1$, i.e., we express all energies and lengths in units of $\epsilon$ and $\sigma$, respectively. The reduced time unit $\tau$ is set by a combination of the LJ parameters as $\tau = \sigma\sqrt{\frac{m}{\epsilon}}$.

The individual beads are connected into chains employing a finite extensible nonlinear elastic (FENE) potential given by [20, 83]

$$U_{\mathrm{FENE}} = \begin{cases} -\frac{1}{2}kR_0^2 \ln\left[1 - \left(\frac{r}{R_0}\right)^2\right] & \text{for } r < R_0; \\ \infty & \text{for } r \geq R_0, \end{cases} \tag{5.3}$$

where $R_0 = 1.5\sigma$ and $k = 30\epsilon/\sigma^2$.

To control the wettability of the polymeric liquid on the substrate we account for the interaction of the beads with the solid substrate. The substrate is modeled by a fixed array of atoms as in Ref. [149] and not by an ideally smooth and homogeneous wall [95, 117]. Specifically, the substrate is represented by two layers of a face-centered-cubic lattice of atoms with a number density of $\rho_{\mathrm{s}} = 1.5\sigma^{-3}$. We also employ a truncated and shifted LJ interaction between the beads of the liquid and the individual constituents of the substrate

$$U^{\mathrm{s}}(r) = U^{\mathrm{s}}_{\mathrm{LJ}}(r) - U^{\mathrm{s}}_{\mathrm{LJ}}(r_c) \tag{5.4}$$

with the length scale $\sigma_{\mathrm{s}} = 0.75\sigma$. The strength of interaction $\epsilon_{\mathrm{s}}$ is varied. By changing $\epsilon_{\mathrm{s}}$ from $0.2\epsilon$ to $\epsilon$, one tunes the wettability of the system from practically non-wetting (polymer droplet with a contact angle of $\theta_{\mathrm{E}} = 163^{\mathrm{o}}$) to complete wetting (polymer film with $\theta_{\mathrm{E}} = 0^{\mathrm{o}}$).

All simulations are carried out in a computational domain that corresponds to a three dimensional box. Periodic boundary conditions are used in the $x$- and $y$-directions, whereas the range in the $z$-direction is limited by a repulsive ideal wall that is positioned far above the polymer liquid. The domain side lengths, $L_x$ and $L_y$, are chosen in such a way that one may study polymer films, $L_x = L_y$), and two-dimensional drops (i.e., ridges in 3d), $L_y \ll L_x$. These ridges span the simulation box in $y$ direction and have the cylindrical form whose cross-section is well visible in Fig. 5.1. $L_y$ is limited by the Plateau-Rayleigh instability that results in the instability of liquid ridges above a critical length. However, as this instability is normally subcritical [14], in a MD simulation $L_y$ has to be smaller than a critical ridge length $L_{\mathrm{nl}}$ that is smaller than the one resulting from the linear stability analysis of a ridge.

The radius of a 2d drop (3d ridge) scales as $\sqrt{N}$ (in comparison to $N^{1/3}$ for a spherical 3d drop), allowing us to study larger droplets [149]. Moreover, the length of the three-phase contact line, $2L_y$, is independent of the 2d droplet size. Thus, there is no direct effect of the line tension on the shape of the droplet.

The temperature of the system is controlled by a dissipative particle dynamics (DPD) thermostat [52, 70]. Using this DPD thermostat, we maintain the constant temperature, $k_{\mathrm{B}}T = 1.2\epsilon$. For more detail about the DPD thermostat we refer the reader to N. Tretyakov's Thesis [179], as well as Ref. [180]. The equations of motion are integrated with the velocity Verlet algorithm [160] with a time step $\Delta t = 0.005\tau$. The simulations are performed on GPU facilities using the HOOMD Software [1, 9, 120].

The MD simulations are used to determine parameters that are passed on to the continuum model. Before the parameter passing is described in section 5.3, we introduce in the following section the continuum model.

### 5.2.2 Continuum model (CM)

We employ a highly coarse-grained description to characterize the free-energy of a droplet on a planar substrate in terms of the position of the solid–liquid and liquid–vapour interfaces. Generally, the free energy takes the translationally and rotationally invariant form

$$F = \gamma_{\mathrm{SL}} \int_{\mathrm{SL}} \mathrm{d}S + \gamma \int_{\mathrm{LV}} \mathrm{d}S + \int_{\mathrm{LV}} \mathrm{d}S \int_{\mathrm{SL}} \mathrm{d}S' \; \tilde{f}(|\mathbf{r} - \mathbf{r}'|), \tag{5.5}$$

where the integrals extend over the solid–liquid (SL) and liquid–vapour (LV) interfaces [1]. In Eq. (5.5), $\gamma_{\mathrm{SL}}$ and $\gamma$ are the solid–liquid and liquid–vapour interface tensions, respectively. The last term of Eq. (5.5) describes the effective interaction between the interfaces, and $\mathbf{r}$ and $\mathbf{r}'$ are points on the liquid–vapour and solid–liquid interface, respectively. In the following, we restrict our attention to 2d droplets on a planar substrate (cf. Fig. 5.1), choose the $x$-coordinate along the planar solid substrate and denote by $z = h(x)$ the local distance between a point $\mathbf{r} \equiv (x, y, z = h(x))$ of the liquid–vapour interface and the planar substrate

[1] If there exist additional long-ranged interactions, $V_{\mathrm{lr}}$, between the liquid and the solid, then one has the additional contribution $F_{\mathrm{lr}} = \int_{\mathrm{L}} \mathrm{d}^3\mathbf{r} \int_{\mathrm{S}} \mathrm{d}^3\mathbf{r}' \; V_{\mathrm{lr}}(|\mathbf{r} - \mathbf{r}'|)$. Writing $V_{\mathrm{lr}}(|\mathbf{r}|) = \nabla \cdot \mathbf{r}\Phi_{\mathrm{lr}}(|\mathbf{r}|)$, we obtain for the long-range contribution $F_{\mathrm{lr}} = \int_{\mathrm{SL}\cup\mathrm{LV}} \mathrm{d}\mathbf{S} \cdot \int_{\mathrm{S}} \mathrm{d}^3\mathbf{r}' \; (\mathbf{r} - \mathbf{r}')\Phi_{\mathrm{lr}}(|\mathbf{r} - \mathbf{r}'|) = \int_{\mathrm{SL}\cup\mathrm{LV}} \mathrm{d}\mathbf{S} \cdot \mathbf{e}_x f_{\mathrm{lr}}(h)$ with $f_{\mathrm{lr}}(h) = \int_{\mathrm{S}} \mathrm{d}^3\mathbf{r}' \; \mathbf{e}_x \cdot (\mathbf{r} - \mathbf{r}')\Phi_{\mathrm{lr}}(|\mathbf{r} - \mathbf{r}'|) = L_y \int \mathrm{d}x \; f_{\mathrm{lr}}(h) + \mathrm{const.}$

(Monge representation). The interaction of a point on the liquid–vapour interface with the solid is obtained by integrating over the substrate area

$$f(h) = \int_{\mathrm{SL}} \mathrm{d}S' \; \tilde{f}(|\mathbf{r} - \mathbf{r}'|), \tag{5.6}$$

which for a homogeneous substrate only depends on the distance, $h$, due to symmetry. $f(h)$ is the effective integrated interaction between a point of the liquid–vapour interface with the homogeneous, planar substrate, and it is termed interface potential. In this special case, the free energy functional (5.5) takes the form

$$F[h] = \gamma_{\mathrm{SL}} L_y \int \mathrm{d}x \; + L_y \int \mathrm{d}x \sqrt{1 + (\partial_x h)^2} \, \Big[\gamma + f(h)\Big], \tag{5.7}$$

where $L_y$ denotes the system dimension parallel to the cylinder axis. In the limit that the equilibrium contact angle is small, one can adopt a long-wave approximation (or small-gradient expansion)

$$F[h] \approx \gamma_{\mathrm{SL}} L_y \int \mathrm{d}x \; + L_y \int \mathrm{d}x \, \Big[1 + \frac{1}{2} (\partial_x h)^2 + \cdots\Big] \, \Big[\gamma + f(h)\Big]. \tag{5.8}$$

It is important to note that, away from the droplet, there is a thin film of thickness $h_{\mathrm{min}}$ with a flat liquid–vapour interface (dewetted surface). $h_{\mathrm{min}}$ corresponds to the minimum of the interface potential. Eq. (5.8) yields for this dewetted part of the surface

$$F[h_{\mathrm{min}}] = L_y \int_{\substack{\mathrm{dew} \\ \mathrm{surf}}} \mathrm{d}x \, \Big[\gamma_{\mathrm{SL}} + \gamma + f(h_{\mathrm{min}})\Big] \equiv L_y \int_{\substack{\mathrm{dew} \\ \mathrm{surf}}} \mathrm{d}x \, \gamma_{\mathrm{SV}} \, . \tag{5.9}$$

Here, $\gamma_{\mathrm{SV}} = \gamma_{\mathrm{SL}} + \gamma + f(h_{\mathrm{min}})$ is the solid–vapour interface tension. We emphasize that it is not a solid-vacuum surface free energy per unit area, $F_0$, that is half of the work needed to cut the bonds of a solid of a unit cross section into two equal pieces in vacuum. Moreover, as long as the solid is not altered by the contact with the liquid or vapour, its free energy per unit area remains constant, $F_0 = \mathrm{const}$, and serves as the reference point for solid-liquid and liquid–vapour interface tensions. In our model of the solid we do not consider interactions between its constituents. Therefore, the work needed to cut the solid is zero and the reference value of the

surface free energy per unit area is $F_0 = 0$.

The equilibrium shape of the droplet is obtained by minimizing this free energy functional subject to the constraint of fixed droplet volume

$$V_{\text{drop}} = L_y \int \mathrm{d}x\; h(x) = \text{const} \tag{5.10}$$

yielding the condition

$$\pi(x) = -\frac{1}{L_y}\frac{\delta F}{\delta h(x)} = \lambda, \tag{5.11}$$

where $\lambda$ is a Lagrange multiplier constraining the droplet volume. Using Eq. (5.7) we obtain

$$\begin{aligned} \pi(x) &= -\sqrt{1+(\partial_x h)^2}\Big[\partial_h f\Big] + \partial_x\left(\frac{\partial_x h}{\sqrt{1+(\partial_x h)^2}}\Big[\gamma + f(h)\Big]\right) \\ &= \frac{\partial_{xx} h\Big[\gamma + f(h)\Big]}{\Big[1+(\partial_x h)^2\Big]^{3/2}} - \frac{\partial_h f}{\sqrt{1+(\partial_x h)^2}}. \end{aligned} \tag{5.12}$$

In the limit of small contact angles, $|\partial_x h| \ll 1$, this equation adopts the form

$$\pi(x) = \partial_{xx} h\Big[\gamma + f(h)\Big] - \partial_h f. \tag{5.13}$$

The pressure (5.12) consists of two contributions: (i) the curvature pressure, where $\kappa_{\text{full}} = \frac{\partial_{xx} h}{\left[1+(\partial_x h)^2\right]^{3/2}}$ is the curvature and $\gamma + f(h)$ is the effective tension of the interface a distance $h$ away from the solid substrate and (ii) the Derjaguin (or disjoining) pressure $\Pi(h) = -\partial_h f(h)$ that models wettability [39, 157]. The dimensionless ratio $f(h)/\gamma$ dictates the shape of a drop in the continuum model and it is this parameter that we will extract from the particle-based model in Sec. 5.3.

A spatially non-uniform pressure, $\pi(x)$, gives rise to a flow of liquid inside the film. As demonstrated in Chapter 2, using the Navier–Stokes equation and employing the long-wave approximation [114, 161, 162], one obtains

$$\partial_t h = -\partial_x \Gamma = -\partial_x\{Q(h)\partial_x \pi(x)\}, \tag{5.14}$$

where $Q(h) = h^3/3\eta$ is the mobility, $\eta$ is the dynamic viscosity of the liquid. Note, that $\Gamma$ is a flux that is written as the product of a mobility and a pressure gradient. For the case when one employs the small contact angles limit for $\pi$ (5.13), one recovers equation (2.34) which we previously employed in Chapters 3 and 4 for describing the evolution of the film thickness of the systems which we studied there, including additional physical effects.

The equation describing stationary solutions may either be obtained by directly minimizing the functional $F[h]$ according to Eq. (5.11), in the way it was done in Chapter 4, or, alternatively, one sets $\partial_t h = 0$ in Eq. (5.14) and integrates twice taking into account that $\Gamma = 0$ in the steady state, as in Chapter 3. Here we use the numerical continuation techniques [45], discussed earlier in Chapters 3 and 4, to solve the resulting ordinary differential equation as a boundary value problem on a domain of size $L$ with boundary conditions such that the center of the resulting drop solution is positioned on the right boundary ($x = 0$) and on the left boundary ($x = -L$) the profile approaches a precursor film. The volume is controlled by the integral condition, Eq. (5.10). Figure 5.2(a) presents typical drop profiles for various volumes whereas Fig. 5.2(b) gives the maximal drop height as a function of drop volume.

Note, that there exists a minimal droplet volume $V_{\mathrm{sn}}$ given by the saddle-node bifurcation in Fig. 5.2(b). If one decreases the volume below $V_{\mathrm{sn}}$, the droplet collapses, i.e., it changes discontinuously into a flat film. The transition is hysteretic (first order) as the primary bifurcation at $V_{\mathrm{c}}$ is subcritical. The situation is different for freely evaporating droplets when the chemical potential is controlled instead of volume. For a more detailed comparison of the two cases see Ref. [162].

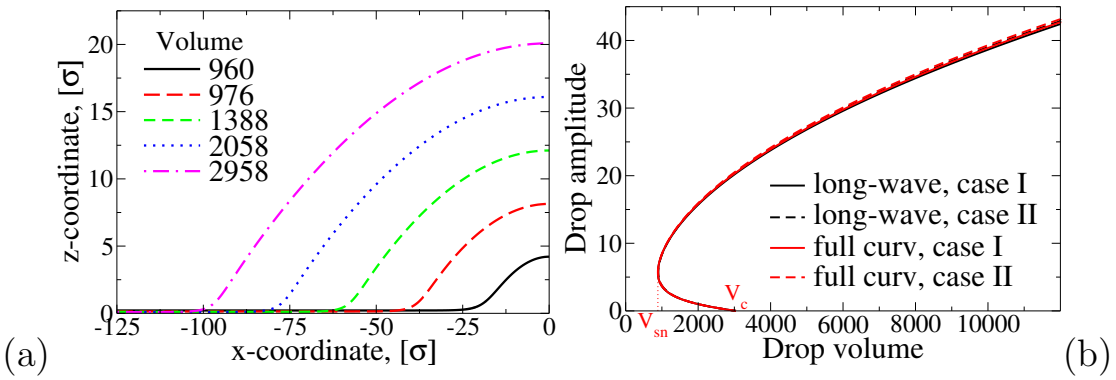


FIGURE 5.2: (a) Shown are selected half-profiles of droplets at volumes as given in the legend and (b) the bifurcation diagram presenting the drop height in dependence of the drop volume. Calculations are performed with (i) the full curvature, i.e., Eq. (5.11) with (5.12), and (ii) the long-wave curvature, i.e., Eq. (5.11) with (5.13). Case I and II refer to usage of only $\gamma$ or the full $\gamma+f(h)$ as prefactor of curvature, respectively. The profiles in panel (a) are obtained with case I for full curvature. The volume is controlled through appropriately adapting the Lagrange multiplier $\lambda$ at fixed domain size $L = 4000$. The employed disjoining pressure and interface tensions are extracted from MD simulations at $\epsilon_s = 0.81\epsilon$ (equivalent to an equilibrium contact angle of $\theta_E = 23.57^o$, for details see below section 5.4).

## 5.3 Parameter passing between particle-based model and continuum description

The particle-based model is defined in terms of pairwise interactions between beads, while the information that dictates the behavior of the continuum description is the liquid–vapour tension, $\gamma$, and the interface potential, $f(h)$. The latter quantifies the free-energy cost of locating the liquid–vapour interface a distance $h$ away from the solid substrate. Several strategies have been proposed to measure the interface potential in computer simulation of particle-based models: (i) The interaction between the interface and the substrate can be obtained in the grandcanonical ensemble, where the chemical potential $\mu$ controls the fluctuating thickness of the wetting layer of the liquid on the substrate. The probability, $P(h)$, of observing a wetting layer of thickness $h$ is related to the interface potential via $f(h) = -k_B T \ln P(h)+\text{const}$ [61, 94, 107, 108], where the choice of the constant ensures the boundary condition $f_{h\to\infty} = 0$. While being elegant, this computational technique is limited to simple models because the grandcanonical

ensemble requires the insertion and deletion of polymers and concomitant Monte-Carlo moves are only efficient for short polymers, low densities or in the vicinity of the liquid–vapour critical point. (ii) A negative curvature of the interface potential at a thickness $h$ signals the spontaneous instability of a wetting layer. From the characteristic length scale of this spinodal dewetting pattern one can deduce information about $\mathrm{d}^2 f(h)/\mathrm{d}h^2$ [146, 184]. (iii) Here we use the pressure tensor. This is a general technique that is not limited to short polymers or low densities. It does not require the implementation of particle insertion/deletion Monte-Carlo moves and can be straightforwardly implemented in standard Molecular Dynamics program packages.

### 5.3.1 Solid-liquid and liquid–vapour interface tensions

We study a supported polymer film as illustrated in Fig. 5.3 in the canonical ensemble. By virtue of the low vapour pressure of the polymer liquid, one can neglect evaporation effects. The flat liquid–vapour interface allows us to divide the system into thin parallel slabs (separated by the horizontal grey lines in Fig. 5.3), whose normal vector $\mathbf{n}$ is perpendicular to the substrate. All relevant quantities can then be averaged over each slab, resulting in fields that depend on the $z$-coordinate only.

In order to obtain the tension of the liquid–vapour and solid–liquid interfaces, $\gamma$ and $\gamma_{\mathrm{SL}}$, as well as the interface potential, $f(h)$, we consider a virtual change of the geometry of the simulation box such that the total volume $V$ remains unaltered. Using the scaling parameter $\lambda$, we relate the new linear dimensions, $L'_x, L'_y, L'_z$ of the simulation box to the original ones via $L'_x = \sqrt{\lambda} L_x$, $L'_y = \sqrt{\lambda} L_y$, $L'_z = \frac{1}{\lambda} L_z$. This scaling is the analog to the spreading of a droplet on a solid substrate. Thereby, only the liquid phase is subjected to this virtual change of the geometry but not the solid support. The value $\lambda < 1$ corresponds to a lateral squeezing of the liquid film on top of a solid substrate and a concomitant increase of the film thickness $h' = \frac{1}{\lambda} h$, where we have assumed that the liquid is incompressible. In the continuum model such a transformation gives rise to the following infinitesimal

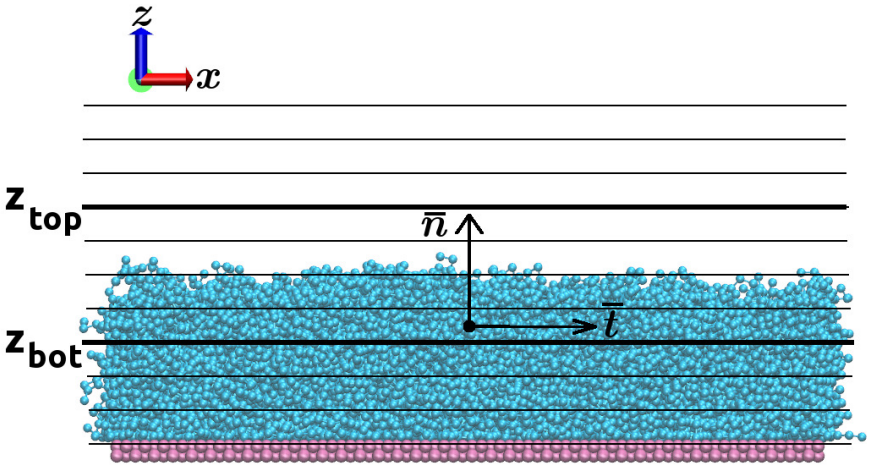


FIGURE 5.3: Sketch of the slab geometry used to calculate the liquid–vapour interface tension $\gamma$. The pressure tensor components $p_{\mathrm{n}}(z)$ and $p_{\mathrm{t}}(z)$ are calculated in every slab $k$ and then their difference is integrated across the interface.

change of the canonical free energy [38]

$$\left.\frac{\mathrm{d}F(\lambda)}{\mathrm{d}\lambda}\right|_{\lambda=1} = \left[\gamma_{\mathrm{SL}}+\gamma+f(h)\right]\left.\frac{\mathrm{d}L'_xL'_y}{\mathrm{d}\lambda}\right|_{\lambda=1} + \left.\frac{\mathrm{d}f(h)}{\mathrm{d}h}\frac{\mathrm{d}h'}{\mathrm{d}\lambda}\right|_{\lambda=1} L_xL_y \quad (5.15)$$

$$= \left[\gamma_{\mathrm{SL}}+\gamma+f(h)-\frac{\mathrm{d}f(h)}{\mathrm{d}h}h\right]L_xL_y, \quad (5.16)$$

where, contrary to the related works in grandcanonical ensemble [19, 63], we use the property of a canonical one and keep the number of particles in the liquid constant, i.e. constant volume $hL_xL_y = h'L'_xL'_y$ of the film

$$\frac{\mathrm{d}(L'_xL'_y)}{L'_xL'_y}+\frac{\mathrm{d}h'}{h'}=0. \quad (5.17)$$

This transformation procedure is described in detail in N. Tretyakov's thesis [179] and in [180]. We will use the final result, relating the local pressure (the free energy per unit area from 5.16) with the anisotropy of the pressure in the liquid and contributions due to the direct interaction between the liquid and the solid

substrate:

$$\gamma_{\text{film}}(h) \equiv \gamma_{\text{SL}} + \gamma + f(h) - \frac{\mathrm{d}f(h)}{\mathrm{d}h}h = \int \mathrm{d}z\ [p_{\text{n}}(z) - p_{\text{t}}(z)] \tag{5.18}$$
$$+\frac{1}{L_x L_y}\left\langle \sum_{s,i}\left[f^{\text{s}}_{z,is}z_{is} - \frac{1}{2}(f^{\text{s}}_{x,is}x_i + f^{\text{s}}_{y,is}y_i)\right] - \sum_{s_2,i} f^{\text{s}}_{z,is_2}\Delta z\right\rangle .$$

Here, $p_n(z)$ and $p_t(z)$ are the profiles of the normal and tangential pressure as a function of the slab position $z$. $\langle\cdots\rangle$ denote averages in the canonical ensemble and $f^s_{x,ij}$ denotes the $x$–component of the force acting between polymer beads $i$ and $j$. In the limit that the substrate is laterally homogeneous the terms involving the lateral forces between solid and liquid vanish.

We particularly stress that in the canonical ensemble the difference of the film tension $\gamma_{\text{film}}(h)$ and interface tensions $\gamma_{\text{SL}}$ and $\gamma$ is not the interface potential $f(h)$ [19, 63, 68], but of the form of Legendre transform $f(h) - h\frac{\mathrm{d}f(h)}{\mathrm{d}h}$.

In the absence of a solid substrate, the liquid is separated by a liquid–vapour interface from its coexisting vapour phase. In this special case, Eq. (5.18) simplifies and allows us to measure the liquid–vapour interface tension through the anisotropy of the pressure tensor components across the interface as [178, 182, 185]:

$$\gamma = \int_{z_{\text{top}}}^{z_{\text{bot}}} \mathrm{d}z\ [p_{\text{n}}(z) - p_{\text{t}}(z)]. \tag{5.19}$$

Here $z_{\text{top}}$ and $z_{\text{bot}}$ stand for the top and bottom limits of the solid–liquid interface.

We find $\gamma = 0.512 \pm 0.006\epsilon/\sigma^2$ which agrees well with previous calculations for similar systems [149]. Mechanical stability requires that the normal component of the pressure is constant throughout the system and equals the coexistence pressure [182]. Since the vapour pressure of a polymer melt is vanishingly small, $p_{\text{n}}(z) \approx 0$. We also note, that the anisotropy of the pressure is localized around the interface and, therefore, the integration can be restricted to an interval $[z_{\text{bot}}, z_{\text{top}}]$ around the interface.

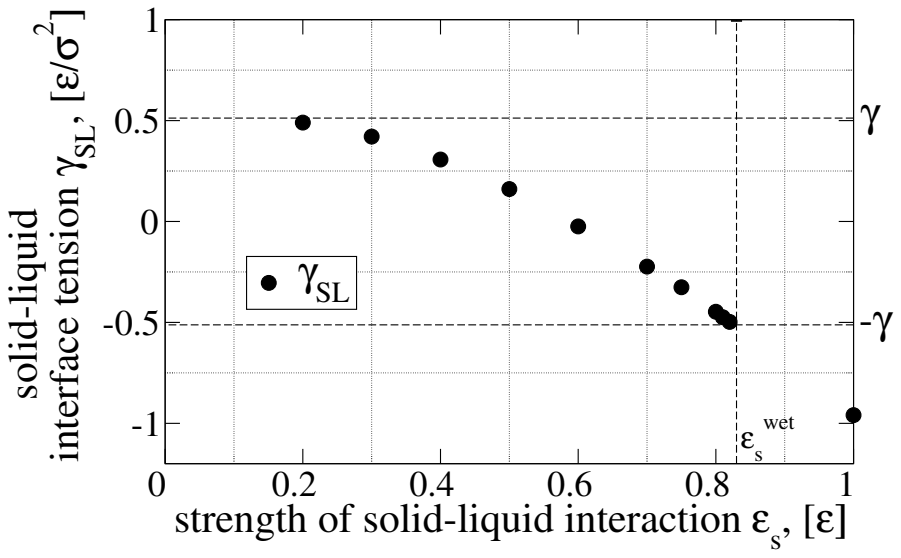


FIGURE 5.4: The dependence of solid-liquid interface tension $\gamma_{SL}$ on the strength of solid-liquid interaction $\epsilon_s$. The horizontal dashed lines represent the value of the liquid–vapour interface tension ($\gamma$) and the value of solid-liquid interface tension corresponding to the wetting transition (-$\gamma$). The wetting transition is localized at $\epsilon_s^{wet} \approx 0.83\epsilon$.

If we consider a liquid film in contact with the solid substrate, we can measure the solid-liquid interface tension $\gamma_{SL}$ according to Eq. (5.18) (provided that the thickness of the liquid film is sufficiently large to prevent the interaction of liquid–vapour and solid-liquid interfaces, i.e., $|f| \ll \gamma_{SL}$). Like in the case of the liquid–vapour interface, the anisotropy of the pressure, as well as the additional contribution due to the interaction between the liquid and the solid, are localized in a narrow region near the interface between the polymer liquid and the solid. The solid-liquid interface tension depends on the strength $\epsilon_s$ of the attractive interaction between solid and polymer liquid. The simulation results are presented in Fig. 5.4.

If the droplet on a substrate depicted in Fig. 5.1 is at equilibrium, one may describe the equilibrium of forces acting on its contact line by the macroscopic Young-Laplace equation (2.1) that relates the interface energies and the equilibrium contact angle $\theta_E$ [86, 193],

$$\gamma_{SL} + \gamma \cos\theta_E - \gamma_{SV} = 0. \tag{5.20}$$

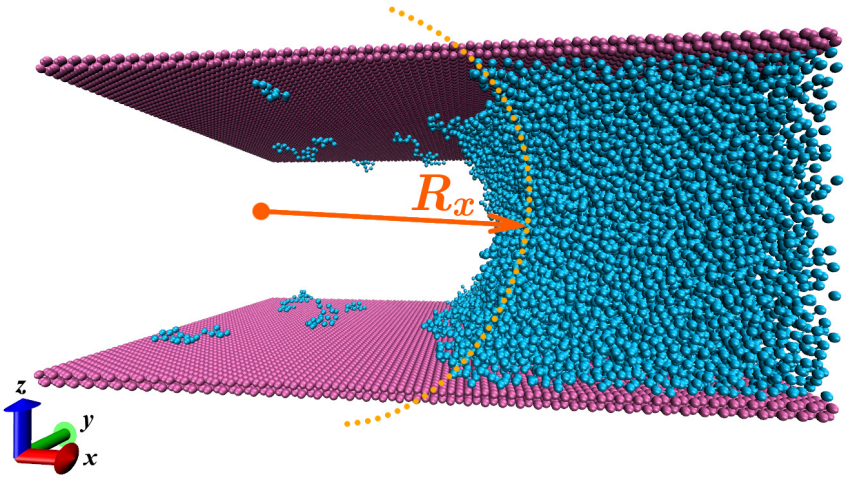


FIGURE 5.5: A part of a system used to determine solid–vapour interface tension $\gamma_{SV}$. The droplet serves as a reservoir to the chains adsorbed on the substrate. The yellow dotted line indicates the curvature of the liquid–vapour interface. The radius of curvature $R_x$ is indicated by the orange arrow.

Since the vapour pressure is vanishingly small for our polymer melt, we can neglect the interface tension between the solid substrate and the vapour phase, $\gamma_{SV} \approx 0$ to a first approximation. Using this approximation, we find that the wetting and drying transitions occur at $\gamma_{SL}(\epsilon_s) \approx -\gamma$ and $\gamma_{SL}(\epsilon_s) \approx \gamma$, respectively. From the data in Fig. 5.4 we locate the wetting transition at $\epsilon_s^{wet} \approx 0.83\epsilon$ and the contact angle reaches $180^o$ for small values of $\epsilon_s < 0.2\epsilon$.

### 5.3.2 Solid–vapour interface tension

While the approximation $\gamma_{SV} \approx 0$ is appropriate for small values of the strength of attractive solid-liquid interactions, $\epsilon_s$, the quality of this approximation deteriorates in the vicinity of the wetting transition. If the wetting transition were of second-order, the amount of liquid adsorbed onto the substrate, would continuously diverge as we approach the wetting transition. Even for a first-order wetting transition we expect that the adsorbed amount (i.e., the film thickness $h_{min}$ at which the interface potential exhibits a minimum) will increase when $\epsilon_s$ increases towards its transition value. In this case the approximation $\gamma_{SV} \approx 0$ becomes

| | $\epsilon_s = 0.75\epsilon$ | $\epsilon_s = 0.80\epsilon$ | $\epsilon_s = 0.81\epsilon$ | $\epsilon_s = 0.82\epsilon$ |
|---|---|---|---|---|
| $\gamma_{SV}$, $[\epsilon/\sigma^2]$ | 0 | – 0.00281 | – 0.00475 | – 0.00523 (– 0.01642) |
| $\gamma_{SL}$, $[\epsilon/\sigma^2]$ | – 0.32576 | – 0.44737 | – 0.47419 | – 0.49761 |
| $\theta_{E_0}$ (at $\gamma_{SV} = 0$), [degree] | 50.50 | 29.14 | 22.20 | 13.69 |
| $\theta_E$, [degree] | 50.50 | 29.77 | 23.57 | 15.98 (20.03) |

TABLE 5.1: Interface tensions of solid–vapour and solid-liquid interfaces and contact angles with ($\theta_E$) and without ($\theta_{E_0}$) taking the solid–vapour interface tension into account. For $\epsilon_s = 0.82\epsilon$ the value $\gamma_{SV}$ is affected by the finite value of $\Delta p$ and we provide in parentheses an alternative estimate of the contact angle.

unreliable and we employ a meniscus geometry as shown in Fig. 5.5 to extract the value of the solid–vapour tension.

The film thickness is chosen sufficiently large, such that the deviation of the pressure from its coexistence value, $\Delta p \sim -\frac{\gamma}{R_x+R_y}$, with $R_x$ and $R_y = \infty$ denoting the principle radii of curvature of the meniscus, has only a small influence on the adsorbed amount of polymer and $\gamma_{SV}$. Since $\Delta p < 0$, the adsorbed amount in the simulations will be smaller than at coexistence, $\gamma_{SV}$ will be too large (i.e., negative $\gamma_{SV}$ will have an absolute value that is too small), and we will slightly underestimate the contact angle, $\theta_E$. This correction to the deviation of the approximation $\gamma_{SV} \approx 0$, however, is insignificant for the used system size for all values of $\epsilon_s$ but the close vicinity of the wetting transition $\epsilon_s^{wet} \approx 0.83\epsilon$. Therefore, at $\epsilon_s = 0.82\epsilon$, we have used an alternative method as described in the following Sec. 5.3.3.

For the calculation of $\gamma_{SV}$ we used the same procedure as earlier for the solid-liquid interface tensions of a film, but the procedure is only applied to the part of the simulation box that is far away from the meniscus-forming liquid bridge. The values of $\gamma_{SV}$ and $\gamma_{SL}$ (for comparison) are presented in Table 5.1. One notices the increase in $\gamma_{SV}$ when the wetting transition is approached. However, compared to the influence on the solid-liquid interface tension the effect is small. Nevertheless, it becomes more important the closer one comes to the wetting transition, and the correction of the contact angles is significant when one compares profiles of drops of different sizes with the prediction of Eq. (5.20).

We compare the shape of drops obtained from the particle-based and continuum description in the vicinity of the wetting transition. In the following detailed

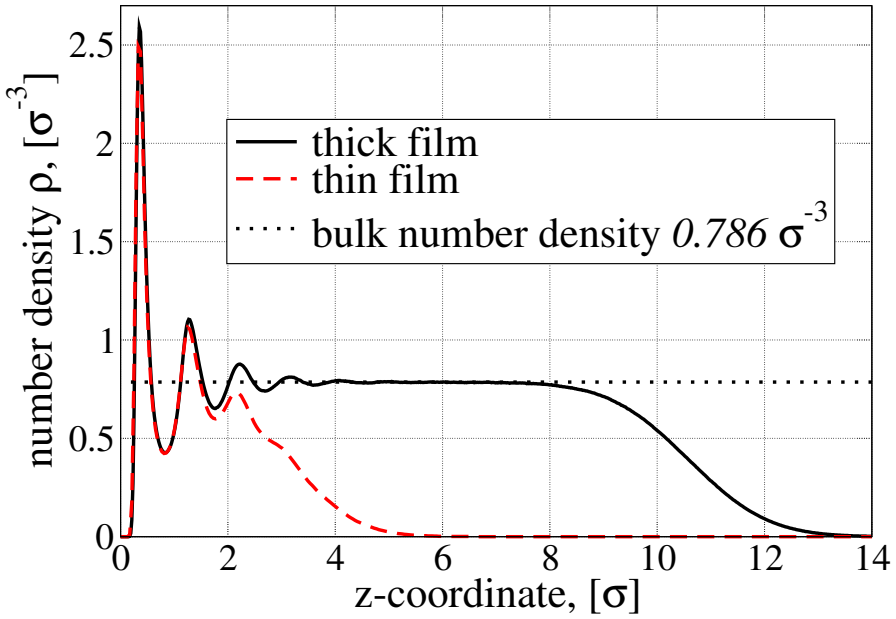


FIGURE 5.6: Density profiles of a polymer film at $\epsilon_s = 0.80\epsilon$. The solid black line represents a thick film with a bulk region separating solid-liquid and liquid–vapour interfaces. In the case of a thin film (dashed red line) it is no longer possible to distinguish the two interfaces. The dotted horizontal line indicates the coexistence number density.

comparison we employ the values $\epsilon_s = 0.75\epsilon$, $\epsilon_s = 0.80\epsilon$, and $\epsilon_s = 0.81\epsilon$ for the solid-liquid interaction strength that correspond to contact angles $\theta_E = 50.50^o$, $\theta_E = 29.77^o$, $\theta_E = 23.57^o$, respectively. For $\epsilon_s = 0.82\epsilon$, however, we will use the more accurate value, $\theta_E = 20.03^o$, extrapolated from the interface potential instead.

### 5.3.3 Interface potential and Derjaguin pressure

If we consider a polymer film on top of the solid substrate, Eq. (5.18) provides information about the solid-liquid and liquid–vapour interface tensions, $\gamma_{SL}$ and $\gamma$ as well as the interface potential, $f(h)$. For a thick film (cf. Fig. 5.6), the transitions in polymer density at the two interfaces are well separated, and the density at the center of the film approaches the bulk coexistence value. In this case, also the contributions to Eq. (5.18) that stem from the two interfaces can be well separated. The anisotropy of the pressure tensor at the solid substrate gives $\gamma_{SL}$, and the one at the liquid–vapour interface gives $\gamma$. Thus, the interface

potential vanishes, $f_{h\to\infty} \to 0$, indicating that the liquid–vapour interface will not interact with the substrate if the film is sufficiently thick.

However, upon decreasing the film thickness, the two interfaces start to interact and the contributions of the solid–liquid and liquid–vapour interfaces can not be separated anymore. The interaction between the interfaces is quantified by the interface potential, $f(h)$, or equivalently, by the Derjaguin pressure $\Pi(h) = -\frac{\mathrm{d}f(h)}{\mathrm{d}h}$. From Fig. 5.6 we observe that for small film thickness both interface density profiles are distorted, and the density does not reach its coexistence value at the center of the film. The distortion of the density profile far away from the interfaces is characterized by the bulk correlation length, $\xi_0$, which therefore sets the length scale of the interface potential [143].

Since we have determined $\gamma_{\mathrm{SL}}$ and $\gamma$ independently, we are able to extract the interface potential, $f(h)$, from the simulation data for thin films. To this end, we have to define the location of the liquid–vapour interface, i.e., the film thickness, $h$. There are several options: Either (i) one determines the position where the density equals a predefined value, typically the averaged density of the liquid and the vapour $(\rho_{\mathrm{liq}} + \rho_{\mathrm{vap}})/2$ (crossing criterion) or (ii) one defines the film thickness via the adsorbed excess (Gibbs dividing surface),

$$\Delta\Gamma_{\mathrm{ads}} = L_x L_y \int \mathrm{d}z \; [\rho(z) - \rho_{\mathrm{vap}}] \equiv [\rho_{\mathrm{liq}} - \rho_{\mathrm{vap}}] \, L_x L_y h. \tag{5.21}$$

In this work we adopt the integral criterion (5.21) to define the film thickness. Neglecting the vanishingly small vapour density at coexistence, we obtain

$$h_{\mathrm{eff}} = \frac{N_{\mathrm{mon}}}{\rho_{\mathrm{liq}} A_{\mathrm{film}}}, \tag{5.22}$$

where $N_{\mathrm{mon}}$ is the number of monomers of the liquid inside the simulation box and $A_{\mathrm{film}} = L_x L_y$ is the area of the substrate underneath the film.

We note that both definitions become problematic for film thicknesses where the curvature of the interface potential is negative, $\frac{\mathrm{d}^2 f}{\mathrm{d}h^2} < 0$. In this regime of film

thicknesses a laterally extended, homogeneous film becomes unstable with respect to spinodal dewetting [100, 162, 184]. However, even in this film thickness region, the films can be linearly or even absolutely stable if the lateral extension of the simulation box is sufficiently small. The related critical values depend on film thickness [174, see, e.g., Fig.8 of]. In the simulation, we can still obtain meaningful data for the interface potential if we restrict the lateral system size to be smaller than the characteristic wavelength of the spontaneous rupture process.

Additionally, we mention that the liquid–vapour interface in the Molecular Dynamics simulations exhibits local fluctuation of its height (i.e., capillary waves), and the Gibbs dividing surface measures the laterally averaged film thickness. The interaction of the liquid–vapour interface with the substrate imparts a lateral correlation length, $\xi_{\parallel} = 2\pi\sqrt{\gamma/\frac{\mathrm{d}^2 f}{\mathrm{d}h^2}}$, onto these interface fluctuations. These fluctuations give rise to a weak dependence of the interface potential on the lateral system size for $L_x, L_y < \xi_{\parallel}$, i.e., the interface potential is renormalized by interface fluctuations. Qualitatively, the effect of fluctuations is to extend the range of the potential, i.e., $\xi = \xi_0(1 + \omega/2)$ with $\omega = \frac{k_\mathrm{B}T}{4\pi\xi_0^2\gamma}$ [92].

The interface potential exhibits a minimum at small film thickness, $h_{\min}$. This film thickness characterises the amount of liquid adsorbed on the substrate in contact with the vapour. As illustrated in Sec. 5.3.2 $\gamma_{\mathrm{SV}} = 0$ and therefore no chains are adsorbed on the substrate except for the close vicinity of the wetting transition. The free energy of such a vanishingly thin polymer film is given by $\gamma_{\mathrm{film}}(h_{\min}) = \gamma_{\mathrm{SL}} + \gamma + f(h_{\min}) = \gamma_{\mathrm{SV}}$. Thus, the measurement of the different tensions for a planar polymer film provides the value of $f(h_{\min})$.

Alternatively, we can use the measured value $f(h_{\min})$, in turn, to estimate the solid–vapour tension, $\gamma_{\mathrm{SV}}$. We have employed this strategy for $\epsilon_{\mathrm{s}} = 0.82\epsilon$, where the finite curvature of the meniscus result in a relevant deviation of the pressure from its coexistence value. Extrapolating the simulation data to the thickness $h_{\min} \approx 0$ we obtain $\gamma_{\mathrm{SV}} = -0.01642$. We will use this more accurate value, which is not affected by the curvature of the meniscus and that is compatible with the interface potential, in the comparison with the continuum model in Sec. 5.4.

Since Eq. (5.18) only provides the Legendre transformation of the interface potential and we require an analytical expression for the continuum model, we make an Ansatz for the functional form of $f(h)$. Generally, one can distinguish between short-range and long-range contributions to the interface potential [43, 143]. The long-range contribution results from dispersion forces between the liquid and the substrate. In our particle-based model, however, we consider only the short-range part as our LJ interaction (5.2) is cut off at $r_c$. Thus, there is no long-range contribution in our model in contrast to previous works, when an effective long-range contribution was taken into account despite finite interaction cut off [19, 63]. The short-range contribution to $f(h)$ stems from the distortion of the interface profile due to the nearby presence of the solid substrate as illustrated in Fig. 5.6, and it is typically expanded in a series of exponentials [43, 143]

$$f_{\mathrm{sr}}(h) = a\mathrm{e}^{-h/\xi} - b\mathrm{e}^{-2h/\xi} + c\mathrm{e}^{-3h/\xi} - d\mathrm{e}^{-4h/\xi} + \dots \tag{5.23}$$

In order to obtain $f(h)$ in practice, we fit its Legendre transform $f(h) - h\frac{\mathrm{d}f}{\mathrm{d}h}$ by a sum of four exponential terms like in Eq. (5.23), and enforce that the interface potential exhibits a minimum at $h_{\mathrm{min}} \approx 0$ (there is no precursor film in our MD model) with a value $f(h_{\mathrm{min}})$, as obtained by the measurement of the interface tensions. The resulting fits for $f(h)$ at $\epsilon_{\mathrm{s}} = 0.75\epsilon, 0.80\epsilon, 0.81\epsilon$ and $0.82\epsilon$ are given as solid lines in Figs. 5.7 (a)-(d). The parameters of the fits are presented in Table 5.2.

| Parameter | $\epsilon_{\mathrm{s}} = 0.75\epsilon$ | $\epsilon_{\mathrm{s}} = 0.80\epsilon$ | $\epsilon_{\mathrm{s}} = 0.81\epsilon$ | $\epsilon_{\mathrm{s}} = 0.82\epsilon$ |
|---|---|---|---|---|
| $a, [\epsilon/\sigma^2]$ | 0.13191 | 0.06485 | 0.05057 | 0.06132 |
| $b, [\epsilon/\sigma^2]$ | 1.40871 | 0.58700 | 0.41256 | 0.36875 |
| $c, [\epsilon/\sigma^2]$ | 1.67606 | 0.70902 | 0.50249 | 0.42963 |
| $d, [\epsilon/\sigma^2]$ | 0.58566 | 0.25447 | 0.18323 | 0.15318 |
| $\xi, [\sigma]$ | 1.51770 | 1.26964 | 1.14735 | 1.00512 |

TABLE 5.2: Parameters of the fitting curves of $f(h)$ for the case where the first four terms of the short-range contributions [Eq. (5.23)] are taken into account. Note, that only three parameters are independent since there are two additional constraints: The local minimum criterion at $h \approx 0\sigma$ implies $d = (a - 2b + c)/4$ and the Young-Dupré relation (5.24) dictates the value $f_{\mathrm{min}}$ by setting $b = a + c - d - f_{\mathrm{min}} = 1.5a + 0.5c - 2f_{\mathrm{min}}$.

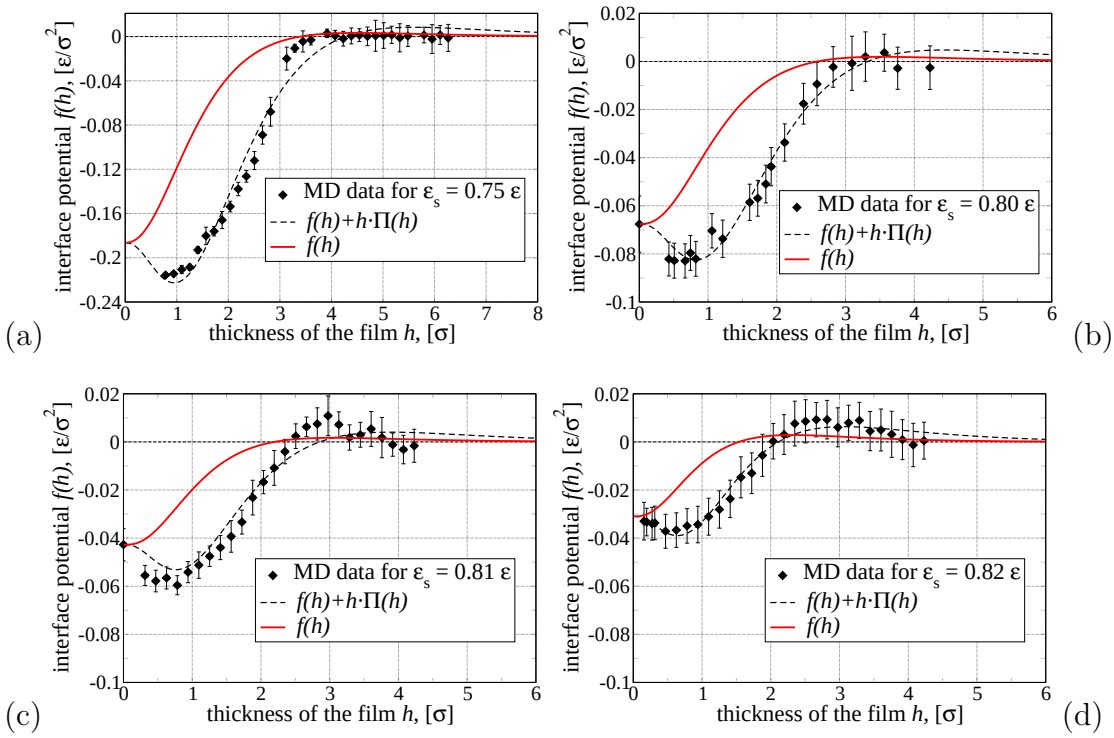


FIGURE 5.7: Panels (a), (b), (c) and (d) give the interface potential $f(h)$ at $\epsilon_s = 0.75\epsilon$, $\epsilon_s = 0.80\epsilon$, $\epsilon_s = 0.81\epsilon$ and $\epsilon_s = 0.82\epsilon$, respectively. They are obtained by fitting the MD results for the tension $\gamma_{film}(h) - \gamma - \gamma_{SL}$ of films of various small thicknesses (black symbols with error bars) by the expression $f(h)+h\Pi(h)$ (dashed black line) obtained employing the first four terms of the short-range part of the interface potential $f_{sr}(h)$. The resulting interface potential $f(h)$ is given as solid red line. Note, that the minimal value of $f_{min}$ is always reached at vanishingly small thicknesses $h \approx 0\sigma$, as there is no precursor film in our MD model.

Using the macroscopic Young-Dupré relation, one observes that value of the minimum of $f(h)$ dictates the contact angle [38]

$$f(h_{min}) = \gamma(\cos\theta_E - 1). \tag{5.24}$$

Much more information can be extracted from the interface potential: (i) The shape of the interface potential controls deviations of the drop shape from a spherical cap in the vicinity of the wetting transition. (ii) Within the square-gradient approximation the integral of $\sqrt{f(h)}$ is related to the line tension at the three-phase contact line [56, 73, 111, 144]. For all values of $\epsilon_s$ investigated in the particle-based model, the line tension is expected to be negative. (iii) The observation that $f(h)$ increases above zero at intermediate values of $h$ indicates that

the wetting transition is of first-order.

## 5.4 Static case - Sitting droplets

In the following we will compare the shape of droplets obtained from the particle-based model and the continuum description. This comparison focuses on droplets with small contact angles $\leq 50^{\circ}$ obtained in the particle-based model for strengths of solid-liquid interaction close to the wetting transition ($\epsilon_s = 0.75\epsilon$ to $0.82\epsilon$). Different numbers of polymer chains are used to create cylindrical 2d droplets (3d ridges) of varying volumes and hence heights. Data are sampled with a frequency of 4000 MD steps. This time interval between two samples corresponds to the Rouse relaxation time for a similar polymer liquid $\tau_R = 25.6 \pm 5\,\tau$ [149]. For small droplets (up to 600 chains) the sampling lasted $2 \times 10^6$ steps, whereas for bigger ones (up to 9600 chains) this interval was increased up to $10^7$ steps, because large fluctuations of the droplet shape occur. As a result, every density profile is obtained by averaging over 500 (small drops) to 2500 (large drops) snapshots. To extract the droplet shape and measure the contact angle, we use a set of density profiles obtained in 10 independent runs. In total, all large droplets are simulated over $10^8$ steps.

The resulting cylindrical droplet snapshots are cut into slices along the invariant $y$-direction. In every slice the two-dimensional $(x, z)$ density map is created with respect to the center-of-mass of the droplet cut. An average over these maps results in the average number density profile in the $(x, z)$ plane. A two-dimensional drop profile is extracted by localizing the solid-liquid and liquid–vapour interfaces by the crossing criterion for the density as $\rho_{\text{int}} = (\rho_{\text{liq}} + \rho_{\text{vap}})/2$. Examples of profiles are presented in Fig. 5.8. The resulting profiles are then compared to the ones extracted from the employed continuum models, which are also presented in Fig. 5.8.

One popular characteristic of the drop shape is the contact angle, because it is related to the balance of interface tensions at the three-phase contact line of a

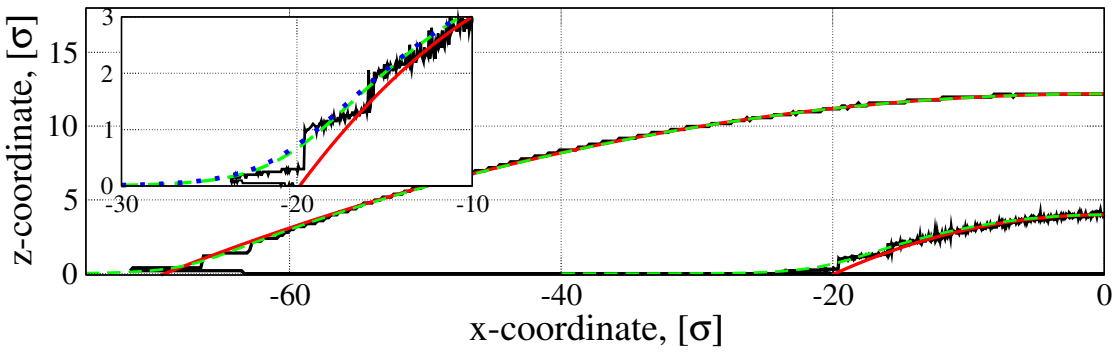


FIGURE 5.8: Profiles of two-dimensional droplets obtained by cutting cylindrical droplets obtained in MD simulations [solid noisy black line] for the case $\epsilon_s = 0.82\epsilon$ for two values of $h_{max}$ ($4.046\sigma$ and $12.181\sigma$). The corresponding spherical cap fit is given as solid smooth red line. The MD drops are compared with results of the continuum model Eq. (5.11) with the full curvature [Eq. (5.12)] and in long-wave approximation [Eq. (5.13)] that are given as dashed green and dotted blue lines, respectively. The inset shows a zoom into the three-phase contact line region of the smaller droplet.

macroscopic drop. For finite-sized drops, however, the contact angle is not uniquely defined: (i) One may define a *mesoscopic contact angle* $\theta_{mes}$ as the slope at the inflection point of the droplet profile, as it was done in Chapter 3 for $\theta_{app}$ [173, 177]. However, the steepest slope obtained in this way may not coincide with the (larger) macroscopic contact angle even in the limit of large drop size [152]. This corresponds to the distinction of macroscopic and microscopic contact angle in Ref. [156]. Moreover, in the particle-based model, the inflection point may be located very close to the three-phase contact line where liquid-like layering effects of the particle fluid [2] may occur and affect the drop profile[3]. (ii) Alternatively, one may define a *spherical cap contact angle* by approximating the drop profile by a spherical cap profile with a minimal radius of curvature $R = -1/\kappa$, i.e., using the curvature at $h_{max}$. The resulting contact angle is $\theta_{sph} = \arccos(1 - h_{max}/R)$[4].

[2]The layering visible in Fig. 5.8 and the MD-simulated droplets presented further corresponds to density variations in the interface region. The effective bead size sets the intrinsic scale of packing and layering in the fluid [179].

[3]Similar extrapolation schemes, like defining a contact angle via the steepest slope of the liquid–vapour interface or the local extrapolation of the droplet shape towards the contact line, have been explored for the particle-based model but did not give reliable results for the contact angle.

[4]There are different strategies of measuring the contact angle with the spherical cap approximation: direct geometric measurements [16, 95], estimation from the center of mass position [149] or from the volume of the droplet. In our MD simulations, we define a contact angle by the geometrical method. Other methods give a similar result as all of them assume the spherical shape of the droplet.

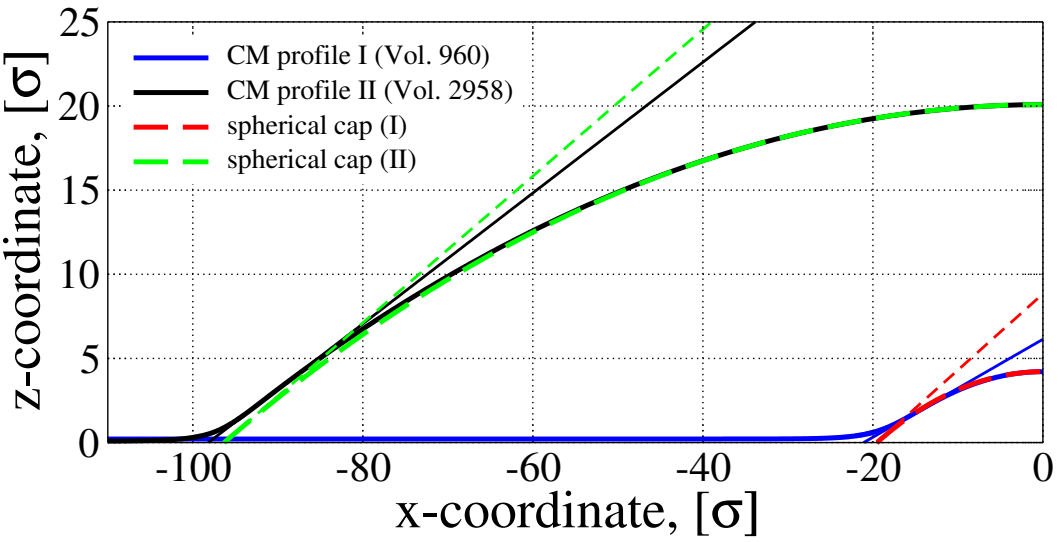


FIGURE 5.9: Droplet profiles as obtained from continuum theory with full curvature (heavy solid lines) for $\epsilon_s = 0.81\epsilon$ and drop height (a) $H = 4$ and (b) $H = 20$. Also shown are the spherical caps as obtained from the curvature at the drop maxima (heavy dashed lines), and the tangent lines at the point of the steepest slope of the profile (thin solid line), and the tangent line of the spherical cap profile at precursor height (thin dashed line). Drop height $H$ is defined as difference of height at maximum and precursor height.

In the profiles extracted from the particle-based model, we extract $\theta_{\text{sph}}$ by only considering the central part of the drop to define the curvature. In this way, the calculation is not perturbed by liquid-like layering effects or by the short-range interface potential that distorts the liquid-gas interface close to the three-phase contact line. The height of the drop is determined as the difference of the highest point of the spherical cap and the position of the solid-liquid interface. $\theta_{\text{sph}}$ converges to the proper macroscopic contact angle in the limit of large drop size, but may misrepresent the shape and volume of small droplets.

For the continuum model, the two angles $\theta_{\text{sph}}$ and $\theta_{\text{mes}}$ are illustrated in Fig. 5.9 that shows two droplet profiles $h(x)$ as obtained from Eqs. (5.11) with (5.12), their approximated spherical cap profiles and the tangents of $h(x)$ at the point of steepest slope (giving $\theta_{\text{mes}}$) and of the spherical cap profile at the point where it crosses the precursor height (giving $\theta_{\text{sph}}$). One clearly notes that the two measures differ, and that the difference decreases with increasing droplet size. We will see below that the two measures do not converge even for very large drops. In the following we focus on the spherical cap contact angle $\theta_{\text{sph}}$.

The resulting contact angles for drops of various sizes are presented for different $\epsilon_s$ as open square symbols in Fig. 5.10. Overall, they agree well with the prediction of Eq. (5.20) that is given as horizontal dashed black line (with the standard deviation indicated as a grey hatched region). Corresponding results for the contact angle obtained from the continuum model, employing the long-wave approximation for the curvature, Eq. (5.13), and with the full curvature, Eq. (5.12), are given as well. The results for both are shown as solid (case I) and dashed (case II) lines of different colors depending on the angle shown ($\theta_{\mathrm{mes}}$ or $\theta_{\mathrm{sph}}$) and the curvature used. Note that both curvature models result in identical results for $\theta_{\mathrm{sph}}$ because $\partial_x h = 0$ at the apex of the drop. This is not the case for $\theta_{\mathrm{mes}}$. Case I and II refer to the usage of only $\gamma$ or the full $\gamma + f(h)$ as prefactor of curvature, respectively [cf. Eqs. (5.13) and (5.12)].

The angle $\theta_{\mathrm{sph}}$ obtained in the continuum approach agrees well with the result of the MD simulations. This is particularly true for case I (only $\gamma$ as prefactor of curvature) where $\theta_{\mathrm{sph}}$ converges for large drops to the value obtained with the Young-Laplace equation. The deviations of case II from case I are small over the entire thickness range for $\epsilon_s = 0.82\epsilon$, $\epsilon_s = 0.81\epsilon$ and $\epsilon_s = 0.80\epsilon$, but rather large for $\epsilon_s = 0.75\epsilon$. Note, that $\theta_{\mathrm{mes}}$ does not agree well with the macroscopic angle obtained in the MD simulations. In long-wave approximation it is always at least some percent smaller than $\theta_{\mathrm{sph}}$ (more so for small droplets). The angle $\theta_{\mathrm{mes}}$ obtained with the full curvature differs less from $\theta_{\mathrm{sph}}$, the difference becomes less than one percent for large drops. For both curvature models, $\theta_{\mathrm{mes}}$ always decreases monotonically with decreasing drop size. All these statements apply for the respective relation between the various curves in case I equally as in case II. The various angles calculated in case I are always slightly below the ones obtained in case II.

Inspecting Fig. 5.10, one notes a number of further details that warrant to be highlighted: (i) A common feature of the particle-based model for $\epsilon_s \geq 0.80\epsilon$, shown in Figs. 5.10 (b)-(d), is the overshooting of the values of contact angles at thicknesses $h \approx 3 - 7\sigma$. This effect can also be observed in the spherical cap contact angle obtained from the continuum models. It indicates that the product of drop height

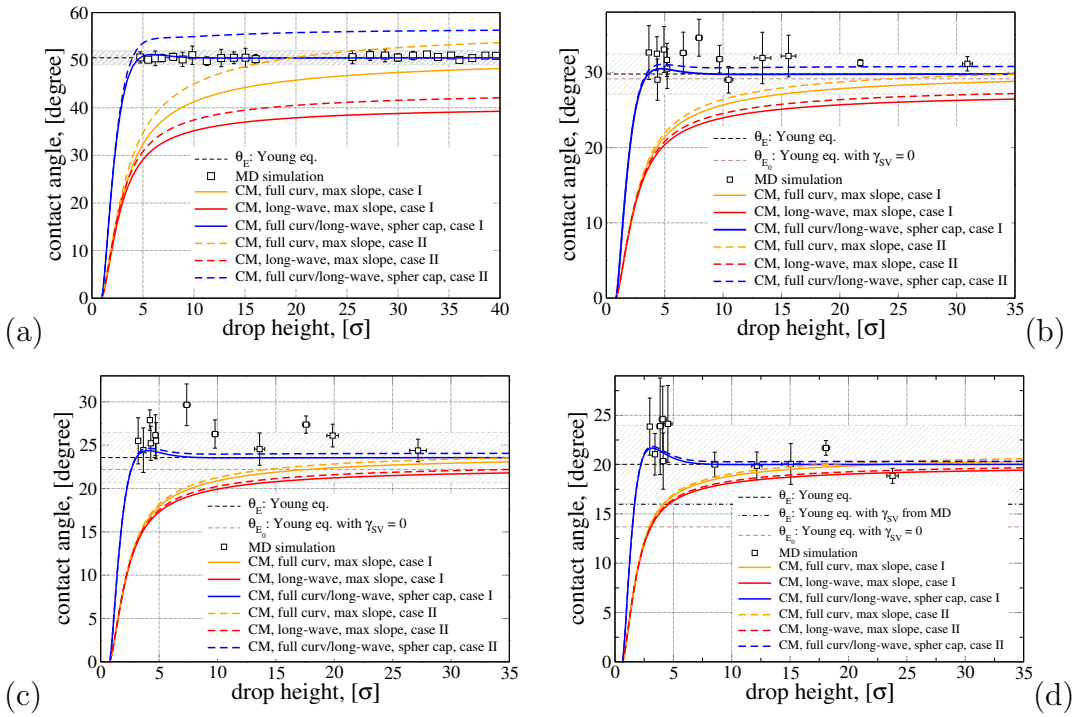


FIGURE 5.10: Contact angles $\theta$ of droplets of different sizes as a function of droplet height. Panels (a), (b), (c) and (d) give results at solid-liquid interaction strengths of $\epsilon_s = 0.75\epsilon$, $\epsilon_s = 0.80\epsilon$, $\epsilon_s = 0.81\epsilon$ and $\epsilon_s = 0.82\epsilon$, respectively. Square symbols correspond to the contact angle measured in MD using a spherical cap approximation of the droplet profile. Dotted and dashed thin horizontal lines correspond to the values $\theta_{E_0}$ and $\theta_E$ obtained from the Young equation with and without accounting for the measured solid–vapour interface tension $\gamma_{SV}$, respectively. Hashed zones show the standard deviation of $\theta_E$. Panel (d) shows additionally as a dot-dashed horizontal line the value of $\theta_E$ as extracted from the meniscus geometry. Case I and II refer to usage of only $\gamma$ or the full $\gamma + f(h)$ as prefactor of the curvature, respectively. The thick solid and dashed curves (orange, red and blue) in panels (a) to (d) give the mesoscopic steepest slope contact angle $\theta_{mes}$ obtained from the continuum model with full and long-wave curvature [Eq. (5.11) with Eqs. (5.12) or (5.13)] and the spherical cap contact angle $\theta_{sph}$, respectively. In the last case, full and long-wave curvatures give the same result (see main text for details).

$h_{max}$ and curvature at the drop apex $\kappa_{max}$ is not a constant any more, instead $|h_{max}\kappa_{max}|$ first increases with increasing volume (before decreasing again). (ii) Another detail one notices is the importance of the solid–vapour interface tension, $\gamma_{SV}$, measured in Sec 5.3.2. At $\epsilon_s = 0.75\epsilon$ it equals zero and at $\epsilon_s = 0.80\epsilon$ the macroscopic contact angles are almost the same if one neglects $\gamma_{SV}$ or properly accounts for it (cf. the dotted and dashed horizontal lines in Fig. 5.10(b), respectively). However, the difference between the two approaches becomes increasingly important with increasing $\epsilon_s$, i.e. decreasing contact angle (Figs. 5.10 (c) and (d)).

Taking a non-zero $\gamma_{SV}$ into account becomes crucial close to the wetting transition. There, for rather small values of the contact angle (about $15 - 20^{o}$) the difference is of the order of $20 - 40\%$ and accounts for $2 - 6^{o}$. The difference can lead to an incorrect prediction of the contact angle if one assumes $\gamma_{SV} = 0$ in the particle-based model.

Finally, we note that the error bars of the contact angles $\theta$ measured in MD using a spherical cap approximation of the droplet profile (open squares in Figs. 5.10(a) to 5.10(d)) are quite large. They increase with decreasing contact angle even in absolute terms. Several possible explanations exist for this behavior: (i) In the vicinity of the wetting transition, there are strong capillary waves on the surface of the droplet (particularly close to the three phase contact line) [3]. (ii) The crossing criterion we apply to define the profile of the drops $(\rho_0 + \rho_V)/2$ is not a unique choice. There are other possibilities to define the local interface position based, e.g., on 10-90% or 20-80% rules (cf. [6, 64, 137]).

Next, we compare the drop profiles as obtained from the particle-based model and the continuum description. For the case of a rather small contact angle, $\epsilon_s = 0.82\epsilon$, Fig. 5.8 gives results for a very small droplet of $h_{max} = 4.046\sigma$ and a larger one with $h_{max} = 12.181\sigma$. The layering effects of the particle-based model are rather independent of droplet size. Obviously, the layering of the particle-based model is not captured by the continuum model, however, its predictions go smoothly through the steps of the profile and always lay between the lateral end points of the steps. At the center of the drop, the spherical-cap fit to the particle-based model and the continuum results, obtained with Eq. (5.11) with the full curvature (Eq. (5.12)) as well as in long-wave approximation (Eq. (5.13)), nicely agree with each other. As cases I and II can not be distinguished by eye alone we have only included case I.

Differences between long-wave and full curvature and the results of the particle-based model are only visible in the contact line region. There, the spherical cap is not a good fit to the particle-based model. The two continuum models nearly coincide, implying that the long-wave approximation for static droplets is still

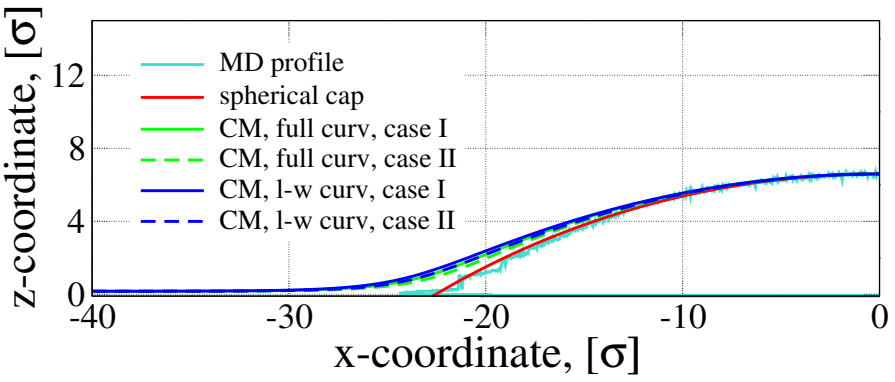


(a)

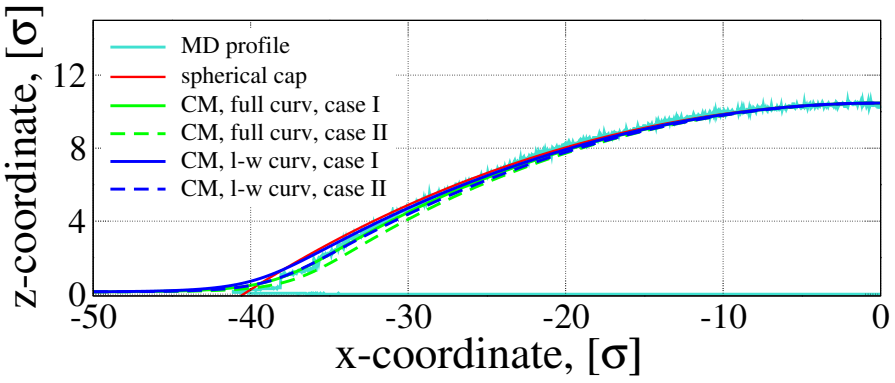


(b)

FIGURE 5.11: Droplet profiles obtained in MD simulations and with continuum models are compared for the case $\epsilon_s = 0.80\epsilon$, apex heights (a) $h_{max} = 6.594\sigma$ and (b) $h_{max} = 10.469\sigma$. The solid light blue curves give the liquid–vapour interface as obtained in the MD simulation, while the solid red curves give the corresponding spherical cap fit. Results of the continuum model (CM) Eq. (5.11) with the full curvature (Eq. (5.12) - green curves) and in long-wave approximation (Eq. (5.13) - dark blue curves) are shown for cases I and II as solid and dashed lines, respectively. For details see main text.

very good for contact angles around 20°. In the contact line region, they seem to represent a better approximation to the particle-based model than the spherical cap. One should actually expect this, as the continuum models incorporate the Derjaguin pressure as measured in the particle-based model. One may conclude that within its limitations the continuum model describes the profiles rather well if it incorporates the interface tensions and Derjaguin pressure from particle-based model.

The situation differs for larger contact angles as obtained for $\epsilon_s = 0.80\epsilon$ and shown in Fig. 5.11: (i) The deviation from the spherical-cap approximation is more significant than for the smaller contact angle and (ii) the continuum model

fails to describe the simulation data for the smaller droplet size. The difference between the predictions of the different versions of the continuum description is small compared to the deviation between the continuum models and the particle-based model. Therefore, the reason of the discrepancy is not rooted in the different approximations of the curvature.

We note that interface fluctuations in a small droplet are strongly suppressed. Therefore, one should rather use the bare interface potential (i.e., interface potential without accounting of capillary waves that could be obtained from a thin film with very reduced lateral dimensions) than the one deduced from a laterally extended film. Since the bare interface potential has a smaller range than the renormalized one [92] that accounts for thermal fluctuations of the liquid–vapour interface (i.e., capillary waves), we expect the profile of a small droplet to be better approximated by a spherical-cap shape than that of a large one, which is indeed consistent with the simulation data.

For the same reason, the predictions of the continuum model are more accurate for the larger drop than for the smaller one because it uses the renormalized interface potential as input. This rational explains why the predictions of the continuum model systematically deviate from the results of the particle-based model for small droplet size. For the large droplet, in contrast, the continuum model succeeds in describing the deviations from the spherical cap shape, which is larger for small contact angles. The profile of the particle-based model lies right in the middle of the predictions of the continuum models. The one that fits best is the case I with full curvature. Therefore, we conclude that even for contact angles of about $30^{\circ}$ all models agree fairly well with the particle-based simulations provided the appropriate interface potential is used.

Finally, we compare the profiles with a rather large contact angle as obtained for $\epsilon_{\mathrm{s}} = 0.75\epsilon$ and shown in Fig. 5.12. For comparison we use a large droplet with $h_{\max} = 25.494\sigma$. The difference between the various versions of the continuum models is clearly seen not only at the contact line but over the entire droplet profile. The best agreement with the particle-based model is achieved for case

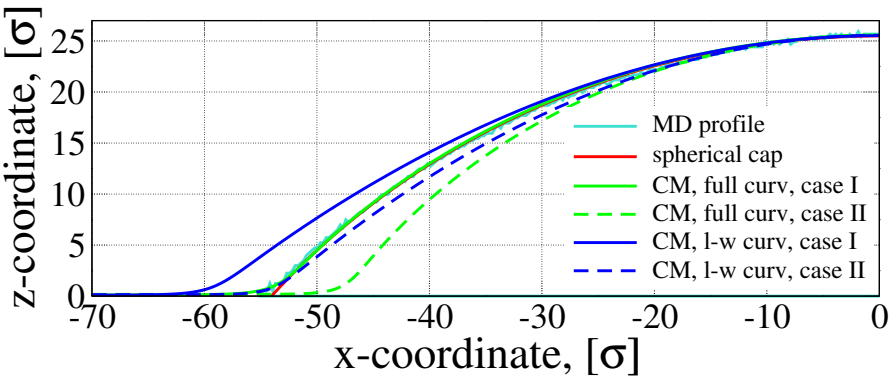


FIGURE 5.12: Droplet profiles obtained in MD simulations and with continuum models are compared for the case $\epsilon_s = 0.75\epsilon$ and apex height $h_{max} = 25.494\sigma$. The solid light blue curve gives the liquid–vapour interface as obtained in the MD simulation, while the solid red curve gives the corresponding spherical cap fit. Results of the continuum model (CM) Eq. (5.11) with the full curvature (Eq. (5.12) - green curves) and in long-wave approximation (Eq. (5.13) - dark blue curves) are shown for cases I and II as solid and dashed lines, respectively. For details see main text.

I with full curvature; all other versions differ more significantly. Therefore, we conclude that for contact angles of about 50° only the model with full curvature agrees well with the particle-based model, while the long-wave approximation is not valid anymore. It is not advisable to apply at $\theta_E = 50°$ where it predicts a contact angle $\theta_{mes}$ that is 20% lower.

## 5.5 Conclusions

The equilibrium properties of polymer droplets have been studied by Molecular Dynamics simulation of a coarse-grained particle-based model and a continuum description in terms of an effective interface Hamiltonian. We have devised a simple method to compute the interface potential for laterally corrugated substrates, which is based on the anisotropy of the pressure inside the film. This general computational strategy can be applied to dense liquids of large macromolecules and can be implemented in standard Molecular Dynamics programs. Using the so-determined interface tensions and the interface potential in the continuum model, we find quantitative agreement between both descriptions if (i) the full curvature

is used in the continuum model for large contact angles and (ii) the size of the drop is larger than the lateral correlation length, $\xi_{\parallel}$, of interface fluctuations. We also find that for contact angles up to about 30 degree the long-wave approximation that is normally used in thin film models describes the droplet shapes even quantitatively quite well.

These results demonstrate that the tensions and the interface potential capture the relevant information that needs to be passed on to a continuum model to describe the equilibrium shape of droplets, including the deviations from the spherical cap shape in the vicinity of the three-phase contact line.

# Chapter 6

# Conclusions and outlook

This thesis covers three projects with the common purpose of exploring the influence of wettability and capillarity on the statics and dynamics of thin liquid films and small drops. The theoretical approach we have chosen to study these types of systems is based on the lubrication approximation. This final chapter summarises the main conclusions of the Thesis, discusses their implications and possible directions for future research.

In Chapter 2 we have introduced the main concepts of capillarity and wettability and the general thin film theory. This theory is developed to describe geometries for which the velocities parallel to the substrate are much larger than the orthogonal ones and due to continuity the latter implies the gradients orthogonal to the substrate are much larger than the parallel ones. These assumptions give rise to the lubrication approximation which significantly simplifies the governing equations. Combining this with a kinematic boundary condition for the free surface serving to guarantee that the material boundary moves with the velocity of the liquid at the boundary, we have demonstrated the derivation of the evolution equation for the film thickness.

Having in mind the idea of developing the thin film theory further to suit the case of complex liquids, we have introduced the standard hydrodynamic formulation for solutions and suspensions and have shown how it can be reformulated as a

gradient dynamics based on an underlying free energy functional. We have discussed the adaptability of this formulation towards various physical effects which it can incorporate, e.g. solvent–solute interactions resulting possibly in phase decomposition, concentration–dependent dispersion forces (wettability), entropic terms accounting for mixing in the case of polymers and solutions, etc.

In Chapter 3 we have considered an isothermal variant of the general thin film equation and we have applied it to slowly evaporating small sessile droplets. We have first studied evaporating droplets with an influx localised in the centre of the drop and serving to establish non–trivial steady states. We have applied an asymptotic analysis at the transition region between the precursor film and the shape of the bulk droplet. Further, we have employed the model to study the time evolution of freely evaporating drops without influx with various initial shapes. We have shown that a freely evaporating shrinking drop is always characterised by a smaller apparent contact angle (measured as the slope at the inflection point of the height profile) as compared to the steadily fed drop. In our simulations we have found that a drop spreads [shrinks] from the beginning if its initial contact angle is larger [smaller] than the contact angle of a large evaporating drop with influx of the same volume.

This seems to be a very promising result that should be further scrutinised as it might have interesting consequences: (i) If the apparent contact angle of a steady drop with influx takes the role of an equilibrium contact angle $\theta_e$, relations between the dynamic angles and the contact line velocity known from non-volatile partially wetting liquids [39] could hold. Although, this has recently been shown for the case of evaporating partially wetting liquid [5], it remains an open question for the case of a wetting liquid that we study here. (ii) It might further be possible to predict the maximal drop radius and the contact angle at which the initial spreading ceases, and the 'turn around' to the receding motion occurs. It seems plausible that the profile at turnaround might actually be identical to the steady drop profile with influx at the same volume. Note that the freely evaporating drop spreads *and* evaporates, i.e., the volume at turn-around does not correspond to the initial one.

Note also, that we have studied a particular evaporation model valid for small drops in situations where thermal aspects and the dynamics in the surrounding gas phase can be neglected. However, the non-isothermal models can all be studied with a similar methodology, i.e., the properties of steady drops with local influx can be determined and may be employed to gain a deeper understanding of the coupled transport and phase change processes.

In Chapter 4 we have discussed the behaviour of thin films of non-volatile liquid mixtures, colloidal suspensions and polymer solutions on a solid substrate. We have used a gradient dynamics formulation based on an underlying free energy functional that has allowed us to establish coupled long-wave time evolution equations for the film height and mean solute concentration that reduce for a 'passive' solute to equations, well known in the literature [53, 187]. This form naturally allows us to incorporate additional effects. In particular, we have focused on the inclusion of a concentration-dependent wettability, derived with the help of homogenisation techniques to obtain effective optical characteristics. Combining this with the classical theory of effective molecular interactions between the free surface of the film and the smooth solid substrate, we have arrived at a wetting energy that depends on film height and concentration. Its partial derivative with respect to the film height is a concentration and height dependent Derjaguin (or disjoining) pressure.

We have used the derived dynamical model to study the linear stability of flat homogeneous films. In particular, we have investigated how the stability thresholds are influenced by the incorporation of the additional degree of freedom related to the concentration field. We have also analysed nonlinear thickness and concentration profiles for steady droplets and have related them to the binodal curves obtained for the case of two coupled fields. Finally, we have looked at the time evolution of flat homogeneous films with solute and have further discussed the dynamical effects of the coupled height and composition fluctuations.

The presented case illustrates that the above introduced thermodynamically consistent long-wave model allows one to predict a novel interface instability for thin

films (below about 100 nm) of liquid mixtures and suspensions under the influence of long-range van der Waals forces that are concentration dependent. The resulting coupling of film height and concentration fluctuations always renders such films more unstable than the decoupled subsystems. It is demonstrated that the destabilisation can even occur if all decoupled subsystems are unconditionally stable.

In summary, we have presented a general gradient dynamics model and a particular underlying free energy which is able to describe a wide range of dynamical processes in thin films of liquid mixtures, solutions, and suspensions on solid substrates, including the dynamics of coupled dewetting and decomposition. Moreover, we have discussed the physical meaning of important contributions that are missing in the hydrodynamic literature and have shown that they are needed for a thermodynamically consistent description of, e.g., evolution pathways controlled by concentration-dependent wettability. The presented gradient dynamics form will allow for systematic future developments. Most importantly, the here presented model for a film of a mixture without enrichment or depletion boundary layers at the interfaces may be combined with models for films with an insoluble surfactant [79, 164] to also describe systems where enrichment or depletion layers form at the interfaces, including instabilities and structuring processes, as observed in Ref. [175].

Further, the model provides intriguing opportunities for a theoretical description of effects specific to polymer systems. In particular, it can almost effortlessly accommodate effects like Flory–Huggins free energy, accounting for coupling of decomposition and dewetting for the case of polymer mixtures/solutions, as well as attractive terms between the solute particles to study gelation.

In Chapter 5 we have introduced a parameter–passing scheme between coarse-grained particle-based Molecular Dynamics simulations and the continuum lubrication model for the case of small droplets of polymeric liquids on solid substrates. The liquid-vapor interfacial tension, and the interface potential as a function of the film height have been determined by the particle-based simulations in the

canonical ensemble. A method, based on the anisotropy of the pressure inside the film, developed in [179], has allowed us to compute the interface potential for laterally corrugated substrates. The so-derrived interface potential has been passed towards the continuum description provided by the thin film theory in a region where both descriptions are feasible.

Further, drop profiles of various size obtained by both descriptions have been compared and analysed. We have found quantitative agreement if (i) the full curvature is used in the continuum model for large contact angles and (ii) the size of the drop is larger than the lateral correlation length of the interface fluctuations. Moreover, we have found that the long-wave approximation describes the droplet shapes even quantitatively quite well for contact angles up to about 30 degree. This is an excellent starting point for comparing the dynamics of droplets driven by external forces, which we will possibly pursue in the future.

FIGURE 6.1: Inspiration could be so easy to find - accidental dewetting experiments in my bathroom.

# Bibliography


[1] Hoomd-blue. http://codeblue.umich.edu/hoomd-blue.

[2] Refractive index database. http://refractiveindex.info.

[3] Abraham, D., Latremoliere, F., and Upton, P. Divergence of the point tension at wetting. Phys. Rev. Lett. 71, 3 (1993), 404–407.

[4] Ajaev, V. S. Spreading of thin volatile liquid droplets on uniformly heated surfaces. J. Fluid Mech. 528 (2005), 279–296.

[5] Ajaev, V. S., Gambaryan-Roisman, T., and Stephan, P. Static and dynamic contact angles of evaporating liquids on heated surfaces. J. Colloid Interface Sci. 342 (2010), 550–558.

[6] Allen, M., and Tildesley, D. Computer simulation of liquids. Oxford science publications. Clarendon Press, 1989.

[7] Anderson, D. M., and Davis, S. H. The spreading of volatile liquid droplets on heated surfaces. Phys. Fluids 7 (1995), 248–265.

[8] Anderson, D. M., McFadden, G. B., and Wheeler, A. A. Diffuse-interface methods in fluid mechanics. Ann. Rev. Fluid Mech. 30 (1998), 139–165.

[9] Anderson, J. A., Lorenz, C. D., and Travesset, A. General purpose molecular dynamics simulations fully implemented on graphics processing units. J. Comput. Phys. 227, 10 (2008), 5342 – 5359.

[10] Archer, A. J., and Evans, R. Dynamical density functional theory and its application to spinodal decomposition. J. Chem. Phys. 121 (2004), 4246–4254.

[11] Balmforth, N. J., Craster, R. V., and Sassi, R. Dynamics of cooling viscoplastic domes. J. Fluid Mech. 499 (2004), 149–182.

[12] Bankoff, S. G. Significant questions in thin liquid-film heat-transfer. J. Heat Transf.-Trans. ASME 116 (1994), 10–16.

[13] Becker, J., Grün, G., Seemann, R., Mantz, H., Jacobs, K., Mecke, K. R., and Blossey, R. Complex dewetting scenarios captured by thin-film models. Nat. Mater. 2 (2003), 59–63.

[14] Beltrame, P., Knobloch, E., Hänggi, P., and Thiele, U. Rayleigh and depinning instabilities of forced liquid ridges on heterogeneous substrates. Phys. Rev. E 83 (2011), 016305.

[15] Benney, D. J. Long waves on liquid films. J. Math. & Phys. 45 (1966), 150–155.

[16] Berim, G. O., and Ruckenstein, E. Nanodrop on a nanorough solid surface: Density functional theory considerations. J. Chem. Phys. 129, 1 (2008), 014708.

[17] Bestehorn, M., and Neuffer, K. Surface patterns of laterally extended thin liquid films in three dimensions. Phys. Rev. Lett. 87 (2001), 046101.

[18] Bestehorn, M., Pototsky, A., and Thiele, U. 3D large scale Marangoni convection in liquid films. Eur. Phys. J. B 33 (2003), 457–467.

[19] Bhatt, D., Newman, J., and Radke, C. J. Molecular simulation of disjoining-pressure isotherms for free liquid, Lennard-Jones thin films. J. Phys. Chem. B 106 (2002), 6529–6537.

[20] Bird, R. B., Armstrong, R., and Hassager, O. Dynamics of Polymeric Liquids, vol. 1, 2. Wiley, New York, 1977.

[21] Bonn, D., Eggers, J., Indekeu, J., Meunier, J., and Rolley, E. Wetting and spreading. Rev. Mod. Phys. 81 (2009), 739–805.

[22] Boos, W., and Thess, A. Cascade of structures in long-wavelength Marangoni instability. Phys. Fluids 11 (1999), 1484–1494.

[23] Borcia, R., Borcia, I. D., and Bestehorn, M. Nonlinear dynamics of thin liquid films consisting of two miscible components. Phys. Rev. E 86 (Nov 2012), 056319.

[24] Bormashenko, E., Pogreb, R., Stanevsky, O., Bormashenko, Y., Stein, T., and Gengelman, O. Mesoscopic patterning in evaporated polymer solutions: New experimental data and physical mechanisms. Langmuir 21 (2005), 9604–9609.

[25] Brochard-Wyart, F., Di Meglio, J. M., Quere, D., and De Gennes, P. G. Spreading of nonvolatile liquids in a continuum picture. Langmuir 7, 2 (1991), 335–338.

[26] Bruggeman, D. A. G. Calculation of various physical properties of heterogeneous substances. Ann. Phys. 24 (1935), 636–679.

[27] Brusch, L., Kühne, H., Thiele, U., and Bär, M. Dewetting of thin films on heterogeneous substrates: Pinning versus coarsening. Phys. Rev. E 66 (2002), 011602.

[28] Butt, H., and Kappl, M. Surface and interfacial forces. Wiley, 2010.

[29] Cachile, M., Benichou, O., and Cazabat, A. M. Evaporating droplets of completely wetting liquids. Langmuir 18 (2002), 7985–7990.

[30] Cahn, J. W., and Hilliard, J. E. Free energy of a nonuniform system. 1. Interfacual free energy. J. Chem. Phys. 28 (1958), 258–267.

[31] Carey, V. P., and Wemhoff, A. P. Disjoining pressure effects in ultra-thin liquid films in micropassages: Comparison of thermodynamic theory with predictions of molecular dynamics simulations. ASME Conference Proceedings 2005, 42223 (2005), 511–520.

[32] Churaev, N. Derjaguin's disjoining pressure in the colloid science and surface phenomena.

[33] Cieplak, M., Koplik, J., and Banavar, J. R. Boundary conditions at a fluid-solid interface. Phys. Rev. Lett. 86 (2001), 803–806.

[34] Clarke, N. Instabilities in thin-film binary mixtures. Eur. Phys. J. E 14 (2004), 207–210.

[35] Clarke, N. Toward a model for pattern formation in ultrathin-film binary mixtures. Macromolecules 38 (2005), 6775–6778.

[36] Craster, R. V., Matar, O. K., and Sefiane, K. Pinning, retraction, and terracing of evaporating droplets containing nanoparticles. Langmuir (2009). online available.

[37] De Coninck, J., and Blake, T. Wetting and molecular dynamics simulations of simple liquids. Ann. Rev. Mat. Res. 38, 1 (2008), 1–22.

[38] de Gennes, P., Brochard-Wyart, F., and Quéré, D. Capillarity and Wetting Phenomena: Drops, Bubbles, Pearls, Waves. Springer, 2004.

[39] de Gennes, P.-G. Wetting: Statics and dynamics. Rev. Mod. Phys. 57 (1985), 827–863.

[40] Deegan, R. D. Pattern formation in drying drops. Phys. Rev. E 61 (2000), 475–485.

[41] Deegan, R. D., Bakajin, O., Dupont, T. F., Huber, G., Nagel, S. R., and Witten, T. A. Capillary flow as the cause of ring stains from dried liquid drops. Nature 389 (1997), 827–829.

[42] Deegan, R. D., Bakajin, O., Dupont, T. F., Huber, G., Nagel, S. R., and Witten, T. A. Contact line deposits in an evaporating drop. Phys. Rev. E 62 (2000), 756–765.

[43] Dietrich, S. Phase Transitions and Critical Phenomena. Academic Press, New York, 1988.

[44] Dietrich, S., and Napiórkowski, M. Analytic results for wetting transitions in the presence of van der waals tails. Phys. Rev. A 43 (Feb 1991), 1861–1885.

[45] Doedel, E., Keller, H. B., and Kernevez, J. P. Numerical analysis and control of bifurcation problems (I) Bifurcation in finite dimensions. Int. J. Bifurcation Chaos 1 (1991), 493–520.

[46] Doedel, E., Keller, H. B., and Kernevez, J. P. Numerical analysis and control of bifurcation problems (II) Bifurcation in infinite dimensions. Int. J. Bifurcation Chaos 1 (1991), 745–72.

[47] Doedel, E. J., Champneys, A. R., Fairgrieve, T. F., Kuznetsov, Y. A., Sandstede, B., and Wang, X. J. AUTO97: Continuation and bifurcation software for ordinary differential equations. Concordia University, Montreal, 2000.

[48] Dunn, G. J., Wilson, S. K., Duffy, B. R., David, S., and Sefiane, K. A mathematical model for the evaporation of a thin sessile liquid droplet: Comparison between experiment and theory. Colloid Surf. A-Physicochem. Eng. Asp. 323 (2008), 50–55.

[49] Dunn, G. J., Wilson, S. K., Duffy, B. R., David, S., and Sefiane, K. The strong influence of substrate conductivity on droplet evaporation. J. Fluid Mech. 623 (2009), 329–351.

[50] Dupuis, A., and Yeomans, J. M. Modeling droplets on superhydrophobic surfaces: equilibrium states and transitions. Langmuir 21, 6 (2005), 2624–2629. PMID: 15752062.

[51] Elder, K. R., Katakowski, M., Haataja, M., and Grant, M. Modeling elasticity in crystal growth. Phys. Rev. Lett. 88 (2002), 245701.

[52] Español, P., and Warren, P. Statistical mechanics of dissipative particle dynamics. Europhys. Lett. 30, 4 (1995), 191.

[53] Frastia, L., Archer, A. J., and Thiele, U. Dynamical model for the formation of patterned deposits at receding contact lines. Phys. Rev. Lett. 106 (2011), 077801.

[54] Frastia, L., Archer, A. J., and Thiele, U. Modelling the formation of structured deposits at receding contact lines of evaporating solutions and suspensions. Soft Matter 8 (2012), 11363–11386.

[55] Geoghegan, M., and Krausch, G. Wetting at polymer surfaces and interfaces. Prog. Polym. Sci. 28 (2003), 261–302.

[56] Getta, T., and Dietrich, S. Line tension between fluid phases and a substrate. Phys. Rev. E 57 (Jan 1998), 655–671.

[57] Gnanappa, A. K., Gogolides, E., Evangelista, F., and Riepen, M. Contact line dynamics of a superhydrophobic surface: application for immersion lithography. Microfluidics and Nanofluidics 10, 6 (2011), 1351–1357.

[58] Greenspan, H. P. On the motion of a small viscous droplet that wets a surface (relevant to cell movement). J. Fluid Mech. 84 (1978), 125–143.

[59] Grest, G. S., and Kremer, K. Molecular dynamics simulation for polymers in the presence of a heat bath. Phys. Rev. A 33 (May 1986), 3628–3631.

[60] Gross, M., Varnik, F., and Raabe, D. Fall and rise of small droplets on rough hydrophobic substrates. Europhys. Lett. 88, 2 (2009), 26002.

[61] Grzelak, E. M., and Errington, J. R. Calculation of interfacial properties via free-energy-based molecular simulation: The influence of system size. J. Chem. Phys. 132, 22 (2010), 224702.

[62] Hadjicostantinou, N. G. Combining atomistic and continuum simulations of contact-line motion. Phys. Rev. E 59 (1999), 2475–2478.

[63] Han, M. Disjoining properties of Ne and Ar on graphite surface. Colloid Surface A 317 (2008), 679–686.

[64] Hariharan, A., and Harris, J. G. Structure and thermodynamics of the liquid–vapor interface of fluorocarbons and semifluorinated alkane diblocks: A molecular dynamics study. J. Chem. Phys. 101, 5 (1994), 4156–4165.

[65] Hayashi, S. Optical study of electromagnetic surface modes in microcrystals. Japanese Journal of Applied Physics 23, Part 1, No. 6 (1984), 665–676.

[66] Heier, J., Groenewold, J., Huber, S., Nuesch, F., and Hany, R. Nanoscale structuring of semiconducting molecular blend films in the presence of mobile counterions. Langmuir 24, 14 (2008), 7316–7322.

[67] Heine, D. R., Grest, G. S., and Webb, E. B. Spreading dynamics of polymer nanodroplets. Phys. Rev. E 68 (Dec 2003), 061603.

[68] Herring, A., and Henderson, J. Simulation study of the disjoining pressure profile through a three-phase contact line. J. Chem. Phys. 132 (2010), 084702.

[69] Hocking, L. M. On contact angles in evaporating liquids. Phys. Fluids 7 (1995), 2950–2954.

[70] Hoogerbrugge, P. J., and Koelman, J. M. V. A. Simulating microscopic hydrodynamic phenomena with dissipative particle dynamics. Europhys. Lett. 19, 3 (1992), 155.

[71] Huang, J., Kim, F., Tao, A. R., Connor, S., and Yang, P. Spontaneous formation of nanoparticle stripe patterns through dewetting. Nat. Mater. 4 (2005), 896–900.

[72] Huppert, H. E. Flow and instability of a viscous current down a slope. Nature 300 (1982), 427–429.

[73] Indekeu, J. Line Tension Near the Wetting Transition - Results from an Interface Displacement Model. Physica A 183, 4 (1992), 439–461.

[74] Israelachvili, J. Intermolecular and Surface Forces (Third Edition). Elsevier, 2011.

[75] John, K., Bär, M., and Thiele, U. Self-propelled running droplets on solid substrates driven by chemical reactions. Eur. Phys. J. E 18 (2005), 183–199.

[76] Kalliadasis, S., and Thiele, U., Eds. Thin Films of Soft Matter. Springer, Wien, 2007.

[77] Kataoka, D. E., and Troian, S. M. A theoretical study of instabilities at the advancing front of thermally driven coating films. J. Colloid Interface Sci. 192 (1997), 350–362.

[78] Konnur, R., Kargupta, K., and Sharma, A. Instability and morphology of thin liquid films on chemically heterogeneous substrates. Phys. Rev. Lett. 84 (2000), 931–934.

[79] Köpf, M. H., Gurevich, S. V., Friedrich, R., and Chi, L. F. Pattern formation in monolayer transfer systems with substrate-mediated condensation. Langmuir 26 (2010), 10444–10447.

[80] Koplik, J., and Banavar, J. R. Continuum deductions from molecular hydrodynamics. Annu. Rev. Fluid Mech. 27 (1995), 257–292.

[81] Koplik, J., and Banavar, J. R. Molecular simulations of dewetting. Phys. Rev. Lett. 84 (2000), 4401–4404.

[82] Koplik, J., Pal, S., and Banavar, J. R. Dynamics of nanoscale droplets. Phys. Rev. E 65 (2002), 021504.

[83] Kremer, K., and Grest, G. S. Dynamics of entangled linear polymer melts: A molecular-dynamics simulation. J. Chem. Phys. 92, 8 (1990), 5057–5086.

[84] Krishnamoorthy, S., Ramaswamy, B., and Joo, S. W. Spontaneous rupture of thin liquid films due to thermocapillarity: A full-scale direct numerical simulation. Phys. Fluids 7 (1995), 2291–2293.

[85] Krogman, K. C., Druffel, T., and Sunkara, M. K. Anti-reflective optical coatings incorporating nanoparticles. Nanotechnology 16, 7 (2005), S338.

[86] Laplace, P. S. Sur l'action capillaire. Suppl. au livre X, Traité de Mécanique Céleste (1806), 349.

[87] Larson, R. The structure and rheology of complex fluids. Oxford University Press, 1998.

[88] Leizerson, I., Lipson, S. G., and Lyushnin, A. V. When larger drops evaporate faster. Nature 422 (2003), 395–396.

[89] Léonforte, F., Servantie, J., Pastorino, C., and Müller, M. Molecular transport and flow past hard and soft surfaces: Computer simulation of model systems. J. Phys.: Condens. Matter 23, 18 (2011), 184105.

[90] Leshev, I., and Peev, G. Film flow on a horizontal rotating disk. Chemical Engineering and Processing: Process Intensification 42, 11 (2003), 925–929.

[91] Lin, Z., Kerle, T., Russell, T. P., Schäffer, E., and Steiner, U. Structure formation at the interface of liquid liquid bilayer in electric field. Macromolecules 35 (2002), 3971–3976.

[92] Lipowsky, R., and Fisher, M. E. Scaling regimes and functional renormalization for wetting transitions. Phys. Rev. B. 36 (1987), 2126–2141.

[93] Lyushnin, A. V., Golovin, A. A., and Pismen, L. M. Fingering instability of thin evaporating liquid films. Phys. Rev. E 65 (2002), 021602.

[94] MacDowell, L. G., and Müller, M. Adsorption of polymers on a brush: Tuning the order of the wetting phase transition. J. Chem. Phys. 124, 8 (2006), 084907.

[95] MacDowell, L. G., Müller, M., and Binder, K. How do droplets on a surface depend on the system size? Colloid Surface A 206, 1-3 (2002), 277 – 291.

[96] Marconi, U. M. B., and Tarazona, P. Dynamic density functional theory of fluids. J. Chem. Phys. 110 (1999), 8032–8044.

[97] Matar, O. K., Craster, R. V., and Sefiane, K. Dynamic spreading of droplets containing nanoparticles. Phys. Rev. E 76 (2007), 056315.

[98] Mellenthin, J., Karma, A., and Plapp, M. Phase-field crystal study of grain-boundary premelting. Phys. Rev. B 78 (2008), 184110.

[99] Milchev, A., and Binder, K. Polymer melt droplets adsorbed on a solid wall: A monte carlo simulation. J. Chem. Phys. 114, 19 (2001), 8610–8618.

[100] Mitlin, V. S. Dewetting of solid surface: Analogy with spinodal decomposition. J. Colloid Interface Sci. 156 (1993), 491–497.

[101] Mognetti, B. M., Kusumaatmaja, H., and Yeomans, J. M. Drop dynamics on hydrophobic and superhydrophobic surfaces. Faraday Discuss. 146 (2010), –.

[102] Moradi, N., Varnik, F., and Steinbach, I. Roughness-gradientinduced spontaneous motion of droplets on hydrophobic surfaces: A lattice boltzmann study. Europhys. Lett. 89, 2 (2010), 26006.

[103] Morariu, M. D., Schäffer, E., and Steiner, U. Molecular forces caused by the confinement of thermal noise. Phys. Rev. Lett. 92 (2004), 156102.

[104] Moriarty, P., Taylor, M. D. R., and Brust, M. Nanostructured cellular networks. Phys. Rev. Lett. 89 (2002), 248303.

[105] Morris, S. J. S. Contact angles for evaporating liquids predicted and compared with existing experiments. J. Fluid Mech. 432 (2001), 1–30.

[106] Morris, S. J. S. The evaporating meniscus in a channel. J. Fluid Mech. 494 (2003), 297–317.

[107] Müller, M., and Binder, K. Interface localization-delocalization transition in a symmetric polymer blend: A finite-size scaling Monte Carlo study. Phys. Rev. E 6302 (FEB 2001).

[108] Müller, M., and MacDowell, L. G. Wetting of polymer liquids: Monte Carlo simulations and self-consistent field calculations. J. Phys.: Condens. Matter 15, 19 (2003), R609.

[109] Müller, M., Pastorino, C., and Servantie, J. Flow, slippage and a hydrodynamic boundary condition of polymers at surfaces. J. Phys.: Condens. Matter 20, 49 (2008), 494225.

[110] Müller-Buschbaum, P., Bauer, E., Pfister, S., Roth, S. V., Burghammer, M., Riekel, C., David, C., and Thiele, U. Creation of multi-scale stripe-like patterns in thin polymer blend films. Europhys. Lett. 73 (2006), 35–41.

[111] Napiórkowski, M., and Dietrich, S. Structure of the effective hamiltonian for liquid-vapor interfaces. Phys. Rev. E 47 (Mar 1993), 1836–1849.

[112] Náraigh, L. Ó., and Thiffeault, J. L. Nonlinear dynamics of phase separation in thin films. Nonlinearity 23 (2010), 1559–1583.

[113] Niklasson, G. A., Granqvist, C. G., and Hunderi, O. Effective medium models for the optical properties of inhomogeneous materials. Appl. Opt. 20, 1 (Jan 1981), 26–30.

[114] Oron, A., Davis, S. H., and Bankoff, S. G. Long-scale evolution of thin liquid films. Rev. Mod. Phys. 69 (1997), 931–980.

[115] Oron, A., and Rosenau, P. Formation of patterns induced by thermocapillarity and gravity. J. Physique II France 2 (1992), 131–146.

[116] Padmakar, A., Kargupta, K., and Sharma, A. Instability and dewetting of evaporating thin water films on partially and completely wettable substrates. J. Chem. Phys. 110 (1999), 1735–1744.

[117] Pastorino, C., Binder, K., Kreer, T., and Müller, M. Static and dynamic properties of the interface between a polymer brush and a melt of identical chains. J. Chem. Phys. 124, 6 (2006), 064902.

[118] Pauliac-Vaujour, E., Stannard, A., Martin, C. P., Blunt, M. O., Notingher, I., Moriarty, P., Vancea, I., and Thiele, U. Fingering instabilities in dewetting nanofluids. Phys. Rev. Lett. 100 (2008), 176102.

[119] Pereira, A., Trevelyan, P. M. J., Thiele, U., and Kalliadasis, S. Dynamics of a horizontal thin liquid film in the presence of reactive surfactants. Phys. Fluids 19 (2007), 112102.

[120] Phillips, C. L., Anderson, J. A., and Glotzer, S. C. Pseudo-random number generation for brownian dynamics and dissipative particle dynamics simulations on gpu devices. J. Comput. Phys. 230, 19 (2011), 7191 – 7201.

[121] Pismen, L. M. Mesoscopic hydrodynamics of contact line motion. Colloid Surf. A-Physicochem. Eng. Asp. 206 (2002), 11–30.

[122] Pismen, L. M. Spinodal dewetting in a volatile liquid film. Phys. Rev. E 70 (2004), 021601.

[123] Pomeau, Y. Recent progress in the moving contact line problem: a review. C. R. Mecanique 330 (2002), 207–222.

[124] Pototsky, A., Bestehorn, M., Merkt, D., and Thiele, U. Morphology changes in the evolution of liquid two-layer films. J. Chem. Phys. 122 (2005), 224711.

[125] Poulard, C., Guena, G., Cazabat, A.-M., Boudaoud, A., and Ben Amar, M. Rescaling the dynamics of evaporating drops. Langmuir 21 (2005), 8226.

[126] Poulard, C., Voue, M., De Coninck, J., and Cazabat, A. M. Spreading of nematic liquid crystals on hydrophobic substrates. Colloid Surf. A-Physicochem. Eng. Asp. 282 (2006), 240–246.

[127] Prieve, D. C., and Russel, W. B. Simplified predictions of hamaker constants from lifshitz theory. Journal of Colloid and Interface Science 125, 1 (1988), 1 – 13.

[128] Priezjev, N. V., Darhuber, A. A., and Troian, S. M. Slip behavior in liquid films on surfaces of patterned wettability: Comparison between continuum and molecular dynamics simulations. Phys. Rev. E 71 (2005), 041608.

[129] Qian, T. Z., Wang, X. P., and Sheng, P. Molecular scale contact line hydrodynamics of immiscible flows. Phys. Rev. E 68 (2003), 016306.

[130] Qian, T. Z., Wang, X. P., and Sheng, P. Power-law slip profile of the moving contact line in two-phase immiscible flows. Phys. Rev. Lett. 93 (2004), 094501.

[131] Quemada, D. Rheology of concentrated disperse systems and minimum energy-dissipation principle I. Viscosity-concentration relationship. Rheol. Acta 16 (1977), 82–94.

[132] Rauscher, M., and Dietrich, S. Wetting phenomena in nanofluidics. Ann. Rev. Mat. Res. 38, 1 (2008), 143–172.

[133] Rednikov, A. Y., and Colinet, P. Vapor-liquid steady meniscus at a superheated wall: Asymptotics in an intermediate zone near the contact line. Microgravity Sci. Technol. 22 (2010), 249–255.

[134] Reiter, G. Dewetting of thin polymer films. Phys. Rev. Lett. 68 (1992), 75–78.

[135] Riolfo, L. A., Nagatsu, Y., Iwata, S., Maes, R., Trevelyan, P. M. J., and De Wit, A. Experimental evidence of reaction-driven miscible viscous fingering. Phys. Rev. E 85 (Jan 2012), 015304.

[136] Ristenpart, W. D., McCalla, P. M., Roy, R. V., and Stone, H. A. Coalescence of spreading droplets on a wettable substrate. Phys. Rev. Lett. 97 (Aug 2006), 064501.

[137] Rivera, J. L., McCabe, C., and Cummings, P. T. Molecular simulations of liquid-liquid interfacial properties: Water–$n$-alkane and water-methanol–$n$-alkane systems. Phys. Rev. E 67 (Jan 2003), 011603.

[138] Ruckenstein, E., and Jain, R. K. Spontaneous rupture of thin liquid films. J. Chem. Soc. Faraday Trans. II 70 (1974), 132–147.

[139] Safran, S. A. Statistical Thermodynamics of Surfaces, Interfaces, and Membranes. Westview Press, 2003.

[140] Salamon, T. R., Armstrong, R. C., and Brown, R. A. Traveling waves on vertical films: Numerical analysis using the finite element method. Phys. Fluids 5 (1994), 2202–2220.

[141] Samid-Merzel, N., Lipson, S. G., and Tannhauser, D. S. Pattern formation in drying water films. Phys. Rev. E 57 (1998), 2906–2913.

[142] Saulnier, F., Raphaël, E., and de Gennes, P.-G. Dewetting of thin-film polymers. Phys. Rev. E 66 (2002), 061607.

[143] Schick, M. Introduction in wetting phenomena. In Les Houches Lectures on "Liquids at Interfaces" (1990), Elsevier Science Publishers BV, Amsterdam, pp. 415–497.

[144] Schimmele, L., Napiórkowski, M., and Dietrich, S. Conceptual aspects of line tensions. J. Chem. Phys. 127, 16 (2007), 164715.

[145] Schwartz, L. W., and Eley, R. R. Simulation of droplet motion on low-energy and heterogeneous surfaces. J. Colloid Interface Sci. 202 (1998), 173–188.

[146] Seemann, R., Herminghaus, S., and Jacobs, K. Dewetting patterns and molecular forces: A reconciliation. Phys. Rev. Lett. 86 (2001), 5534–5537.

[147] Seemann, R., Herminghaus, S., Neto, C., Schlagowski, S., Podzimek, D., Konrad, R., Mantz, H., and Jacobs, K. Dynamics and

structure formation in thin polymer melt films. J. Phys.: Condens. Matter 17 (2005), S267–S290.

[148] Sefiane, K., Wilson, S. K., David, S., Dunn, G. J., and Duffy, B. R. On the effect of the atmosphere on the evaporation of sessile droplets of water. Phys. Fluids 21 (2009), 062101.

[149] Servantie, J., and Müller, M. Statics and dynamics of a cylindrical droplet under an external body force. J. Chem. Phys. 128, 1 (2008), 014709.

[150] Shahidzadeh-Bonn, N., Rafai, S., Azouni, A., and Bonn, D. Evaporating droplets. J. Fluid Mech. 549 (2006), 307–313.

[151] Shanahan, M. E. R., and Carre, A. Viscoelastic dissipation in wetting and adhesion phenomena. Langmuir 11, 4 (1995), 1396–1402.

[152] Sharma, A. Equilibrium contact angles and film thicknesses in the apolar and polar systems: Role of intermolecular interactions in coexistence of drops with thin films. Langmuir 9 (1993), 3580.

[153] Sharma, A. Relationship of thin film stability and morphology to macroscopic parameters of wetting in the apolar and polar systems. Langmuir 9 (1993), 861–869.

[154] Sharma, A., Mittal, J., and Verma, R. Instability and dewetting of thin films induced by density variations. Langmuir 18 (2002), 10213–10220.

[155] Sharma, A., and Ruckenstein, E. Mechanism of tear film rupture and formation of dry spots on cornea. J. Colloid Interface Sci. 106 (1985), 12–27.

[156] Starov, V. M. Equilibrium and hysteresis contact angles. Adv. Colloid Interface Sci. 39 (1992), 147–173.

[157] Starov, V. M., and Velarde, M. G. Surface forces and wetting phenomena. J. Phys.-Condes. Matter 21 (2009), 464121.

[158] Starov, V. M., Velarde, M. G., and Radke, C. J. Wetting and spreading dynamics. Taylor and Francis, Boca Raton, 2007.

[159] Starov, V. M., Zhdanov, S. A., Kosvintsev, S. R., Sobolev, V. D., and Velarde, M. G. Spreading of liquid drops over porous substrates. Adv. Colloid Interface Sci. 104 (2003), 123–158.

[160] Swope, W. C., Andersen, H. C., Berens, P. H., and Wilson, K. R. A computer simulation method for the calculation of equilibrium constants for the formation of physical clusters of molecules: Application to small water clusters. J. Chem. Phys. 76, 1 (1982), 637–649.

[161] Thiele, U. Structure formation in thin liquid films. In Thin Films of Soft Matter (Wien, 2007), S. Kalliadasis and U. Thiele, Eds., Springer, pp. 25–93.

[162] Thiele, U. Thin film evolution equations from (evaporating) dewetting liquid layers to epitaxial growth. J. Phys.-Cond. Mat. 22 (2010), 084019.

[163] Thiele, U. Note on thin film equations for solutions and suspensions. Eur. Phys. J. Special Topics 197 (2011), 213–220.

[164] Thiele, U., Archer, A. J., and Plapp, M. Thermodynamically consistent description of the hydrodynamics of free surfaces covered by insoluble surfactants of high concentration. Phys. Fluids 24 (2012), 102107.

[165] Thiele, U., Brusch, L., Bestehorn, M., and Bär, M. Modelling thin-film dewetting on structured substrates and templates: Bifurcation analysis and numerical simulations. Eur. Phys. J. E 11 (2003), 255–271.

[166] Thiele, U., and John, K. Transport of free surface liquid films and drops by external ratchets and self-ratcheting mechanisms. Chem. Phys. 375 (2010), 578–586.

[167] Thiele, U., and Knobloch, E. Thin liquid films on a slightly inclined heated plate. Physica D 190 (2004), 213–248.

[168] Thiele, U., and Knobloch, E. On the depinning of a driven drop on a heterogeneous substrate. New J. Phys. 8 (2006), 313.

[169] Thiele, U., Mertig, M., and Pompe, W. Dewetting of an evaporating thin liquid film: Heterogeneous nucleation and surface instability. Phys. Rev. Lett. 80 (1998), 2869–2872.

[170] Thiele, U., Neuffer, K., Bestehorn, M., Pomeau, Y., and Velarde, M. G. Sliding drops on an inclined plane. Colloid Surf. A - Physicochem. Eng. Asp. 206 (2002), 87–104.

[171] Thiele, U., Todorova, D. V., and Lopez, H. Gradient dynamics description for films of mixtures and suspensions: Dewetting triggered by coupled film height and concentration fluctuations. Phys. Rev. Lett. 111 (2013), 117801.

[172] Thiele, U., Velarde, M. G., and Neuffer, K. Dewetting: Film rupture by nucleation in the spinodal regime. Phys. Rev. Lett. 87 (2001), 016104.

[173] Thiele, U., Velarde, M. G., Neuffer, K., Bestehorn, M., and Pomeau, Y. Sliding drops in the diffuse interface model coupled to hydrodynamics. Phys. Rev. E 64 (2001), 061601.

[174] Thiele, U., Velarde, M. G., Neuffer, K., and Pomeau, Y. Film rupture in the diffuse interface model coupled to hydrodynamics. Phys. Rev. E 64 (2001), 031602.

[175] Thomas, K. R., Clarke, N., Poetes, R., Morariu, M., and Steiner, U. Wetting induced instabilities in miscible polymer blends. Soft Matter 6 (2010), 3517–3523.

[176] Tinga, W. R., Voss, W. A. G., and Blossey, D. F. Generalized approach to multiphase dielectric mixture theory. J. Appl. Phys 44 (1973), 3897–3902.

[177] Todorova, D., Thiele, U., and Pismen, L. The relation of steady evaporating drops fed by an influx and freely evaporating drops. J. Eng. Math. 73 (2012), 17–30.

[178] Tolman, R. C. Consideration of the Gibbs theory of surface tension. J. Chem. Phys. 16, 8 (1948), 758–774.

[179] Tretyakov, N. Molecular dynamics simulations of polymer liquids on substrates of different topography. Dissertation, Georg-August University,Göttingen, 2012, 2012.

[180] Tretyakov, N., Müller, M., Todorova, D., and Thiele, U. Parameter passing between molecular dynamics and continuum models for droplets on solid substrates: The static case. J. Chem. Phys. 138 (2013), 064905.

[181] van Teeffelen, S., Backofen, R., Voigt, A., and Löwen, H. Derivation of the phase-field-crystal model for colloidal solidification. Phys. Rev. E 79 (2009), 051404.

[182] Varnik, F., Baschnagel, J., and Binder, K. Molecular dynamics results on the pressure tensor of polymer films. J. Chem. Phys. 113, 10 (2000), 4444–4453.

[183] Varnik, F., Truman, P., Wu, B., Uhlmann, P., Raabe, D., and Stamm, M. Wetting gradient induced separation of emulsions: A combined experimental and lattice boltzmann computer simulation study. Physics of Fluids 20, 7 (2008), 072104.

[184] Vrij, A. Possible mechanism for the spontaneous rupture of thin, free liquid films. Discuss. Faraday Soc. 42 (1966), 23–33.

[185] Walton, J., Tildesley, D., Rowlinson, J., and Henderson, J. The pressure tensor at the planar surface of a liquid. Mol. Phys. 48, 6 (1983), 1357–1368.

[186] Wang, H., and Composto, R. J. Wetting and phase separation in polymer blend films: Identification of four thickness regimes with distinct morphological pathways. Interface Sci. 11 (2003), 237–248.

[187] Warner, M. R. E., Craster, R. V., and Matar, O. K. Surface patterning via evaporation of ultrathin films containing nanoparticles. J. Colloid Interface Sci. 267 (2003), 92–110.

[188] Wasan, D. T., and Nikolov, A. D. Spreading of nanofluids on solids. Nature 423 (2003), 156–159.

[189] Wayner, P. C. Spreading of a liquid film with a finite contact angle by the evaporation/condensation process. Langmuir 9 (1993), 294–299.

[190] Wilson, S., Hunt, R., and Duffy, B. The rate of spreading in spin coating. Journal of Fluid Mechanics 413 (2000), 65–88.

[191] Xu, J., Xia, J. F., and Lin, Z. Q. Evaporation-induced self-assembly of nanoparticles from a sphere-on-flat geometry. Angew. Chem.-Int. Edit. 46 (2007), 1860–1863.

[192] Yamamura, M., Nishio, T., Kajiwara, T., and Adachi, K. Evaporation-induced pattern formation in polymer films via secondary phase separation. Chem. Eng. Sci. 57 (2002), 2901–2905.

[193] Young, T. An essay on the cohesion of fluids. Phil. Trans. R. Soc. Lond. 95 (1805), 65–87.